JGR Planets

RESEARCH ARTICLE

10.1029/2024JE008622

Clouds and Ammonia in the Atmospheres of Jupiter and Saturn Determined From a Band-Depth Analysis of VLT/MUSE Observations

Patrick G. J. Irwin[1], Steven M. Hill[2], Leigh N. Fletcher[3], Charlotte Alexander[1], and John H. Rogers[4]

[1]Atmospheric, Oceanic and Planetary Physics, Department of Physics, University of Oxford, Oxford, UK, [2]Independent Researcher, Denver, CO, USA, [3]School of Physics and Astronomy, University of Leicester, Leicester, UK, [4]British Astronomical Association, London, UK

Key Points:

- Band-depth approximation analysis from 600 to 680 nm reliably maps ammonia abundance at 2–3 bars in atmospheres of both Jupiter and Saturn
- Methane band at 619 nm and ammonia band at 647 nm are formed deeper than the expected ammonia condensation level
- Main observable clouds seen in atmospheres of Jupiter and Saturn are at deeper pressures than the ammonia ice condensation level

Supporting Information:

Supporting Information may be found in the online version of this article.

Correspondence to:

P. G. J. Irwin,
patrick.irwin@physics.ox.ac.uk

Citation:

Irwin, P. G. J., Hill, S. M., Fletcher, L. N., Alexander, C., & Rogers, J. H. (2025). Clouds and ammonia in the atmospheres of Jupiter and Saturn determined from a band-depth analysis of VLT/MUSE observations. *Journal of Geophysical Research: Planets*, *130*, e2024JE008622. https://doi.org/10.1029/2024JE008622

Received 12 JUL 2024
Accepted 11 DEC 2024

Abstract The visible spectrum of Jupiter contains absorption bands of methane (619 nm) and ammonia (647 nm) that can be used to probe the cloud-top pressures and ammonia abundance in Jupiter's atmosphere. Recently, it has been shown that filter-averaged observations of Jupiter made with telescopes and filters accessible to backyard astronomers can be reduced to yield ammonia maps that bear a remarkable similarity with distributions derived using more complex radiative transfer methods. Here, we determine the reliability of this method by applying it to observations made with the MUSE instrument at ESO's Very Large Telescope, and find excellent correspondence with the retrieved products from multiple-scattering retrieval model analyses. We find that the main level of reflection in Jupiter's atmosphere is at 2–3 bar, which is far beneath the anticipated ammonia ice condensation level at ∼0.7 bar, and conclude that pure ammonia ice cannot be the main cloud constituent. We show that the spatial variations of ammonia determined at 2–3 bar are strongly correlated with those determined from thermal-infrared observations, and microwave observations by the Very Large Array and the Juno spacecraft. Finally, we show that the same technique can be applied to observations of Saturn, again yielding maps of ammonia abundance at 2–3 bar that are well-correlated with thermal-IR observations made near 5 μm by Cassini/VIMS and JWST/MIRI. Similarly, the main level of reflectivity is found to be lie far beneath the expected condensation level of ammonia in Saturn's atmosphere at ∼1.8 bar.

Plain Language Summary In a recent paper, it has been shown that it is possible for backyard astronomers to make observations of Jupiter with three to four spectral filters that can be processed to map the abundance of ammonia in Jupiter's atmosphere. Here test the reliability of this filter-imaging technique by applying it to VLT/MUSE observations of Jupiter and show that the method yields surprisingly reliable results that agree closely with more sophisticated analyses of these observations, and which are also consistent with observations made at microwave wavelengths by Juno and the Very Large Array. We show that the main level of reflection at red wavelengths is from the 2–3 bar level, which is well beneath the expected ammonia ice cloud condensation level at ∼0.7 bar, and conclude that ammonia ice cannot be the main cloud constituent. We also show that the same technique can be applied to MUSE observations of Saturn and find that ammonia maps extracted agree very well with the ammonia abundance determined by Cassini and the James Webb Space Telescope at pressures greater than 2 bar.

1. Introduction

Hill et al. (2024) have recently shown that visible-wavelength observations of Jupiter made with telescopes and spectral filters available to backyard astronomers can be used to determine maps of ammonia abundance and cloud-top pressure using the band-depth approximation (e.g., Combes & Encrenaz, 1979). In this paper we assess the efficacy and physical meaning of these ammonia and cloud-top pressure determinations by applying the same technique to spectrally resolved VLT/MUSE observations of Jupiter and comparing the derived abundances with those determined from the same spectra using a multiple-scattering radiative transfer retrieval model, NEMESIS (Irwin et al., 2008), and also with other determinations.

The atmosphere of Jupiter, composed predominantly of hydrogen and helium, contains several condensable gases, which at the cold temperatures found in the upper troposphere are expected to condense to form clouds of aqueous-ammonia/water-ice, ammonium hydrosulfide (NH_4SH) and ammonia at pressure levels ∼10, 2, and

0.7 bar, respectively (West et al., 1986; Atreya et al., 1999; Irwin, 2009, assuming heavy elements are enriched by ~5× solar). Similar calculations for Saturn determine condensation levels of ~20, 6, and 1.8 bar (Irwin, 2009), for the same condensates and Saturnian enrichment levels (5× solar for O/H, N/H, 14× solar for S/H, and 11× solar for C/H). Since ammonia is known to be abundant in these atmospheres and is predicted to condense at the lowest pressures, it is widely expected, and commonly thought, that the main observable clouds we see in images of these planets are ammonia ice clouds. Higher in the atmosphere, photolysis becomes important, which breaks down organic molecules such as methane and ammonia to form complex photochemical products such as ethane and acetylene in the stratosphere (which have been detected) and potential products such as hydrazine and diphosphine in the upper troposphere, which may contribute to the color-carrying chemicals, or "chromophores", that color the clouds of these planets.

Jupiter and Saturn were visited by the Pioneer and Voyager spacecraft in fly bys during the 1970s and 1980s, but the NASA Galileo spacecraft became the first craft to enter into orbit about the Jovian system in 1995, followed many years later by the NASA Juno spacecraft, which entered Jupiter's orbit in 2016. The Galileo orbiter included the Near Infrared Mapping Spectrometer (NIMS, R. W. Carlson et al., 1992; R. Carlson et al., 1996), which recorded spectra from 0.7–5.2 μm, covering wavelengths of both reflected sunlight (0.7–3.5 μm) and thermal emission in the "5-μm window" (4.7–5.2 μm), where radiation thermally emitted from the 5–10 bar region, modulated by the absorption of gases and overlying clouds, is detected. The Galileo orbiter also included the Solid State Imaging (SSI) camera that allowed filter-averaged imaging at various wavelengths from 400 to 1,100 nm. However, Galileo observations were severely handicapped by the main communication antenna not deploying fully and thus data could only be transmitted back to Earth with the low gain antenna at greatly reduced data rate (Gershman et al., 1994; Statman & Deutsch, 1997). Hence, very few complete spectra were returned of Jupiter's atmosphere by NIMS, but one set of four complete spectra (known as the "real-time" spectra) were measured close to Jupiter orbit insertion, targeting a low cloud opacity region known as a "5-μm hotspot" (Orton et al., 1996). Irwin et al. (1998) found that these spectra were consistent with vertically thin NH_4SH and NH_3 clouds, and a detached haze layer near ~0.2 bar. However, further analysis of these spectra (Irwin et al., 2001) found that beneath the upper level haze a single extended vertical distribution of haze, with peak opacity (in terms of specific density, i.e., particles/gram) at ~1.4 bar was more consistent with these observations, suggesting that there was generally no need, or evidence, for a distinct ammonia condensation cloud at ~0.7 bar. Irwin et al. (2001) also found that the main source of the near-IR reflectivity variability, which is seen to be anti-correlated with 5-μm brightness, is due to cloud opacity changes of this deeper cloud. Finally, Roos-Serote and Irwin (2006) analyzed pairs of 5-μm NIMS spectral observations of the Equatorial Zone (EZ) and North Equatorial Belt (NEB) to determine limb-darkening curves, from which it was concluded that the vertical location of the 5-μm absorber was strongly constrained to lie at pressures $p < 2$ bar.

In addition to the orbiter, the Galileo mission also comprised an entry probe, which entered and descended through Jupiter's atmosphere on 7 December 1995 at 6.5°N (planetocentric), 4.4°W (System III), sampling the atmosphere for ~58 min from pressure levels of roughly 0.46 to 15 bar. Although intended to fall through a cloudy region of the EZ, the Galileo probe actually entered the atmosphere in a 5-μm hotspot (Orton et al., 1996), where cloud opacity is known to be anomalously low. The probe nephelometer (Ragent et al., 1992, 1998), which observed light reflected from a GaAs laser source (904 ± 5 nm), found evidence for an upper level haze ($p < 0.5$ bar), a main vertically extended cloud, based at ~1.35 bar, a vertically thin layer at ~1.7 bar, and then a very broad region of low reflectivity centered at 3–4 bar. (N.B., the long wavelength of the GaAs laser was chosen to easily distinguish the laser reflection from background reflected sunshine, and also to make the instrument less sensitive to Rayleigh-scattering from the air.) The Galileo probe also included a Net Flux Radiometer (NFR, Sromovsky et al., 1996, 1998), which determined that the net heating peaked at ~1.35 bar, consistent with the vertical location of the main aerosol layer seen by the nephelometer. Sromovsky et al. (1998) suggested that the upper haze layer at 0.4–0.5 bar was an ammonia ice cloud, composed of small particles (r ~0.5 μm), which is consistent with their retrieved ammonia mole fraction profile with a deep mole fraction of ~250 ppm that started to decrease with altitude at 3–4 bar and did not reach the saturated vapor pressure curve until $p < 0.4$ bar. Sromovsky et al. (1998) concluded that the main aerosol layer was likely composed of moderately sized NH_4SH particles (r ~3 μm). Later, Sromovsky and Fry (2002) found that this model was also consistent with HST/WFPC2 observations over dark and bright regions, with most of the variability accounted for by variation of the opacity of the ~1.35-bar cloud. For various technical reasons the Galileo probe mass spectrometer (GPMS, Niemann et al., 1998) was unable to determine a vertical profile of NH_3, but only an upper limit (relative to H_2) of 2,300 ppm, which was

later revised down to 664 ppm by Wong, Mahaffy, et al. (2004) at ~10 bar. However, measurements of the probe radio signal attenuation (Folkner et al., 1998), found the ammonia mole fraction to steadily increase from 0 ppm at ~1.5 bar to a maximum of ~700 ppm at ~8 bar, and then decrease slightly to ~600 ppm at the maximum measured pressure of 15 bar. Similarly, the Galileo mass spectrometer found the abundance of H_2S to increase with depth to a deep abundance (relative to H_2) of 89 ppm (Wong, Mahaffy, et al., 2004). Further evidence for a steady increase of ammonia mole fraction with depth beneath the ammonia condensation level (perhaps caused by NH_4SH condensation or other processes) comes from microwave, and radio-wave observations (e.g., de Pater et al., 2016, 2019; Fletcher et al., 2021; Moeckel et al., 2023; Showman & de Pater, 2005).

Although Irwin et al. (2001) found no evidence for significant opacity at the ammonia condensation level at ~0.7 bar, analysis of Galileo/SSI observations (Banfield et al., 1998) reported the presence of a vertically thin component at the base of the tropospheric haze at ~0.75 bar, presumed to be composed of ammonia ice, whose optical depth variations were deduced to be primarily responsible for the features seen in Jupiter's atmosphere at red and longer wavelengths. The Galileo/ISS filters used by Banfield et al. (1998) were centered at 756, 727, and 889 nm, which cover a wide range of pressure levels, albeit with coarse resolution, but are most sensitive to upper tropospheric hazes, whose properties were found to be consistent with a review of the field made after the Voyager encounters (West et al., 1986). Later analysis of Galileo/NIMS observations (Baines et al., 2002) found evidence for a component in Jupiter's clouds with significant absorption near 2 μm, which was attributed to ammonia ice (or Spectrally Identifiable Ammonia Clouds - SIACs). However, SIACs were seen to be very uncommon (covering less than 1% of the planet) and were restricted to small regions of turbulent convective activity such as to the northwest of Jupiter's Great Red Spot (GRS). Ammonia and spectrally identifiable NH_3 features were also explored in the near-infrared by Sromovsky and Fry (2010a) and Sromovsky and Fry (2010b), extending to New-Horizons/LEISA by Sromovsky and Fry (2018), and similarly found to be sparsely distributed.

In the mid-infrared, Cassini/CIRS observations have also been found to indicate the presence of aerosols. Matcheva et al. (2005) find aerosol absorption is needed to match the CIRS observations near 7.2 μm, with the cloud opacity profile peaking at 1.1 bar in regions of thin cloud, reducing to 0.9 bar in regions of thick cloud. Meanwhile, Wong, Bjoraker et al. (2004) find that spectral variations seen at longer wavelengths (9.5–10 μm) can be matched with the presence of opacity at the ammonia condensation level, and that spectrally identifiable ammonia ice absorption features are seen near the equator and also at 23°N (planetographic). Finally, Fletcher et al. (2009) also find that aerosol opacity of clouds at pressures less than 1 bar are necessary to match CIRS observations over the 7.2–11.5 μm range.

Whatever the clouds are made of, and whatever their vertical location and distribution, we know that they are generally not pure ice, since we would then expect brilliant white clouds, not the blue-absorbing clouds that are actually seen. It is clear that photochemistry plays a vital role in the formation and scattering properties of the Gas Giant aerosols and there have been many hypotheses put forward for what the chromophores are composed of, including photochemical products of ammonia or methane, or even allotropes of sulfur or phosphorus (Noy et al., 1981). From laboratory experiments R. W. Carlson et al. (2016) found that when irradiated with UV light (λ = 214 nm) mixtures of ammonia and acetylene (C_2H_2) reacted to form a blue-absorbing material, whose properties are consistent with those of Jupiter's chromophores. It was proposed that this material caused the reddening of the GRS, with ammonia upwelling from below meeting photochemically produced acetylene downwelling from above, and photolyzing to form the chromophore, giving rise to the so-called "Créme Brulée" model (Baines et al., 2019). Sromovsky et al. (2017) extended this analysis to other locations on Jupiter by modeling Cassini/VIMS spectra and found that inclusion of different abundances of the "Carlson" chromophore at the top of the clouds was consistent with the measured spectra of many other locations on the planet, suggesting this might be a "universal chromophore."

To probe more deeply in the atmosphere, the NASA Juno mission includes a Microwave Radiometer (MWR, Janssen et al., 2017), which can probe from 0.6–120 bar (e.g., Fletcher et al., 2021). It had been expected that the deep ammonia abundance would be high in the visibly bright "zones", where the air is thought to be upwelling and low in the dark "belts", where the air is thought to be downwelling. However, by inverting these MWR data, Li et al. (2017) found that while there were some belt-zone variations, the distribution was dominated by a very strong maximum at ~5°N and strong depletion at 6–20°N. Although the strong peak at ~5°N had previously been noted in the upper troposphere (Achterberg et al., 2006; Fletcher et al., 2016; Gierasch et al., 1986), MWR found

that these distributions extended very deep into Jupiter's atmosphere, with the latitudinal variation of ammonia abundance inverting at pressures exceeding ~20 bar. These data were reanalyzed by Guillot, Li, et al. (2020), who found similar results, while Moeckel et al. (2023) combined the MWR data with radio-wave observations made with the Very Large Array (VLA), to constrain the deep abundance of ammonia at pressures greater than ~20 bar to be $340.5^{+34.8}_{-21.2}$ ppm. Moeckel et al. (2023) also found that away from 5°N ammonia was depleted everywhere at pressures less than ~20 bar, which is consistent with the previous determinations, and also with a suggested depletion processes, such as "mushballs" (Guillot, Stevenson, et al., 2020), where ammonia is trapped in an exotic phase with water ice and "rains" out to deeper levels, or with powerful downdrafts. In the enhanced ammonia region at ~5°N, Moeckel et al. (2023) curiously found the abundance of ammonia to increase with height (also seen in the analyses of Li et al. (2017) and Guillot, Stevenson, et al. (2020)), rising to values of ~470 ppm near 1 bar.

Higher in the atmosphere, the clouds are mapped regularly by Juno using JunoCam, a public outreach camera that observes in four filters: red, green, blue, and a narrowband methane filter centered at 890 nm. These observations have been processed by the public community to produce ground-breaking new images of Jupiter's clouds from close distances. Juno's orbit is highly elliptical in order to achieve close passes needed for gravitational mapping, with long periods far away from the planet to keep the spacecraft clear of Jupiter's very strong radiation belts. Hence, imaging observations from JunoCam, and also the infrared spectral mapper JIRAM (e.g., Grassi et al., 2020, 2021) are limited in spatial coverage due to the constraints of the orbit, with wider coverage of the polar regions, providing a unique new perspective on Jupiter's poles that are very difficult to observe from the Earth due to Jupiter's small obliquity of only 3°. However, in many sequences taken close to perijove, small white clouds—almost certainly SAICs—can be seen "poking up" above the main cloud deck in JunoCam images (e.g., Guillot et al., 2023). More generally, because Juno's observations of equatorial latitudes are limited to narrow swaths, the mission has been supported by ground-based observations of the wider planet close to the perijoves. One such set of supporting observations are those that have been made using the Multi Unit Spectroscopic Explorer (MUSE) instrument at the Very Large Telescope (VLT) (Alexander, 2024; Braude et al., 2020; Irwin et al., 2019), and also with the New Mexico State University Acousto-optic Imaging Camera at the Apache Point Observatory (Dahl et al., 2021). By inverting these visible/near-IR spectra, both Braude et al. (2020) and Dahl et al. (2021) find that the main cloud deck on Jupiter is, once again, based near the 1.5-bar level, and find that the Créme Brulée model is consistent with this observations, if appropriate modifications are made to the imaginary index of refraction spectrum of the "Carlson" chromophore. Braude et al. (2020) also presents retrievals of the abundance of ammonia at a quoted pressure of ~1 bar along the central meridian, finding enhanced values at the northern edge of the EZ and greatly depleted values in the NEB, with moderately constant values at other latitudes of ~60 ppm. This latitudinal variation is consistent with the Juno/MWR and VLA determinations, but the absolute abundances are significantly smaller than previous estimates.

1.1. Structure of Paper

The latitudinal variation of ammonia determined from amateur observations by Hill et al. (2024) bear a remarkable similarity with the ammonia distributions derived from VLT/MUSE, Juno/MWR and VLA and in this paper we test the reliability of this filter-imaging technique by applying it to MUSE observations of Jupiter (Section 2) and compare the derived results with formal retrievals using the multiple-scattering radiative transfer and retrieval model NEMESIS (Irwin et al., 2008) (Section 3), interpreting our findings in Section 4. In addition, we also assess how applicable and reliable this method is to studying the distribution of ammonia in Saturn's atmosphere (Section 5) and interpret our findings in Section 6. We discuss general implications in Section 7, before summarizing our conclusions in Section 8.

2. VLT/MUSE Observations and Application of Band-Depth Approximation

The Multi Unit Spectroscopic Explorer (MUSE) instrument, at ESO's Very Large Telescope in Chile, is an Integral-Field Unit (IFU) Spectrograph, which records 300 × 300 pixel images from a field of view of 60″ × 60″ in Wide Field Mode, where each 0.2″ × 0.2″ pixel contains a complete visible/near-infrared spectrum (475–933 nm) with a spectral resolving power of 2000–4000 (i.e., a spectral resolution of ~0.2 nm). Since the MUSE data have three dimensions they are often referred to as "cubes." MUSE observations of Jupiter and Saturn have good spatial resolution due to the generally excellent "seeing" at the location of VLT, of typically <0.8″, but

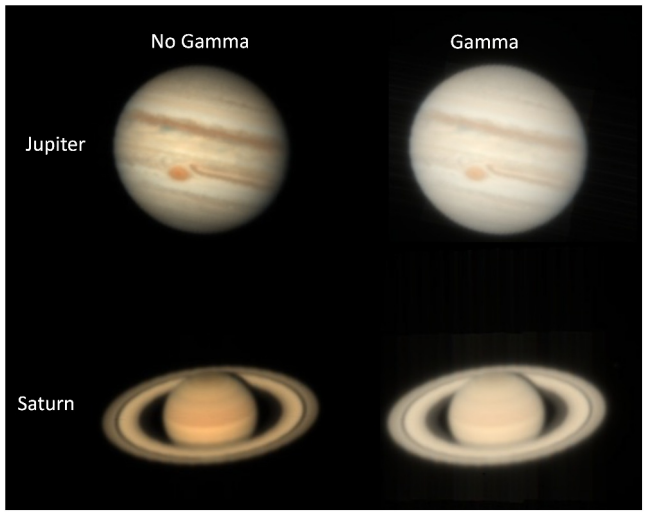

Figure 1. Visible appearance of Jupiter and Saturn reconstructed from VLT/MUSE observations on 23 March 2020 and 6 April 2017, respectively. The left-hand column shows the reconstructed colors when no gamma-correction has been applied, while the right-hand column shows the gamma-corrected appearances, which are closer to what the average human observes with their naked eye through a telescope, but have reduced contrast and are less color enhanced.

observations can also be made with adaptive optics (AO), which improves the spatial resolution still further. The high quality of MUSE observations can be seen in Figure 1, which shows an AO observation of Jupiter, made on 23 March 2020 and a non-AO observation of Saturn, made on 6 April 2017. Both planets are displayed as "true-color" images, showing the banded structure of both planets and including Jupiter's Great Red Spot (GRS) at lower left of the Jupiter image. These "true color" images have been generated as described by Irwin et al. (2024), using standard XYZ color-matching functions, conversion to the sRGB color space and including, or not, the gamma correction of intensities. The images omitting the gamma correction are more contrast-enhanced and better highlight variations across the disc, while the gamma-corrected images are closer to what the average observer would see at the eyepiece of a telescope. Note that to generate these images, the spectrum in each pixel at wavelengths less than the MUSE minimum wavelength of 475 nm has been set to the disc-averaged Jupiter or Saturn spectra of Karkoschka (1994), scaled to match the MUSE spectra at overlapping wavelengths, before the resulting spectra are converted to true color. The color of both Jupiter and Saturn can be seen to have generally an "ochre" color, with slight variation for Saturn, but stronger color variations seen in Jupiter's atmosphere. Pure condensates, such as ammonia and water ice will appear white and hence the colors seen are indicators of photochemistry. Were the atmospheres of Jupiter and Saturn entirely devoid of aerosols then light would penetrate to great depths before being Rayleigh-scattered back. Under these conditions the red-absorbing spectrum of methane becomes significant and so the overall color of both planets would be light blue, as is shown in Figure S1 in Supporting Information S1. VLT/MUSE observations of Jupiter have been made in support of the NASA/Juno mission and cover many Juno perijoves between 2016 and 2023. In addition, there are commissioning observations from 2014. Previous MUSE Jupiter observations have been analyzed by Irwin et al. (2018, 2019) and Braude et al. (2020), who determined latitudinal variations in cloud/haze cover and ammonia abundance. Recent observations are being analyzed by Alexander (2024).

Figure 2 compares the disc-averaged radiance spectra of these planets (reconstructed from the reflectivity spectra of Karkoschka, 1994) with a standard solar spectrum (Chance & Kurucz, 2010) and shows their reflectivity decreasing at shorter, bluer wavelengths, due to the presence of a blue-absorbing "chromophore" in these atmospheres (e.g., R. W. Carlson et al., 2016). At longer wavelengths, absorption bands of methane and ammonia become increasingly strong and are detectable in visible reflectance spectra at 619 and 647 nm, respectively. These bands are more clearly seen in Figure 3, which compares the disc-averaged Jovian spectrum of Karkoschka (1994) from 600–680 nm with the disc-averaged and center-of-disc spectra of Jupiter observed by MUSE on 23 March 2020. The strength of these absorption features are often measured in terms of their "Equivalent Width", where the measured reflectivity spectrum is divided by a "continuum" spectrum to yield the two-way transmission spectrum, $T(\lambda)$, that can be integrated to:

$$W = \int (1 - T(\lambda)) d\lambda. \quad (1)$$

The equivalent width, W, is thus equal to the effective area of the absorption bands, which are shown as the pink and blue areas in Figure 3, and here have values of 2.248 and 0.838 nm, respectively, for the methane and ammonia bands at disc center.

Hill et al. (2024) have shown that filter-averaged imaging observations of Jupiter at visible wavelengths, made with telescopes and equipment within the reach of committed "backyard astronomers", can be reduced to determine estimates of the distribution of ammonia in Jupiter's atmosphere. Observations by Hill et al. (2024) were made with a 28-cm Schmidt-Cassegrain Telescope (SCT) with commercially obtained filters, one centered in the methane band at 619 nm, a second centered on the nearby ammonia band at 647 nm, and two further filters centered on continuum wavelengths at 632 and 656 nm, respectively. The position of these filters relative to our

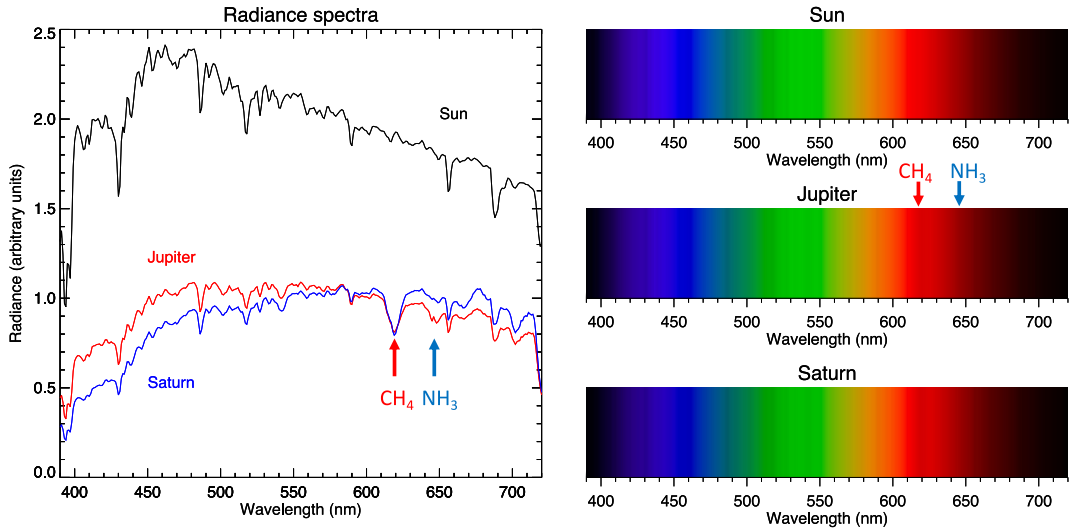

Figure 2. Left panel: Disc-averaged radiance spectra of Jupiter and Saturn, compared to the spectrum of a perfectly reflecting Lambertian surface at the same solar distance (i.e., "Sun"). Right panels compare the same three spectra (normalized) as viewed through a long-slit spectrometer. The solar spectrum is that of Chance and Kurucz (2010) and the calculations also include the transmission spectrum of a standard Earth atmosphere to simulate ground-based observations. The Jupiter and Saturn spectra are constructed from the disc-average reflectivity spectra of Karkoschka (1998), multiplied by the solar and terrestrial atmosphere spectra. Fraunhofer absorption lines from the solar atmosphere are faintly seen in all three spectra, and a faint absorption band is also visible near 619 nm, which is caused by methane absorption in the atmospheres of Jupiter and Saturn, together with a fainter absorption band of ammonia near 647 nm.

reference Jupiter spectra are shown in Figure 3, and are also compared with the measured/estimated absorption spectra of methane (Karkoschka, 1994; Karkoschka & Tomasko, 2010) and ammonia (Coles et al., 2019). The absorption coefficient spectra shown here are calculated at a temperature of 165 K and pressure 1 atm, which is typical of "cloud-top" conditions in Jupiter's atmosphere. Although these coefficient spectra change over the pressures (1–0.1 bar) and temperatures seen in the upper tropospheres of Jupiter and Saturn (by ~5% of peak absorption for methane and ~10% for ammonia) they have to held constant in the band-depth approximation method. The average absorption coefficients of these spectra integrated over the four SCT filters are listed in Table 1.

If we measure the filter-averaged reflectances in these four channels, then Hill et al. (2024) approximates the effective two-way transmission of Jupiter's atmosphere in the methane and ammonia bands as:

$$T_{\mathrm{CH4}} = \frac{R_{619}}{R_{632}} \tag{2}$$

and

$$T_{\mathrm{NH3}} = \frac{R_{647}}{(1-x)R_{632} + xR_{656}} \tag{3}$$

where R_y is the measured reflectivity in the filter centered at y nm, and x is a weighting factor to combine the R_{632} and R_{656} continuum filters equal to $x = (647.0 - 632.0)/(656.0 - 632.0) = 0.625$. The filter-averaged opacities can then be calculated from these transmissions as $\tau_{\mathrm{CH4}} = -\ln(T_{\mathrm{CH4}})$ and $\tau_{\mathrm{NH3}} = -\ln(T_{\mathrm{NH3}})$.

If we assume that the vertical profiles of methane and ammonia differ only by a constant factor at all altitudes (which we will shortly see is not a good assumption), then the abundance of ammonia can be estimated from these observations (see Appendix A) to be:

$$f_{\mathrm{NH3}} = f_{\mathrm{CH4}} \frac{\tau_{\mathrm{NH3}}}{\tau_{\mathrm{CH4}}} \frac{k_{\mathrm{CH4}}}{k_{\mathrm{NH3}}} \tag{4}$$

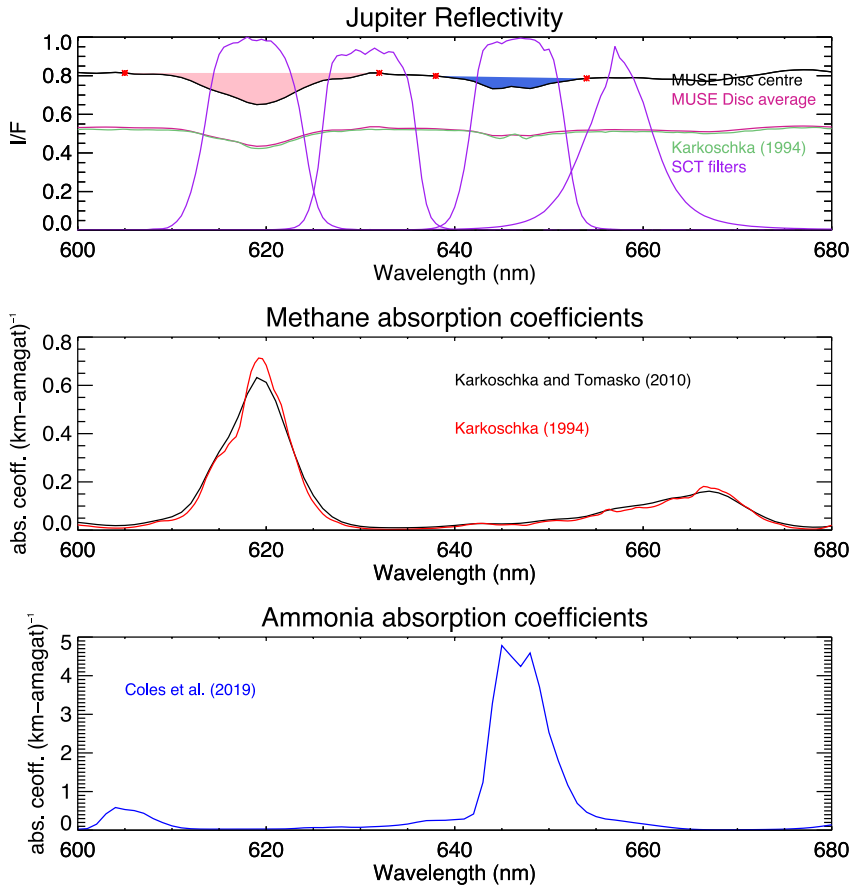

Figure 3. Top panel: Center-of-disc and disc-average 23 March 2020 VLT/MUSE reflectivity spectra compared with disc-averaged reflectivity spectrum of Karkoschka (1994) and filters used in the SCT observations and the HILL method (Hill et al., 2024). The methane and ammonia absorption bands are shaded in pink and blue, and have equivalent widths of 2.248 and 0.838 nm, respectively, where the red asterisks mark the wavelength boundaries of the respective straight line "continuum" spectra. Middle panel: Absorption coefficient spectra of methane (Karkoschka, 1994; Karkoschka & Tomasko, 2010) at 165 K and 1 atm. Bottom panel: Absorption coefficient spectra of ammonia (Coles et al., 2019) for the same path conditions.

where k_{CH4} and k_{NH3} are the filter-averaged absorption coefficients of methane and ammonia in the 619-nm and 647-nm bands, respectively, listed in Table 1, and f_{CH4} is the mole fraction of methane, which was determined from the NASA Galileo entry probe in 1995 to be well mixed (i.e., constant with height) and to have a value of $f_{CH4} = 1.81 \times 10^{-3}$ (Niemann et al., 1998). Note that Equation 4 assumes that the contribution of methane and ammonia absorption bands outside of the 619-nm and 647-nm channels, respectively, can be considered to be negligible. Using this method, which we shall hereon refer to as the HILL method, imaging observations in these channels can be reduced to maps of ammonia abundance. In addition, if we assume that Jupiter's clouds have a

Table 1
Methane and Ammonia Absorption Coefficients (km-amagat)$^{-1}$, Calculated for Path Conditions of 1 atm and 165K, Averaged Over the Four SCT Filters of Hill et al. (2024)

Data source	619 nm	632 nm	647 nm	656 nm
CH_4 (Karkoschka & Tomasko, 2010)	0.42684	0.01931	0.02795	0.08094
CH_4 (Karkoschka, 1994)	0.41919	0.02808	0.03276	0.08891
NH_3 (Coles et al., 2019)	0.03248	0.10571	2.96297	0.45466

Note. An amagat is defined as the number density of an ideal gas at a pressure of 1 atm (1.01325×10^5 Pa) and temperature of 273.15 K, and is equal to: 2.6867811×10^{25} m^{-3}.

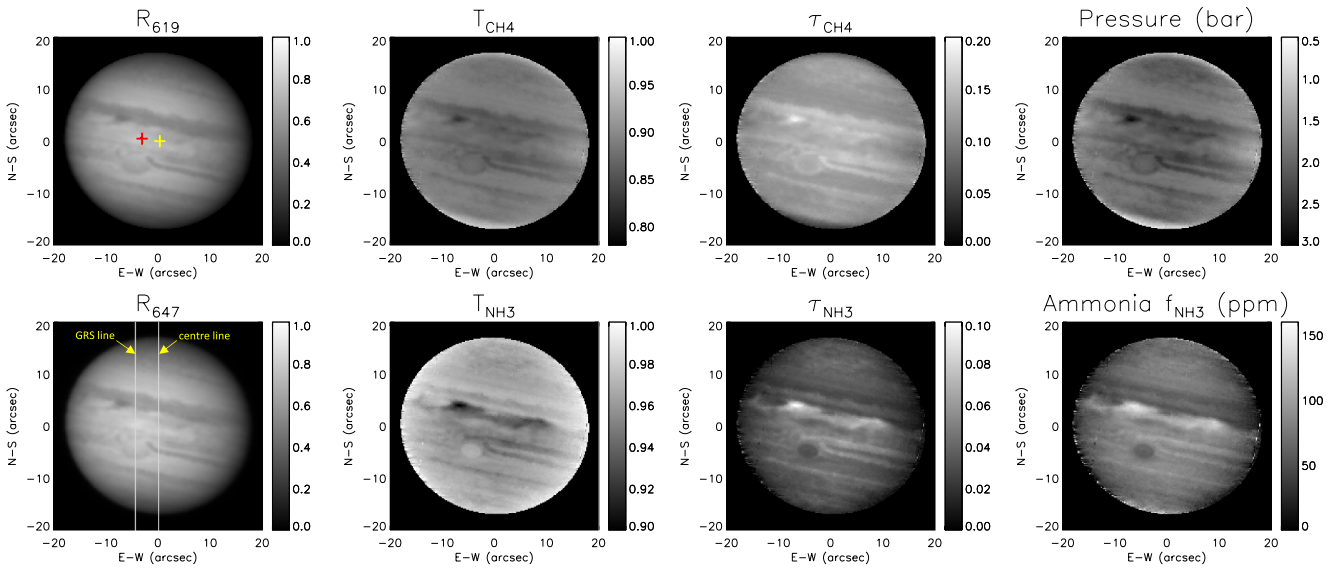

Figure 4. Example of band-depth approximation calculations (HILL method) applied to VLT/MUSE observations of Jupiter made on 23 March 2020. The left hand column shows the observed reflectivity averaged over the 619- and 647-nm SCT filters. The second column shows the transmission of methane and ammonia calculated from the filter-averaged reflectivities. The third column shows the calculated filter-averaged opacities, while the right-hand column shows the calculated maps of cloud top pressure (p_{cloud}) and ammonia abundance (f_{NH3}). The image at 619 nm (top left) also shows the sub-observer point (yellow cross) and the subsolar point (red cross), indicating this is a low phase angle observation. The image at 647 nm (bottom left) includes lines passing through the center-of-disc and GRS, and cross sections in these lines are shown later in Figures 6 and 18.

well-defined upper boundary, known as the Reflecting Layer Model (RLM), then, by rearranging Equation A5 in Appendix A, the τ_{CH4} map can be used to calculate the effective cloud-top pressure:

$$p_{\mathrm{cloud}} = \frac{\tau_{\mathrm{CH4}}\overline{m}g}{\eta f_{\mathrm{CH4}} N_A k_{\mathrm{CH4}}}. \tag{5}$$

Here, $\eta = 1/\mu_0 + 1/\mu$ is the geometric airmass factor (Equation A4), where μ and μ_0 are the cosines of the viewing and solar zenith angles, respectively, and is equal to 2.0 for nadir-viewing. In addition, $\overline{m}$ is the mean molecular weight of the atmosphere (kg/mol), g is the gravitational acceleration (m s^{-2}), and N_A is Avogadro's number. If the absorption coefficient k_{CH4} is expressed in units of (km-amagat)$^{-1}$ then Equation 5 reduces to:

$$p_{\mathrm{cloud}} = \frac{44.615 \times 10^3 \tau_{\mathrm{CH4}}\overline{m}g}{\eta f_{\mathrm{CH4}} k_{\mathrm{CH4}}}. \tag{6}$$

2.1. Application of Filter-Averaged HILL Band Approximation Method to MUSE Observations

In Figure 4, we have applied the HILL method to the MUSE data set measured on 23 March 2020, previously shown in Figure 1. The measured MUSE radiance spectra in each pixel were first converted to reflectivity using the solar spectrum of Meftah et al. (2023) (smoothed to MUSE resolution), setting Jupiter's distance from the Sun at the time to be 5.1975 AU. They were then averaged with a triangular instrument function with FWHM (Full Width Half Maximum) = 2 nm, sampled every 1 nm, to improve the SNR and also because our main source of methane gas absorption spectra (Karkoschka & Tomasko, 2010) has limited spectral resolution. At each location on the disc, we averaged the recorded reflectivity spectra over the four filter profiles shown in Figure 3 to compute the four filter-averaged images, two of which are shown in Figure 4 for reference. The images were then processed to determine the mean atmospheric transmissions in the methane and ammonia filters (Equations 2 and 3), converted to opacity, and then used to determine the cloud-top ammonia abundance (Equation 4) and cloud-top pressure (Equation 5).

It can be seen in Figure 4 that although the maps of τ_{CH4} and τ_{NH3} are similar, they show significant differences. We expect some degree of similarity since variations in cloud vertical structure will affect the column abundances

of both gases, but dividing τ_{NH3} by τ_{CH4} to determine the ammonia mole fraction (Equation 4) should correct for this correlation if the vertical profiles of these gases are assumed to be the same (we shall return to this assumption later). We can see that the ammonia distribution across the planet shows significant enhancement at the northern edge of the EZ at 5°N and then considerable depletion in the North Equatorial Belt (NEB) at 10–20°N. Elsewhere, the ammonia abundance is found to be moderately uniform, except in the Great Red Spot (GRS), where it appears to be significantly depleted. The apparent enhancement toward the north and south poles is difficult to judge reliably as we are here observing at a high zenith angle, where this model may not be so reliable.

2.2. Development and Application of Spectrally Resolved FIT Band Method to MUSE Observations

Since with our MUSE observations we have the complete spectrum at each location, we can extract band-depths not just with the fixed filter profiles of the HILL method, but also with other methods. The HILL method neglects the fact that the ammonia and methane absorption spectra overlap in the 600–680-nm spectral region. Hence, we implemented a more general band-depth approximation method, which we will call the FIT method, to properly account for this. In the FIT method we simulate the measured reflectivity spectrum $R(\lambda)$ at each location with a simple reflection model:

$$R(\lambda) = \left(R_0 + R_1(\lambda - \lambda_0) + R_2(\lambda - \lambda_0)^2\right) \exp(-X_{CH4}k_{CH4}(\lambda) - X_{NH3}k_{NH3}(\lambda)) \quad (7)$$

where R_0, R_1 and R_2 are quadratic polynomial coefficients to fit the continuum, $k_{CH4}(\lambda)$ and $k_{NH3}(\lambda)$ are the assumed methane and ammonia absorption coefficient spectra (shown in Figure 3), and X_{CH4} and X_{NH3} are the fitted two-way column abundances of methane and ammonia, respectively. The parameter λ_0 is a reference wavelength, which was arbitrarily set here to 600 nm. The five free parameters: R_0, R_1, R_2, X_{CH4}, and X_{NH3} were fitted to the observed reflectivity spectra using a least squares algorithm based on that used in NEMESIS (Irwin et al., 2008).

Figure 5 shows the results of applying the FIT method to the MUSE observations, where it can be seen that very similar variations are derived as those determined from the simpler HILL model (Figure 4). This shows that the non-overlapping gas absorption assumption of the HILL method is reasonable, but there are small differences, including the fact that the FIT method finds ammonia to be less depleted in the GRS. The quantitative latitudinal variation of ammonia along Jupiter's the center of Jupiter's disc (indicated in Figure 4) from the FIT model is shown in Figure 6. This distribution bears a remarkable similarity with the abundance of ammonia determined near the 1-bar level from Juno/MWR and VLA (Guillot, Li, et al., 2020; Moeckel et al., 2023), which we show later in Figure 13, and a previous MUSE analysis (Braude et al., 2020), with a peak just north of the EZ at 5°N and a minimum in the North Equatorial Belt (NEB) at 10–20°N.

Turning to cloud-top pressure, we find that for both the HILL and FIT methods values of $p_{cloud} = 2$–3 are determined at equatorial and mid latitudes, reducing to ~1 bar at the poles. A nadir-viewing airmass factor of $\eta = 2$ was used at all latitudes in Equation 5 so we might be concerned that the derived decrease toward the poles could be just a geometric effect of ignoring the variation of η across the disc. However, looking at the map of methane two-way column abundance (X_{CH4}) in Figure 5 it can be seen that although X_{CH4} increases markedly toward the poles, there is a slight decrease toward the limb at all other latitudes. Hence, the reduction of X_{CH4} (and thus p_{cloud}) toward the poles looks real and suggests the clouds are significantly higher in altitude in Jupiter's polar regions, or that there is a thicker layer of overlying aerosols at lower pressures.

The derived p_{cloud} values away from the poles are considerably higher than we might expect if the clouds were dominated by ammonia ice, since ammonia will condense at p ~0.7 bar. In addition to assuming $\eta = 2$ and $f_{CH4} = 1.81 \times 10^{-3}$, p_{cloud} was determined assuming the mean molecular weight to be $\overline{m} = 2.2$ g/mol, while the gravitational acceleration, g, was determined from the gravitational J-coefficients as a function of latitude (e.g., Irwin, 2009) varying from 23.1 ms^{-2} at the equator to 26.9 ms^{-2} at the poles. Since we have good evidence from the Galileo entry probe that methane is well mixed, and have good estimates for its abundance (Niemann et al., 1998) and the values of all other quantities in Equation 5, including the methane absorption coefficient, the calculation of p_{cloud} should be accurate under the assumption that Jupiter contains a single cloud with a well-defined sharp top. To explore this further, Figure 7 shows the calculated two-way nadir transmission spectra from space to different levels in a typical Jovian atmosphere, for aerosol-free conditions, including Rayleigh-scattering opacity and the gaseous absorption of methane and ammonia. Our reference atmospheric profile is

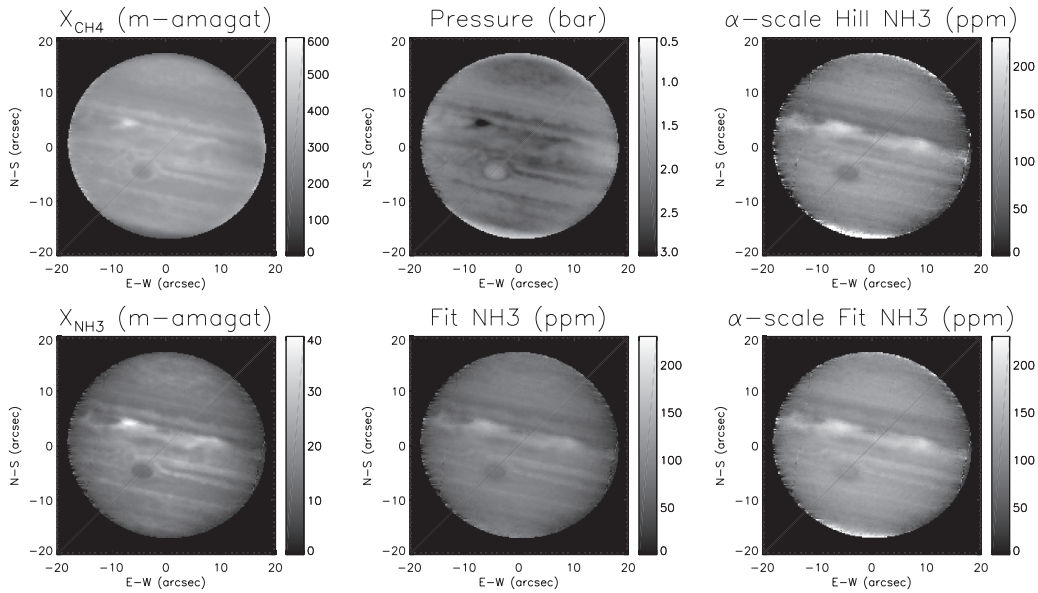

Figure 5. Similar to Figure 4, but showing the results of the analysis of the VLT/MUSE Jupiter observations with the FIT reflectivity model. The left columns show the fitted vertical two-way column abundances of methane (X_{CH4}) and ammonia (X_{NH3}), while the middle columns show the derived values of cloud-top pressure (p_{cloud}) and ammonia abundance (f_{NH3}). The right column shows maps of the ammonia abundance computed with the HILL and FIT methods, and further corrected for cloud top pressure variations using the $\alpha(p)$ correction factor (Equation 11), described on Section 3.

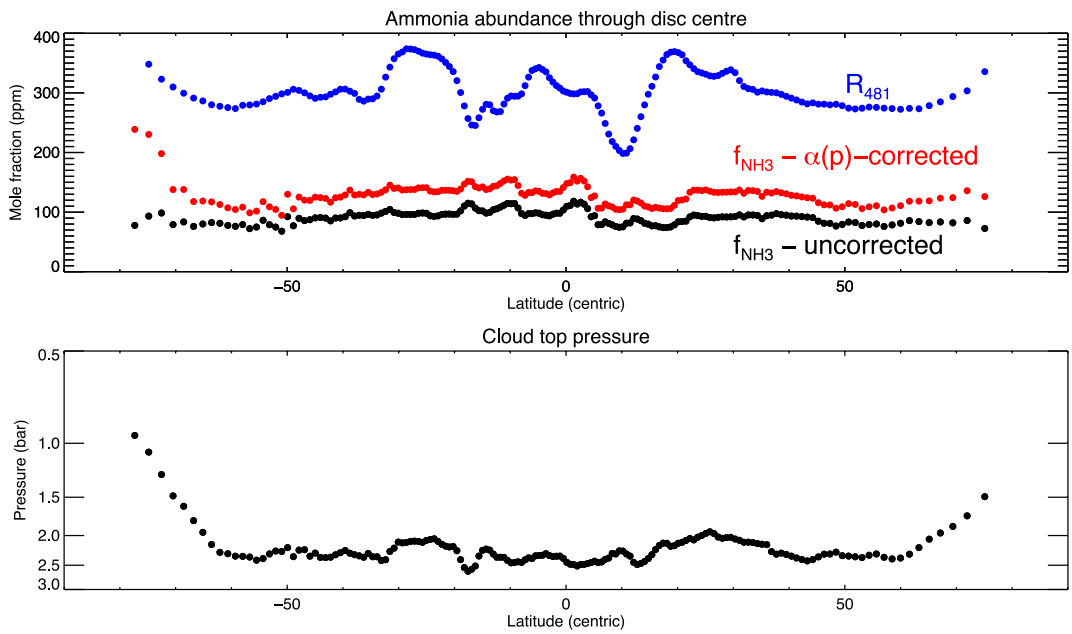

Figure 6. Latitudinal variation of ammonia abundance (f_{NH3}) (top panel) and cloud-top pressure (p_{cloud}) (bottom panel) along the center of Jupiter's disc (line marked in Figure 4), determined from our VLT/MUSE observations using the FIT reflectivity model. The top panel shows the original values of f_{NH3} (black), the $\alpha(p_{cloud})$-corrected values (red), and the central-meridian blue reflectivity at 481 nm (arbitrarily scaled) for reference. The cloud-top pressure correction factor, $\alpha(p)$ (Equation 11), used to correct f_{NH3}, is discussed in Section 3.

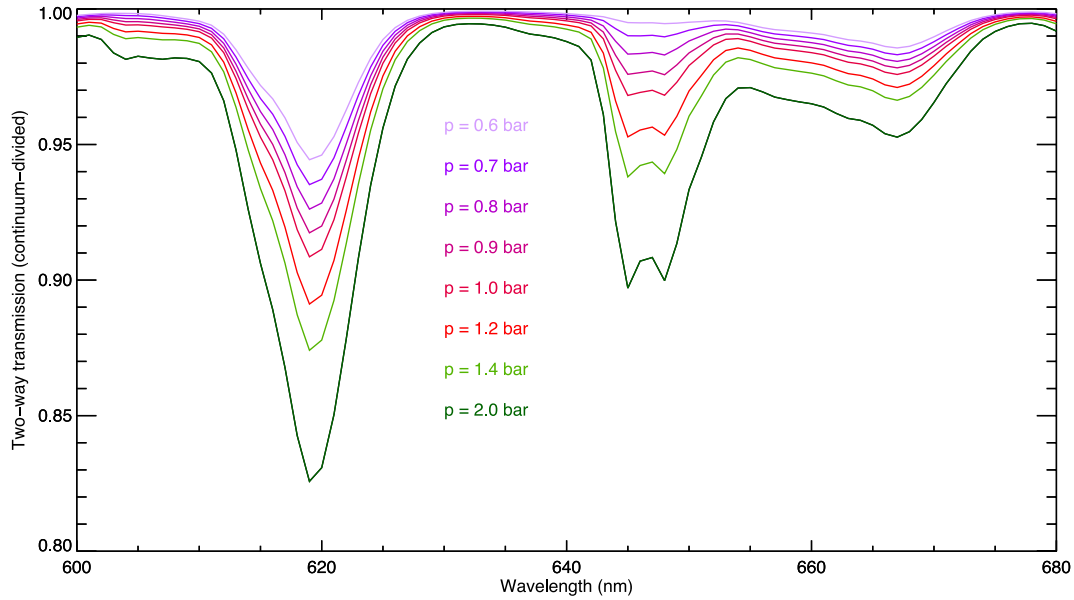

Figure 7. Normalized two-way nadir transmission in our Jupiter aerosol-free atmospheric model down to varying pressure levels. Here, to make the absorption bands clearer, we have divided the calculated transmission spectra including Rayleigh-scattering opacity, methane and ammonia absorption by the spectra calculated including Rayleigh-scattering opacity only. The methane band can be seen to be clearly present throughout the range of pressures plotted (0.6–2.0 bar), but the ammonia band at 647 nm only becomes visible at $p > 0.7$ bar as it condenses above this level.

based on that determined from the Galileo entry probe and for composition assumes $He/H_2 = 0.155$, $f_{CH4} = 1.81 \times 10^{-3}$, and the "deep" mole fraction of ammonia is $f_{NH3} = 200$ ppm, limited to the saturated vapor pressure curve at pressures less than its condensation level at ~0.7 bar. As can be seen in Figure 7 the absorption of methane increases steadily with pressure, while the absorption of ammonia is only visible for pressures greater than 0.7 bar, since it condenses at lower pressures. From the calculated two-way transmission spectra we can calculate the equivalent widths of the methane (W_{CH4}) and ammonia (W_{NH3}) absorption bands and we plot these as a function of base pressure in Figure 8. Here, we see more clearly that W_{NH3} only starts to grow for $p > 0.7$ bar, but the values of both W_{CH4} and W_{NH3} only match the values seen in our equatorial MUSE spectrum (Figure 3) of 2.248 and 0.838 nm, respectively, when $p \sim 2.5$ bar. This pressure is consistent with our p_{cloud} values.

2.3. Limb-Darkening Constraints

The great advantage of our MUSE data over observations made with, for example, a long-slit spectrometer, is that we can use IFU observations to examine the center-to-limb (CTL) variation of the spectra at different latitudes, which can give unique and strong constraints on the cloud-scattering properties of an atmosphere (e.g., Irwin, Teanby, Fletcher, et al., 2022; Irwin et al., 2021). If the Jovian clouds have a well-defined upper "cloud top", expected by the Reflecting Layer Model (RLM), then we would expect the absorption band depth (or equivalently the column abundances) of both gases to increase as we near the limb because of the increased path lengths encapsulated by the geometric factor, $\eta = 1/\mu + 1/\mu_0$. Hence, we would expect maps of both τ_{CH4} and τ_{NH3} (or equivalently X_{CH4} and X_{NH3}) to be limb-brightened. Instead, away from the anomalous poles, we find that τ_{CH4} decreases slightly toward the limb, while τ_{NH3} appears even more limb-darkened. This can be seen more clearly in Figure 9, where we have determined the equivalent widths of the methane and ammonia absorptions from our MUSE observations on 23 March 2020 in a 2°–wide latitude band centered at the equator, and plotted these against the airmass factor, η. Here, both absorptions show limb-darkening, not limb-brightening, while the ratio of the two absorptions, W_{CH4}/W_{NH3} increases quasi-linearly with η, indicating that the ammonia band depth decreases more rapidly toward the limb than the methane band depth. This shows two things:

1. First, it is clear that the Jovian clouds do not have a well-defined cloud top, otherwise we would see limb-brightening, not limb-darkening. In reality, the clouds/hazes extend upwards with a certain scale height above the cloud base and so as we view at higher zenith angle we are not able to see quite as deep into the

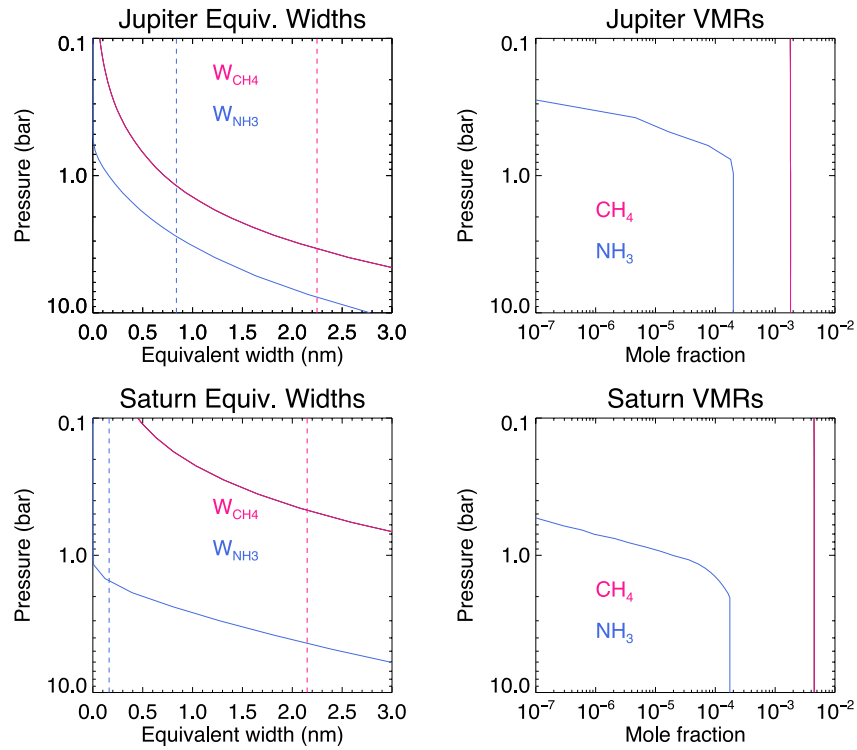

Figure 8. Comparison of calculated variation of equivalent widths of the 619-nm methane (W_{CH4}) and 647-nm ammonia (W_{NH3}) bands with the pressure of a reflecting layer in our reference Jupiter model (top left) and Saturn model (bottom left), for aerosol-free conditions. Also shown are the methane and ammonia mole fraction profiles assumed for Jupiter (top right) and Saturn (bottom right), where it can be seen that ammonia condenses at ~0.7 bar in Jupiter's atmosphere, and at ~1.8 bar in Saturn's. In the equivalent width profiles (left column) the vertical dashed lines show the observed center-of-disc equivalent widths of these absorptions observed in Figures 3 and 20, respectively. For Jupiter it can be seen that the observed equivalent widths both meet the modeled curves at a pressure of ~2.5 bar. However, for Saturn, the methane equivalent widths intersect at ~0.5 bar, while the ammonia equivalent widths intersect deeper in the atmosphere at ~1.5 bar. This is discussed later in Section 5.

atmosphere as we do at nadir. This will reduce the depth of the absorption bands, as we see, although the effect is partially counter-balanced by the increased path length through the overlying layers at higher zenith angle. The observed limb-darkening thus contains information on the vertical distribution of aerosols.

2. The second insight again concerns the location of the main cloud/haze deck on Jupiter. If the main clouds on Jupiter were based at the ammonia condensation level at ~0.7 bar then, since the ammonia mole fraction falls rapidly with height above this level, we would expect the ammonia absorption to fall much more rapidly with zenith angle than the methane absorption. Although this effect is partially seen in Figure 9, we will show in Section 3 that the increase of W_{CH4}/W_{NH3} with η is not steep enough to be consistent with the main clouds being at the ammonia ice condensation level. Note that if both ammonia and methane were well mixed we would not expect W_{CH4}/W_{NH3} to vary with airmass at all.

3. Validation of Filter-Averaged Determinations With Formal VLT/MUSE Jupiter Retrievals

To validate the determinations of ammonia mole fraction, f_{NH3}, and p_{cloud} from the band-depth approximation, we compared them with formal retrievals of the same MUSE spectra using our NEMESIS (Irwin et al., 2008) radiative transfer and retrieval model. We analyzed the observations in latitudinal bands of width 2°, sampled every 1° (to achieve Nyquist sampling) and approximated the center-to-limb variations seen at each wavelength using the Minnaert model (Minnaert, 1941):

$$(I/F) = (I/F)_0 \mu_0^k \mu^{k-1}. \quad (8)$$

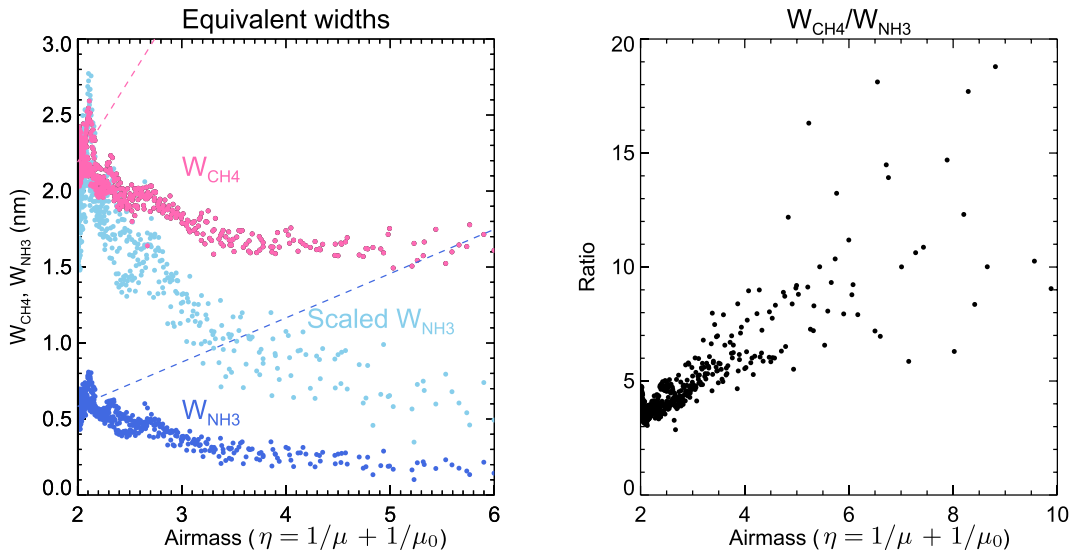

Figure 9. Variation of the 619-nm CH_4 and 647-nm NH_3 absorption equivalent widths with airmass factor $\eta = 1/\mu + 1/\mu_0$ in the latitude band 1°S to 1°N in Jupiter's atmosphere from VLT/MUSE observations. Left: Variation of equivalent width of methane (W_{CH4}) and ammonia (W_{NH3}) with η. The expected variation from a Reflecting Layer Model with $X \propto \eta$ is shown by the dashed lines, which is totally inconsistent with the observations. In addition, we also show the W_{NH3} values roughly scaled to match W_{CH4} at $\eta = 2$ to highlight the fact that W_{NH3} falls more rapidly with η than W_{CH4}. Right: Observed variation of W_{CH4}/W_{NH3} with η. If both ammonia and methane were well mixed then W_{CH4}/W_{NH3} should not vary with η.

Here, μ and μ_0 are again the cosines of the viewing and solar zenith angles, respectively, $(I/F)_0$ is the fitted nadir reflectance, and k the fitted limb-darkening parameter. The reflectance, I/F, is the observed radiance at each location, I, divided by the radiance reflected from a perfectly reflecting Lambertian surface. The Minnaert model is found to match the observed center-to-limb variations very well. Following Irwin et al. (2021), Alexander (2024) use the fitted $(I/F)_0(\lambda)$ and $k(\lambda)$ spectra in each latitude band to reconstruct the averaged observed spectra at two zenith angles (both viewing and solar) of 0° and 61.45°, respectively, and fitted to both spectra simultaneously. The first angle is clearly nadir, while the second angle has a two-way airmass of ~4 and corresponds with another of the five zenith angles in the Gauss-Lobatto quadrature scheme we use in our matrix operator multiple-scattering code, following the formalism of Plass et al. (1973). We have found that fitting two spectra simultaneously like this constrains much more strongly the scattering properties of the unknown aerosols in giant planet atmospheres (Irwin, Teanby, Fletcher, et al., 2022; Irwin et al., 2021). For our aerosol model, we used a two-layer model based on that used by Alexander (2024), which has a detached aerosol layer centered at ~0.2 bar, and a deeper, vertically extended cloud, centered and fixed at ~1.4 bar. In both cases, these peak pressures are in terms of the specific density (particles/gram) profile and both aerosol layers are assumed to have a Gaussian distribution of specific density with respect to the log(pressure) vertical ordinate, which from the hydrostatic relation is proportional to altitude. Since the composition of the particles is unknown we retrieve spectra of their imaginary refractive indices, reconstructing the real refractive indices using the Kramers–Kronig relation for a range of trial real refractive indices at a reference wavelength of 875 nm. The scattering properties are calculated from the resulting complex refractive index spectra together with best estimates for the particle size distributions using Mie theory. This approach is strictly valid only for spherical particles, which is not the case for the ice particles expected in Jupiter's atmosphere. However, the scattering properties of randomly orientated nonspherical particles can to first order be approximated by a Mie model, and in our approach the computed phase functions are approximated by Henyey-Greenstein functions, which average over features that are unique to spherical particles, such as the "rainbow" and "glory." This model has been used successfully in several recent studies (e.g., Irwin et al., 2021; Irwin, Teanby, Fletcher, et al., 2022) and although it is an approximation, it has the advantage that it is self-consistent in terms of its computed cross-section, single-scattering albedo and phase function spectra.

For this study, we analyzed the same MUSE observations shown earlier, made on 23 March 2020 at 08:59UT. For direct comparison with the band-depth determinations we made new fits to the 600–680 nm region only, fitting for

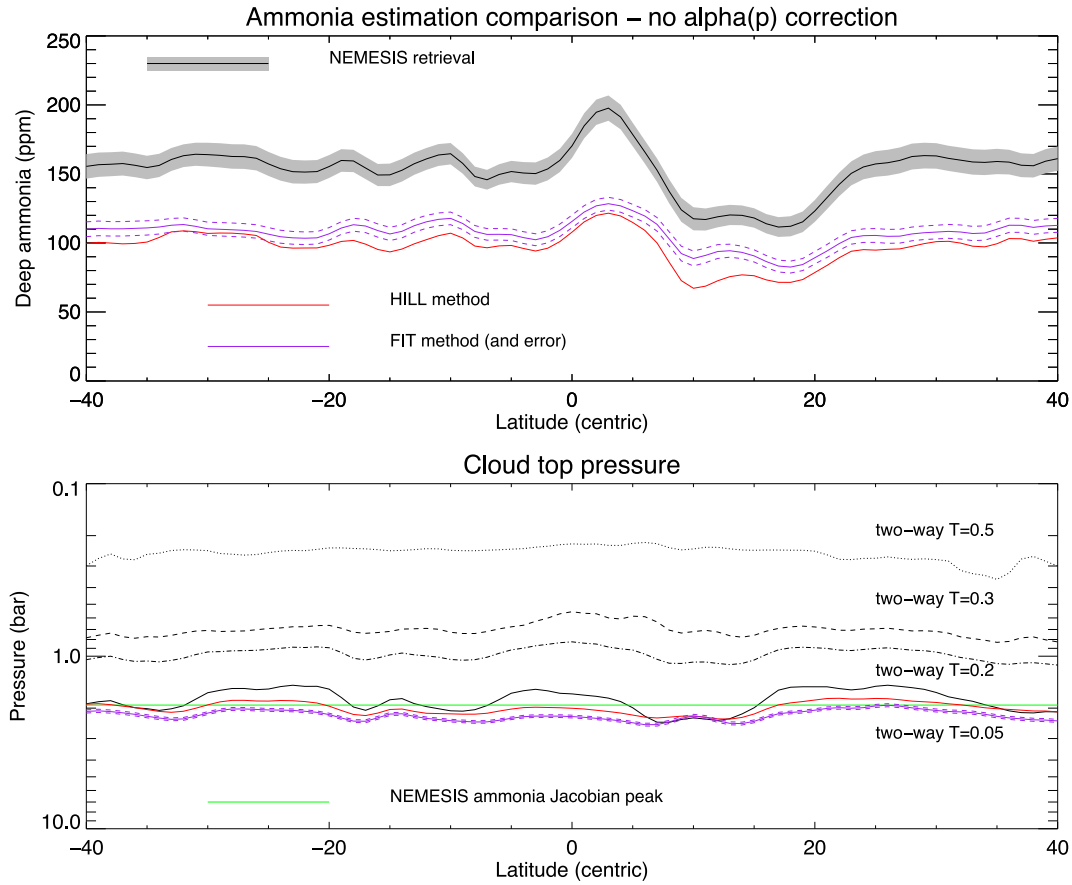

Figure 10. Comparison of retrieved values of the ammonia mole fraction (top panel) and cloud-top pressure (bottom panel) from Jupiter VLT/MUSE observations. In the top panel, the NEMESIS-retrieved deep ammonia mole fraction is plotted (with error) as a function of latitude and compared to values of f_{NH3} determined with the band-depth approximation method using different approaches: (a) analysis of MUSE reflectance spectra averaged using SCT filter profiles (HILL method); and (b) analysis of MUSE reflectance spectra using the FIT method. The bottom panel shows different estimates of the cloud-top pressure, described in the text.

the opacity of the two aerosol layers, the width of the deeper layer, the imaginary refractive index spectrum of the particles in the deep layer and the deep mole fraction of ammonia. Alexander (2024) describe the results when applied to the whole MUSE wavelength range simultaneously, but these retrievals also have to fit the chromophore absorption at short wavelengths and the haze reflection in the 890-nm methane band, where haze reflection is most clearly identifiable. In addition, although the same ammonia absorption data (Coles et al., 2019) are used at all wavelengths, the absorption of ammonia gets stronger at longer wavelengths and so the ammonia bands probe lower pressures. Hence, simultaneous fitting to the whole MUSE range leads to a slightly different balance between the fitted parameters to optimize the fit. By restricting ourselves here to the 600–680 nm region, we use a single band of ammonia and can compare our retrievals "like-for-like" with the band-depth approximation method. The imaginary refractive index spectrum of the particles in the upper layer was set to that derived by Alexander (2024) and its width was similarly fixed to a small value ($\Delta p/p = 0.2$). The ammonia profile used was a simple "step" model, with a constant mole fraction pressures greater than the condensation level and then decreasing with height following the saturated vapor pressure curve (i.e., 100% relative humidity) computed from our prior temperature-pressure profile used to model Cassini/CIRS observations of Jupiter (Irwin et al., 2004). The a priori deep ammonia mole fraction was set to 200 ppm, but was entirely free to vary in our retrieval model. The resulting retrieved deep ammonia mole fraction as a function of latitude is shown in Figure 10. Here we can see a retrieved mean ammonia mole fraction of ∼160 ppm, rising to a maximum of ∼190 ppm at 5°N and then decreasing to minimum of ∼110 ppm in the NEB at 10–20°N. A similar latitudinal variation of ammonia mole fraction was derived from MUSE observations by Braude et al. (2020) and also by Alexander (2024), but both

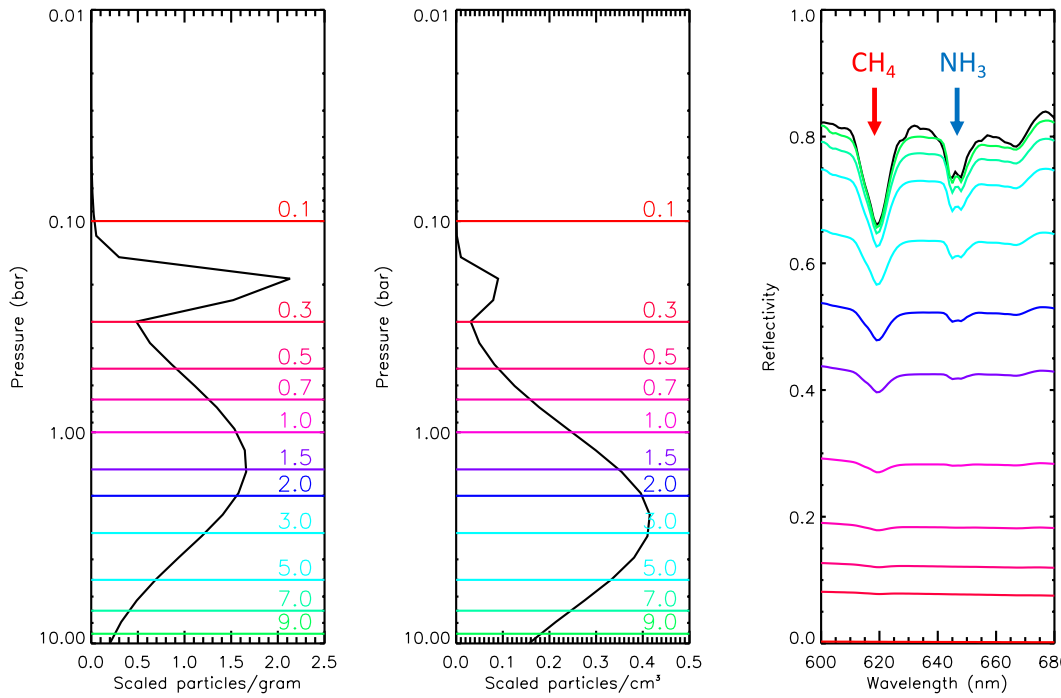

Figure 11. NEMESIS simulations with opaque non-reflecting base added at a range of pressures to the model that has been fitted to nadir equatorial VLT/MUSE spectrum of Jupiter. Left and middle panels shows retrieved two-component cloud model in units of particles/gram and particles/cm^3, respectively, with one cloud/haze centered at 1.4 bar in specific density and the other centered at 0.2 bar, together with the range of pressures for the bottom non-reflecting layer. Right-hand panel shows measured nadir spectrum (black) with range of simulations from our best fit model with non-reflecting base added at the pressures shown in other panels and shown with the same color. As we go deeper into the atmosphere, the reflectance increases, as expected, and the methane and ammonia bands can be seen to deepen, but for ammonia this band (at 647 nm) is only significant at pressures greater than the condensation pressure of ∼0.7 bar.

studies, which analyze the whole 475–933 nm MUSE range, find lower mean abundances of ∼60 ppm. This discrepancy is due to the additional difficulties in analyzing the whole MUSE range simultaneously, as previously mentioned, where the retrieval is trying to fit the ammonia signature over a very wide range wavelengths, and thus absorption strengths, while simultaneously fitting the aerosol opacities and particle scattering properties, to model the chromophore effects in the main cloud and also the variation of upper atmospheric haze, which is best determined near 890 nm (Alexander, 2024; Braude, 2019; Braude et al., 2020).

Reliably defining a cloud-top pressure from our retrievals is difficult in a scattering model with vertically extended clouds. As a first approximation, we show in Figure 10 the pressure level where the two-way nadir transmission to space at 625 nm has values of 0.5, 0.3, 0.2, and 0.05 respectively, using the extinction opacities of the aerosol layers and Rayleigh-scattering opacity, but no multiple scattering. As can be seen the corresponding pressure levels are approximately 0.25, 0.7, 1, and 1.8 bar, respectively. So where, then, should we say the cloud "top" is? In reality, the particles are highly scattering and, from their assumed size of ∼1 μm, also quite forward-scattering at these wavelengths. In addition, conservative Rayleigh scattering from the air molecules themselves is significant at these wavelengths. Hence, light can scatter down to and be reflected from layers much deeper than might be expected from such simple extinction optical depth calculations.

To extract a more meaningful estimate of the cloud top pressure, we fitted our two-component vertical cloud profile to the nadir spectrum at the equator, retrieving the opacity and width of the lower layer, the opacity of the upper layer (with fixed width with $\Delta p/p = 0.2$), together with the imaginary refractive index spectra of the two components. Once fitted, we then computed forward-modeled spectra when an additional non-reflecting opaque vertically thin layer was added at various pressures. The results are shown in Figure 11. First of all, in Figure 11 we can see that although we assume our deep aerosol to peak at 1.4 bar in terms of specific density (i.e., particles/gram) the retrieved layer is not infinitely thin, but has a significant width and thus contributes to the total

reflectivity over a wide range of pressures. In addition, we see that in terms of number density (particles/cm^3) the layer peaks closer to 3 bar, which is more consistent with the estimated $p_{\rm cloud}$ values. Hence, as the pressure of the additional opaque layer increases, we can see smoothly increasing reflection from the overlying hazes and the depth of the methane band steadily increases right to the bottom of our atmosphere, which in this simulation was set to 10 bar. In contrast, the ammonia band only starts to appear for $p > 0.7$ bar. Clearly the methane band feature is formed over a very wide range of pressures in our simulation, which means that it is difficult to assign a simple, single cloud top pressure. We also computed the Jacobians for cloud and ammonia, where the Jacobian is the rate of change of radiance with respect to either cloud specific density (particles/gram) or ammonia mole fraction at each pressure level. Both are found to peak strongly at 2 bar (shown in Figure 10), but this is driven mostly by the fact that the aerosol profile peaks near these levels. Our simulations did not determine meaningful variation of the Jacobians with latitude since the peak pressure of the lower cloud was assumed to be fixed. Light is able to penetrate to and be reflected to such deep levels in our model because gaseous absorption is very low away from the absorption bands and Rayleigh scattering is conservative. Because we can potentially see to such great depths the retrieval of aerosol profiles is extremely difficult and degenerate using the 600–680 nm alone and further analysis is beyond the scope of this paper.

In Figure 10, we compare our formal NEMESIS-retrieved values of ammonia mole fraction and inferred cloud-top pressure with the values of $f_{\rm NH3}$ and $p_{\rm cloud}$ determined from our two implementations of the band-depth approximation. As can be seen, the latitudinal variation of $f_{\rm NH3}$ was found to be very similar to the latitudinal variations of the NEMESIS-retrieved deep ammonia mole fractions for both band-depth approximations used, but the abundances were found to be too small by a factor of ∼1.5. Once again, the cloud-top pressure $p_{\rm cloud}$ is determined to be 2–2.5 bar at all latitudes, which corresponds very well with peaks of both the cloud opacity and ammonia Jacobians. Hence, remarkably, although the observed center-to-limb (CTL) variations show that Jupiter's clouds do not have a well-defined cloud top, the derived cloud-top pressures closely match the values determined from a full multiple-scattering retrieval analysis, and similarly the derived ammonia abundances closely match the retrieved deep abundance variations of our simple "step" ammonia profile, albeit with a different scaling factor.

To interpret why our band-depth determinations of $f_{\rm NH3}$ are systematically smaller than our NEMESIS retrievals, we need to remember that the formula we used to compute $f_{\rm NH3}$ (Equation 4) assumes that both CH_4 and NH_3 have the same vertical distribution of mole fraction. In reality, we know that the ammonia mole fraction reduces rapidly above its condensation level at ∼0.7 bar, which is ∼30 km above the ∼2-bar "cloud-top" level. This altitude difference is of the same order as the scale height of Jupiter's atmosphere (∼25 km) and thus it is unsurprising that our band-depth $f_{\rm NH3}$ values are systematically smaller. In addition, the rapid reduction of ammonia mole fraction above its condensation level is also responsible for the different limb-darkening of the methane and ammonia bands seen earlier in Figure 9. To quantify these two distinct effects we took our reference Jupiter atmospheric model and computed the nadir column abundances of CH_4 and NH_3 down to the various pressure levels in our model, $X_{\rm CH4}(p)$ and $X_{\rm NH3}(p)$. In the next two subsections we use these calculated $X_{\rm CH4}(p)$ and $X_{\rm NH3}(p)$ curves to quantify both the center-to-limb variation, and also the observed $f_{\rm NH3}$ scaling offset.

3.1. Center-To-Limb Variation

If we assume a certain "cloud-top" pressure, p_0, for the nadir observation of the methane equivalent width, $W_{\rm CH4}$, then as we approach the limb we can use the observed reduction of $W_{\rm CH4}$ with airmass, η, to determine the path abundance actually observed and convert this to the equivalent vertical path abundance $\tilde{X}_{\rm CH4}(\eta)$ using our modeled nadir column abundance curve, $X_{\rm CH4}(p)$:

$$\tilde{X}_{\rm CH4}(\eta) = \frac{\eta_0 W_{\rm CH4}(\eta)}{\eta W_{\rm CH4}(\eta_0)} X_{\rm CH4}(p_0), \tag{9}$$

where η_0 is the nadir airmass factor, equal to 2.0. Comparing $\tilde{X}_{\rm CH4}(\eta)$ with $X_{\rm CH4}(p)$ we can then compute the actual pressure level sounded, $p(\eta)$, at these higher zenith angles and look up the corresponding vertical path abundance of ammonia above this level, $X_{\rm NH3}(p(\eta))$. We can then calculate the expected equivalent width of ammonia at this airmass factor:

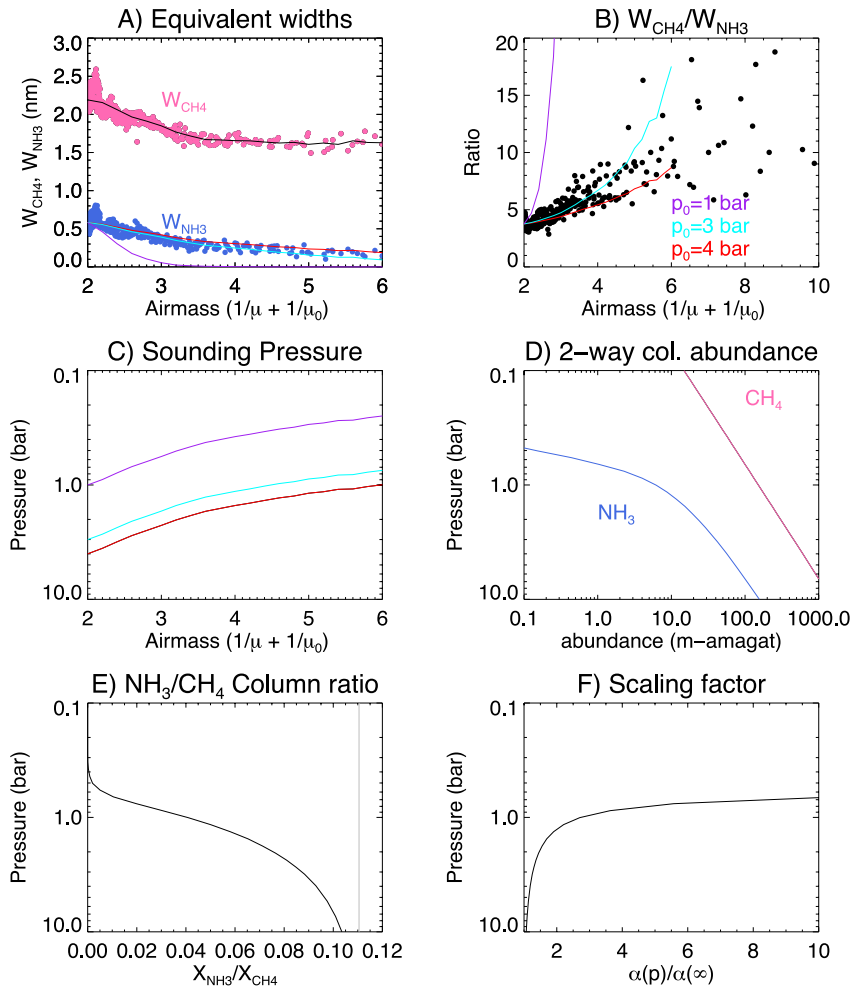

Figure 12. Top row repeats Figure 9, showing the variation of the 619-nm CH_4 and 647-nm NH_3 absorption band strengths and band strength ratio (W_{CH4}/W_{NH3}) with airmass factor $\eta = 1/\mu + 1/\mu_0$ at Jupiter's equator from VLT/MUSE. In both panels the colored lines show the expected variation of W_{NH3} and W_{CH4}/W_{NH3} with η, respectively, computed from the smoothed variation of W_{CH4} with η (shown in black), depending on the assumed nadir pressure level p_0 observed, which are here set to 1, 3, and 4 bar. These assumed nadir pressures and calculated variation with airmass are shown in Panel C and are computed from the pressure variation of the two-way methane column abundance from our reference Jupiter atmosphere, shown in panel D. The ammonia two-way column abundance is also plotted in panel D, which decreases rapidly above ammonia's condensation level at ~0.7 bar. Panel E shows the variation of ammonia/methane column abundances (i.e., X_{NH3}/X_{CH4}) as a function of pressure, compared with the asymptotic value at infinite pressure of $f_{NH3}/f_{CH4} = 2 \times 10^{-4}/1.81 \times 10^{-3} = 0.11050$. Panel F shows the computed correction factor $\alpha(p) = (f_{NH3}X_{CH4})/(f_{CH4}X_{NH3})$, which has a value of unity at depth, and increases as pressure decreases.

$$\tilde{W}_{NH3}(\eta) = \frac{\eta X_{NH3}(p(\eta))}{\eta_0 X_{NH3}(p_0)} W_{NH3}(\eta_0). \tag{10}$$

Taking the observed, smooth variation of W_{CH4} with η (shown in Figure 12a as the black line) we computed the expected airmass dependence of W_{NH3} for three values of p_0: 1, 3 and 4 bar. Our simulated variations with airmass of W_{NH3} are shown in Figure 12a, while the simulated variations with airmass of W_{CH4}/W_{NH3} and $p(\eta)$ are shown in Figures 12b and 12c, respectively. As can be seen the agreement between this simple model and the observations is best for p_0 = 3–4 bar, which is moderately consistent with the values of p_{cloud} determined earlier. Figure 12c shows that at higher angles we probe to lower pressure levels, where the column abundance of ammonia (Figure 12d) starts to decrease more rapidly with altitude, depending on the choice of p_0. Hence, W_{CH4}/W_{NH3} increases more rapidly with η as p_0 is reduced. The fact that the center-to-limb variations of W_{CH4}

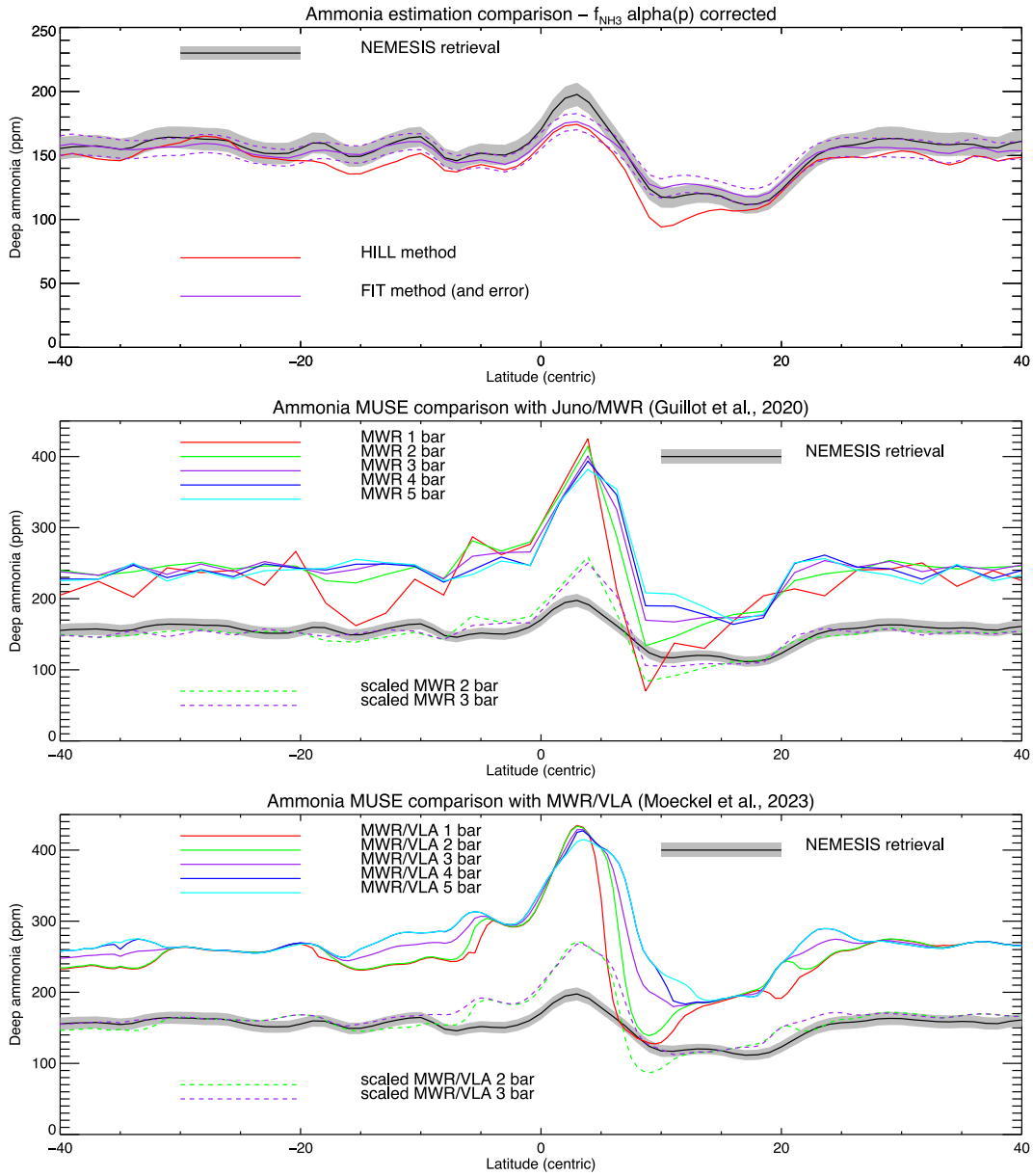

Figure 13. Top plot shows the revised variation of band-depth fitted ammonia mole fraction f_{NH3} with latitude, corrected for variations in cloud-top pressure using the $\alpha(p)$ factor (Equation 11) and compared with the formal MUSE NEMESIS retrievals. Middle plot compares the MUSE NEMESIS retrievals with the ammonia mole fractions retrieved at several pressure levels from Juno MWR observations (Guillot, Li, et al., 2020), while the bottom plot compares the MUSE NEMESIS retrievals with the ammonia mole fractions retrieved at the several pressure levels from the combined VLA/MWR analysis of Moeckel et al. (2023) (including clouds). In the bottom two plots, the MUSE and MWR/VLA variations have very similar latitude variations, but are offset from each other by a factor of ∼1.6. Also plotted are the MWR/VLA results at 2 and 3 bar re-scaled by this factor of 1.6 to lie over the MUSE variations, allowing easier comparison.

and W_{NH3} are more consistent with deeper values of p_0 (i.e., > 2 bar) adds further evidence that the bulk of reflection from Jupiter's aerosol layers is from levels well below the ammonia condensation level.

Although we have treated p_0 as a tunable parameter to explore the parameter space of limb-darkening in Figure 12, we might expect from our two-way transmission calculations (Figures 7 and 8) that it should be strongly constrained by $W_{\mathrm{CH4}}(\eta_0)$ to be ∼2.5 bar. Larger or smaller values of p_0 would be expected to lead to methane equivalent widths that are significantly different from those observed (Figure 8). However, in a scattering atmosphere we can see from Figure 11 that the equivalent width of the methane 619-nm band is less than

would be expected from a Reflecting Layer Model since this approximation does not account for reflectivity already added from upper layers. These contributions from upper levels partially "fill in" the absorption band, lowering its equivalent width. Hence, we should view $p_{\rm cloud}$ as a lower limit for the main pressure levels of reflection, which then makes $p_{\rm cloud}$ more consistent with the values of p_0 that give the best match to the observed CTL variations (Figure 12).

We should also note that the synthetic curves in Figure 12 assume the ammonia mole fraction profile is that contained in our reference Jovian atmosphere, which has a constant value of 200 ppm at depth, and then decreases along the saturated vapor pressure curve at pressures less than the condensation level at ~0.7 bar. If the ammonia profile actually starts falling with height at pressures deeper than 0.7 bar, due to the formation of NH_4SH, or perhaps a "mushball" NH_3-H_2O cloud, for example, then $X_{\rm NH3}(p)/X_{\rm CH4}(p)$ would start to decrease with altitude at even greater pressures. This would then imply from the observed variation of $W_{\rm CH4}/W_{\rm NH3}$ with η that p_0 should be even greater. In other words, if NH_3 is depleted below the condensation level, we are probing the ammonia abundance at even deeper pressures.

3.2. Systematic Offset Between Band-Depth Approximation and Retrieved Ammonia Abundances

In Figure 12d, we have already shown the calculated column abundances of methane and ammonia, $X_{\rm CH4}$ and $X_{\rm NH3}$, above different pressure levels in our reference Jupiter atmosphere. If both gases had the same constant mole fraction profiles, then $X_{\rm NH3}/X_{\rm CH4}$ would be constant with height and equal to $f_{\rm NH3}/f_{\rm CH4}$. As can be seen in Figure 12e, the actual column abundance ratio approaches a constant value at high pressure, but falls rapidly as we move up toward the ammonia condensation level. Hence, if we wish the band-depth approximation ammonia determinations of $f_{\rm NH3}$ to match the "deep" ammonia abundances determined from the NEMESIS retrievals, $f_{\rm NH3:Deep}$, we need to multiply $f_{\rm NH3}$ by a pressure-dependent scaling factor, $\alpha(p)$:

$$\alpha(p) = \frac{f_{\rm NH3:Deep}}{f_{\rm CH4}} \frac{X_{\rm CH4}(p)}{X_{\rm NH3}(p)}. \tag{11}$$

This pressure-dependent scaling factor is shown in Figure 12f and at a pressure level of ~2 bar it can be seen that $\alpha(p) \sim 1.5$, which is precisely the factor needed to reconcile the band-depth approximation ammonia abundances with the NEMESIS-retrieved deep ammonia mole fractions. Hence, if we compute $f_{\rm NH3}$ and $p_{\rm cloud}$ using either of the band-depth approximations, we can use the derived $p_{\rm cloud}$ estimates to calculate factors $\alpha(p_{\rm cloud})$ and use these to correct our ammonia abundances. We have included panels showing these pressure-corrected $f_{\rm NH3}$ distributions across Jupiter's disc in Figures 5 and 13 show the revised latitudinal variation of the pressure-corrected $f_{\rm NH3}$ determinations compared with the formal NEMESIS retrievals, showing the remarkably close agreement between the values when corrected for $\alpha(p)$, with the FIT method agreeing more closely than the HILL values, which are slightly too small.

3.3. Summary of Retrieval Validation

For zonally averaged MUSE observations we have seen that the simple HILL band-approximation method yields determinations for ammonia abundance that are remarkably consistent with formal NEMESIS multiple-scattering retrievals, with the more sophisticated FIT method (which requires resolved reflectivity spectra rather than filter-averaged reflectivities) agreeing more closely. The formal NEMESIS retrievals use a full multiple-scattering code, which is very slow, making it impractical to perform full multiple-scattering retrievals on wide-area, spatially resolved observations. However, the band-approximation HILL and FIT methods are computationally very efficient and since we have validated these with our zonally averaged MUSE observations, we can be much more confident that the spatial variations of ammonia and cloud seen when applying the HILL method (which can be done with observations made by amateur astronomers) or the FIT method (which requires spectral imaging observations, currently only accessible by professional astronomers) to Jupiter observations reveal real variations in Jupiter's atmosphere that indicate how the atmosphere of Jupiter circulates on very small scale lengths. In the next section we analyze our MUSE observations with the FIT band-approximation model over small scales to reveal clues on the circulation at finer scales, including at the northern edge of the EZ, and over the Great Red Spot.

4. Interpretation of Spatial Variations of Ammonia and Cloud Revealed in Jupiter's Atmosphere

Having shown that the band-depth approximation HILL and FIT methods reliably determine the abundance of ammonia in the 2–3 bar pressure range, a number of spatial features are revealed in these MUSE observations, which we discuss here.

4.1. Ammonia Latitudinal Distribution and Comparison With Juno/MWR

We previously noted the similarity of the latitudinal variation of ammonia abundance determined by VLT/MUSE and that determined from the Microwave Radiometer (MWR) on board the NASA Juno spacecraft. Our retrievals from the 600–680 nm region are compared in detail with Juno observations in Figure 13, where we compare to the MWR analysis of Li et al. (2017) and Guillot, Li, et al. (2020), and also the combined MWR and VLA analysis of Moeckel et al. (2023), for pressure levels between 1 and 5 bar in both cases. As can be seen the VLA-MWR and MUSE determinations have very similar variations with latitude, but the MUSE abundances are systematically smaller by a factor of ∼1.6. One possibility is that there is a systematic offset between the ammonia absorption coefficients assumed in the 647-nm band and those assumed in the MWR-VLA inversions, but it is also possible that there are systematic errors in the MUSE determinations, which are co-dependent on the assumed vertical cloud structure, and assume a simple "step" profile for ammonia abundance that does not vary with depth below its condensation level at ∼0.7 bar. If the true Jovian atmosphere had more opacity of high-altitude aerosol than we find in our current retrievals, then this might partially "fill in" the ammonia absorption band, but have less of an effect on the methane band leading to lower apparent abundance of ammonia. However, in preliminary simulations where we tried to model the effect of additional upper level hazes filling in the ammonia band, we found we could not fit the spectra as well and achieved only modest increases in the retrieved deep ammonia abundance. Another possibility is that the ammonia abundances we retrieve with MUSE at 2–3 bar are less than those sounded at deeper pressures due to ammonia being depleted by the formation of another cloud, such as NH_4SH or aqueous ammonia. For example, for a standard Jovian atmosphere with generally accepted deep Jovian composition of: O/H, S/H = 5 × solar; N/H = 5.5 × solar; and C/H = 4.8 × solar, Irwin (2009), finds the ammonia abundance to decrease from 280 ppm below the NH_4SH cloud at ∼2 bar to 178 ppm, above. This a reduction by a factor of 1.6, which, perhaps coincidentally, is exactly the factor of difference between the MUSE and MWR-VLA retrievals. Hence, the discrepancy between MUSE and MWR might be because MUSE is more sensitive to the ammonia abundance above an NH_4SH cloud at ∼2 bar, while MWR and VLA are more sensitive to the abundance below. However, Moeckel et al. (2023) explore several different scenarios for interpreting the MWR-VLA observation, and although they note there is considerable degeneracy, they do not find compelling evidence for a decrease in ammonia abundance at an NH_4SH condensation level. In addition, other MWR studies (Guillot, Li, et al., 2020; Li et al., 2017) even find that at 5°N the retrieved abundance of ammonia increases as the pressure decreases. We note, however, that both these findings are contrary to an analysis of the Galileo Probe radio signal strength (Folkner et al., 1998), which found that the ammonia mole fraction increases smoothly with pressure from 2–8 bar, before then decreasing slightly from 8–16 bar, which suggests that there is indeed some process depleting ammonia in the mid-troposphere. Whatever systematic offsets remain between the MUSE and MWR-VLA determinations, we can see in Figure 13 that the latitudinal variations of the MUSE determinations are most consistent with MWR and MWR-VLA at the 2–3 bar pressure level, which again agrees well with our previous determinations of the pressure level probed in our observations.

4.2. Ammonia Variations at Northern Edge of the EZ

The abundance of ammonia is found to peak sharply at the northern edge of the EZ at a latitude of ∼5°N, but has large spatial variations, which can be seen in Figure 5, where strong f_{NH3} and p_{cloud} peaks appear to coincide with dark bluish regions seen at visible wavelengths, known as North Equatorial Dark Features, or NEDFs (Rogers, 2019). The spatial correspondence between these features can be seen more easily in Figure 14, where for three representative sample dates within our MUSE data set the variations have been projected onto a cylindrical grid from 40°S to 40°N, and 50°E to 50°W of the central meridian. The variations on 23 March 2020 over the GRS and a large NEDF at the EZ/NEB boundary can be seen more clearly in the zoomed-in plots shown in Figure 15. In Figures 14 and 15, it can be seen that the high values of p_{cloud} coincide exactly with the NEDFs, while f_{NH3} is found to be high in the NEDFs, especially over the southern and eastern edges of these features, but low to the west of them, coinciding with the northern edge of the bright "plume" regions seen in the visible

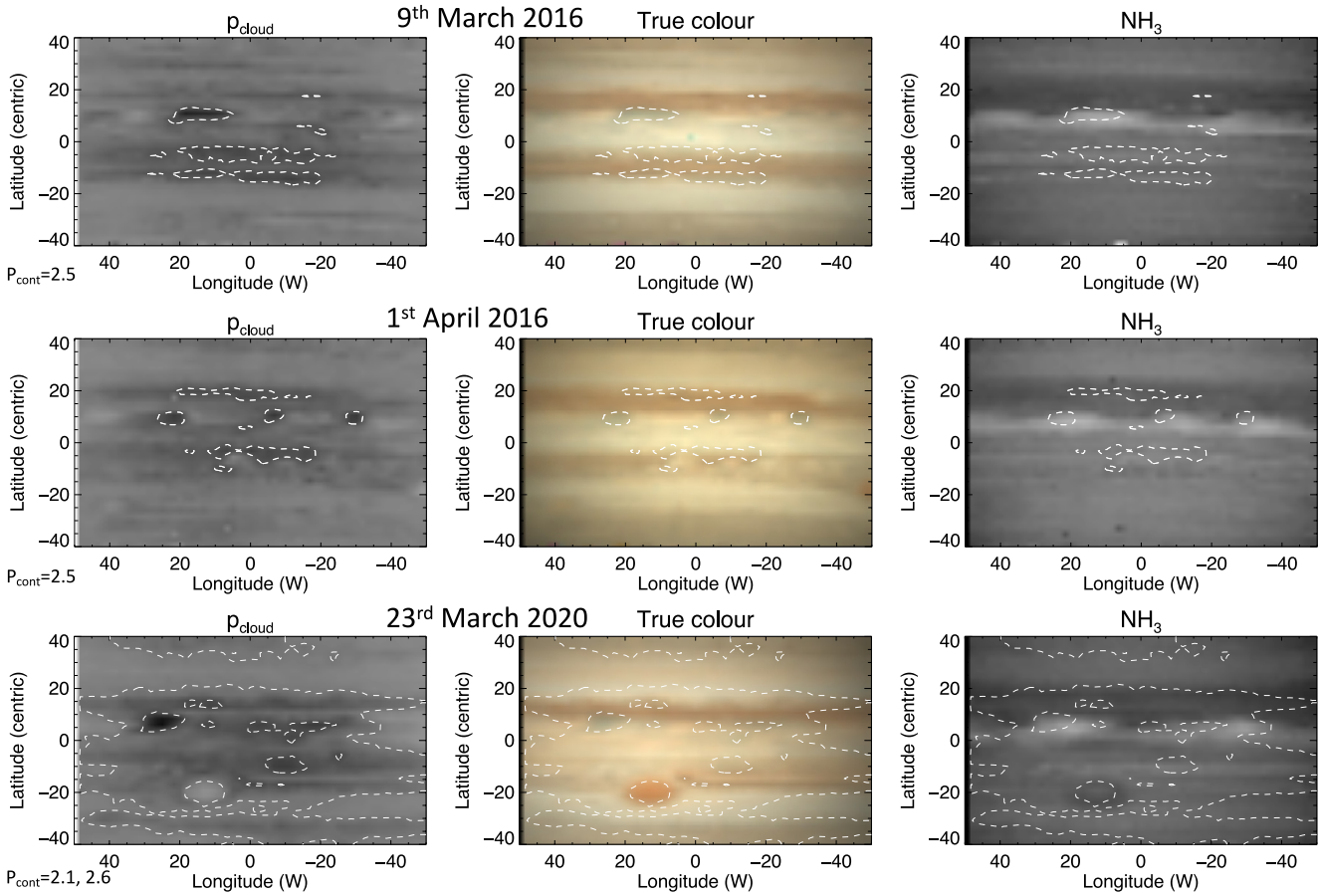

Figure 14. Projected variation of ammonia abundance (f_{NH3}) and cloud-top pressure (p_{cloud}) near the center of disc for selected dates in the VLT/MUSE archive. The left hand column shows the derived maps of p_{cloud}, with contours at $p = 2.5$ bar indicated for the 2016 observations and contours marked at $p = 2.6$ and 2.1 bar for the 23 March 2020 observation. The middle row shows a true non-gamma-corrected color image from the MUSE cube for reference, including the p_{cloud} contours. As can be seen NEDF regions, which appear dark and bluish in the color image are well correlated with regions of high p_{cloud}. The right column shows the associated ammonia mole fractions f_{NH3}. Here, we can see that f_{NH3} is high to the south and east of the NEDFs and low to the north and west.

images. NEDFs appear very bright at wavelengths near 5 μm, where thermal emission from pressure levels as deep at ~10 bar can escape to space if there is a low opacity of overlying cloud, and so these NEDF regions are also known as "5-μm hotspots." The dynamics of NEDFs has been the subject of much study (e.g., Choi et al., 2013) and they are seen to have dark streaks extending southwest into the EZ, called "festoons", which are less bright at 5 μm, but which can still be seen in Figures 14 and 15 to have elevated ammonia abundances and deeper p_{cloud} values. Our determination here of high values of p_{cloud} in NEDFs is consistent with a clearing of clouds in these regions, which allows light to penetrate deeper before being Rayleigh-scattered by the air itself, or scattered from deeper hazes. The bluish tinge of the NEDFs can be seen more quantitatively in Figure S4 in Supporting Information S1, where we have plotted the spectra of several sample regions from our observations on 23 March 2020, which are indicated in Figure S3 in Supporting Information S1.

Although observations from the Galileo orbiter were severely handicapped by the main communication antenna not deploying fully, a few continuous spectra were returned from the Galileo/NIMS instrument over a few regions, including the set of four "real-time" spectra, targeting a single "5-μm hotspot", mentioned in the introduction. In these spectra, Irwin et al. (1998) found there to be a strong correlation between the ammonia absorption (visible near 1.5 and 2.0 μm) and the 5-μm flux, with brighter regions at 5-μm (and thus thinner clouds) coinciding with lower ammonia absorption. However, Roos-Serote et al. (1998), analyzing 5-μm spectra of several hot spots, found that the deep ammonia abundance was correlated with hot spots, with elevated ammonia abundance seen on the southern halves of these features, which is more consistent with our findings. EZ plumes and hotspots were also mapped using Gemini/TEXES and Juno/MWR by Fletcher et al. (2020), who found that

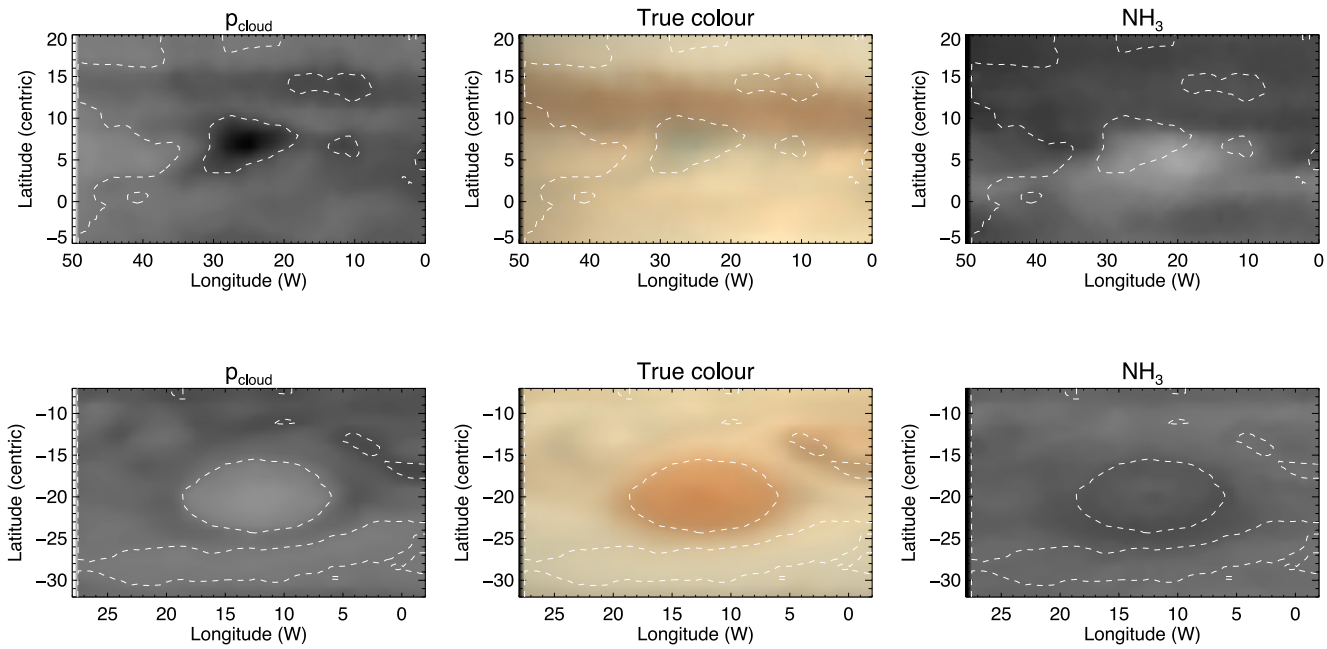

Figure 15. Projected variation of ammonia abundance (f_{NH3}) and cloud-top pressure (p_{cloud}) near the GRS and NEDF on 23 March 2020. The left hand column shows the derived maps of p_{cloud}, with contours at $p = 2.6$ and 2.1 bar. The middle row shows a true non-gamma-corrected color image from the MUSE cube for reference, including the p_{cloud} contours. The right column shows the associated ammonia mole fractions f_{NH3}.

the NEDFs were generally depleted in upper-tropospheric (440 mb) ammonia compared the neighboring plumes, but that there was substantial variability in ammonia content within and between the different hotspots. For the plume regions to the west and southwest of NEDFs, these were found to coincide with low ammonia, while the regions to the east and southeast were found to coincide with high ammonia, just as we find here. Similarly, Keck observations at 5-μm in 2017 found low ammonia abundance to the east of NEDFs (Bjoraker et al., 2022). The low abundances of ammonia detected in the bright plume regions to the west of NEDFs is surprising as detailed images of such regions sometimes reveal them to be convectively active. It is possible that such regions are where ammonia ice clouds form, and that the reflection from these clouds partially "fills in" the ammonia absorption band and thus low values of f_{NH3} over plumes may be an indirect indication of ammonia ice clouds. However, the correspondence of our maps at 2–3 bar here, with those of Gemini/TEXES (Fletcher et al., 2020) suggests that ammonia may really be depressed in the plumes to the west and southwest of NEDFs.

Given that some studies have found NEDFs to be regions of low ammonia, while here we find elevated f_{NH3}, we decided to re-examine the assumptions underpinning our results to see if the observed ratio of column abundances, X_{NH3}/X_{CH4}, could perhaps be interpreted differently. Might it be, for example, that we conclude higher f_{NH3} values in the NEDFs because the clouds are thinner and so we can see deeper? Also, we have assumed that the pressure-temperature profile is the same at all locations, which is a major simplification (Fletcher et al., 2020). Finally, we have assumed that although the ammonia profile has a variable deep abundance, the mole fraction does not vary with height until the ammonia condensation level, above which the mole fraction falls according to the saturation vapor pressure. If the ammonia profile really is the same shape as we assume, then our $\alpha(p_{cloud})$ factor should correct f_{NH3} for these p_{cloud} variations. But what if the ammonia profile does not have this shape? What if the mole fraction of ammonia increases with pressure below the ammonia condensation level, as seen in the Galileo probe observations, due perhaps to the formation of an NH_4SH cloud, or another mechanism? If the ammonia profile is different from what we have assumed then, we would have to recompute the $\alpha(p)$ correction curve (Figure 12), which would lead to larger values in the 2–3 bar range and also an increase in the rate of change of $\alpha(p)$ with pressure. In extremis, if the 1–5 bar region were heavily depleted in ammonia, then, since the atmosphere is very scattering, light at ammonia-absorbing wavelengths could scatter down to very deep levels before experiencing any absorption; this would lead to the 647-nm ammonia band forming at much deeper pressures than the 619-nm methane band, which, as we'll see in Section 5 is what we find to be the case in Saturn's atmosphere.

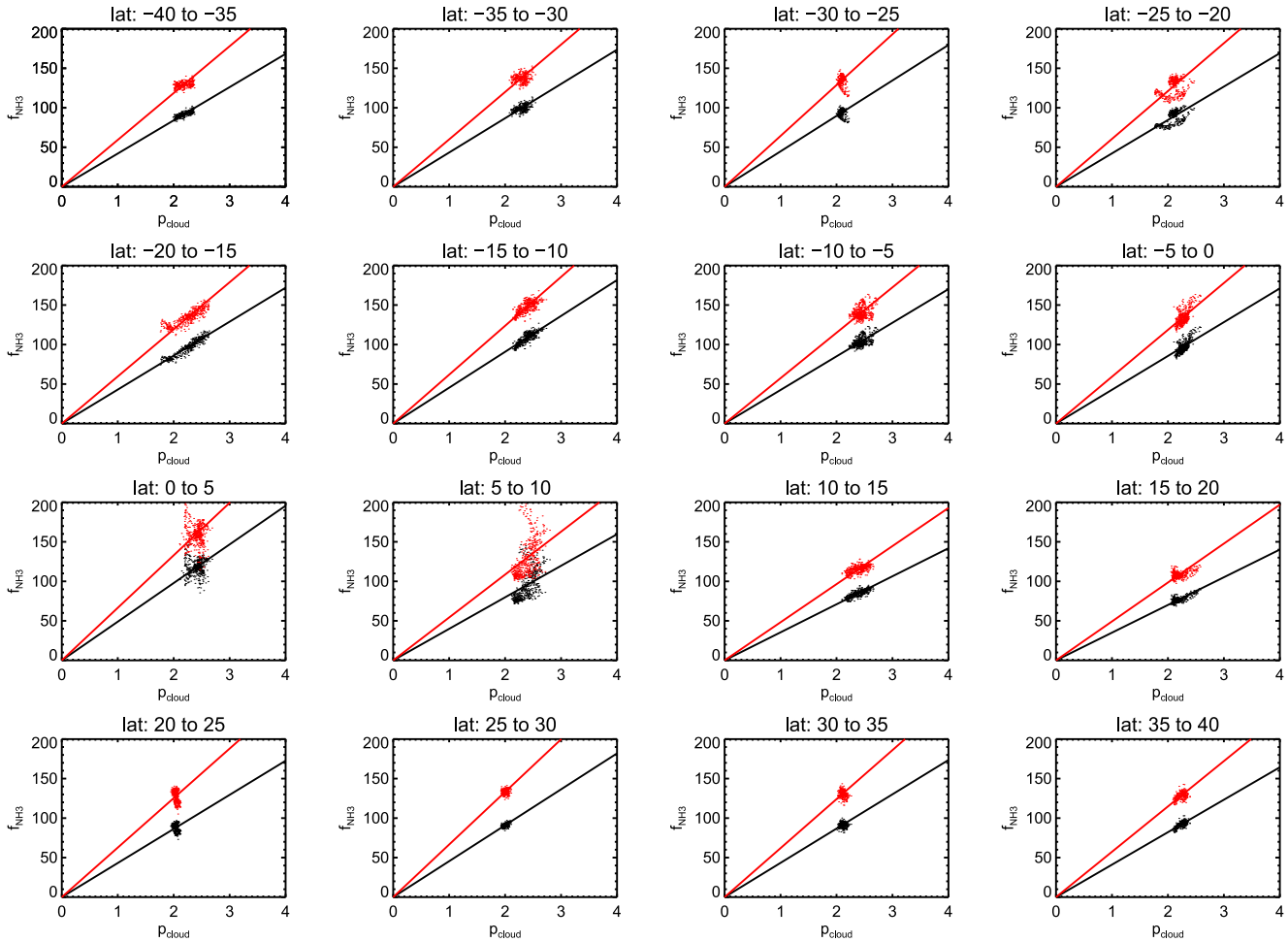

Figure 16. Correlation between FIT ammonia abundance (f_{NH3}) and cloud-top pressure (p_{cloud}) along Jupiter's central meridian (±20° longitude) in 5°–wide bins from 40°S to 40°N. The black points show uncorrected f_{NH3} values, while the red points show $\alpha(p)$-corrected values. The straight lines show linear fits through the origin to the data in each latitude band. In some latitude bands there is very little variation of p_{cloud}, but in bands where this quantity varies, f_{NH3} can be seen to increase moderately linearly with p_{cloud}, although at many latitudes the correlation is not very strong. The anomalous behavior in the 20–25°S band is due to the presence of the GRS. Figure S9 in Supporting Information S1 plots the correlations for points in longitudes 0–20°E, only, where the anomalous points can be seen to disappear. The spread in points in the 0–5°N and 5–10°N bands are due to the presence of NEDFs, which are clearly anomalous regions of the atmosphere.

To explore whether the ammonia profile shape might be different from what we have assumed, we looked at the correlation between our derived f_{NH3} and p_{cloud} values in 5°-wide latitude bins spread along the central meridian (±20° longitude), and show our results in Figure 16. Here, we can see that in latitude bands where p_{cloud} varies significantly the calculated f_{NH3} values (with or without the $\alpha(p_{cloud})$ correction) are moderately well correlated with p_{cloud}, with the line of best fit moderately consistent with a line passing through the origin. It may be that these correlations are physically real, and that regions of high p_{cloud} coincide with regions of elevated ammonia abundance, but these correlations may also reveal that our assumed ammonia profile is incorrect. Unfortunately, to explore this fully requires that we analyze spectral information from as wide a wavelength range as possible to determine aerosol and ammonia profiles that are simultaneously consistent with all observations, but this is beyond the scope of this paper as we have already explained. In the meantime, if we assume that this correlation is an artifact of using an inappropriate ammonia profile, then to a first order we can correct for it by multiplying our f_{NH3} values by a factor p_{ref}/p_{cloud}, where p_{ref} is any convenient pressure level we might like to choose and p_{cloud} is the locally inferred cloud top pressure. Assuming $p_{ref} = 2$ bar, which is typical of the lower pressures covered in Figure 16, we corrected the f_{NH3} maps over the NEDF and GRS shown in Figure 15 and show our revised maps in Figure 17. Here, we can see that f_{NH3} is now low over the whole of the NEDF, remaining low to the west, but is still high to the southeast as previously determined. This is more consistent with the mid-infrared retrieval

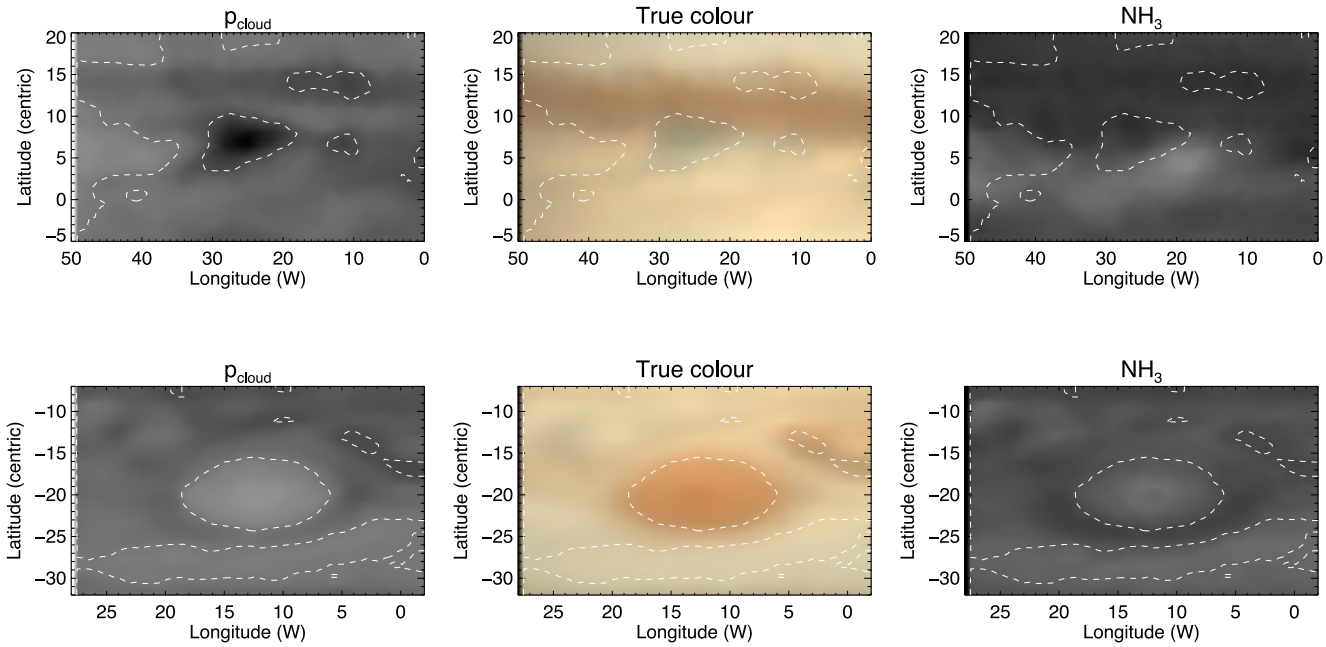

Figure 17. As Figure 15, but for ammonia abundances that have been corrected for p_{cloud} correlation to a reference pressure of p_{ref} = 2 bar (i.e., they have been multiplied by p_{ref}/p_{cloud}). With this correction, we can see low f_{NH3} over the NEDFs and increased values in the GRS, which are results that are more in line with expectations from other observations.

analysis of Fletcher et al. (2020) and also with Juno/MWR observations that find NEDFs to be bright and thus ammonia depleted. However, the absolute accuracy of these maps depends on the shape of both the temperature and ammonia abundance profiles and cannot be addressed any further here. For completeness, Figure S5 in Supporting Information S1 shows the global maps of f_{NH3} (Figure 5) when the additional p_{ref}/p_{cloud} has been applied. Similarly, Figure S6 in Supporting Information S1 reproduces Figure 6, including the latitudinal variation of f_{NH3} along the disc center when scaled by p_{ref}/p_{cloud}.

4.3. Ammonia and Cloud Variations Over the Great Red Spot

The band-depth-derived ammonia abundance in Jupiter's Great Red Spot (GRS), using the FIT method, was found to be slightly depleted in Figure 5, which is more clearly seen in Figure 18, where we have plotted the variation of f_{NH3} and p_{cloud} along a line (shown in Figure 4) passing vertically through the center of the GRS, centered at 20°S in planetocentric coordinates. It might be thought that the lower apparent ammonia abundance in the GRS arises because the thicker clouds in the spot mask the 647-nm ammonia absorption band. However, p_{cloud} is not seen to be drastically less inside the GRS and dividing the X_{NH3} map by the X_{CH4} map and applying the $\alpha(p_{cloud})$ factor should correct for this, assuming the vertical profile of ammonia is as we have assumed (Section 4.2). However, we can also not rule out the possibility that increased reflection from an aerosol component at pressures <1 bar, may again partially "fill in" the ammonia absorption band, leading to lower apparent values of f_{NH3}. Across the GRS, our analysis shows that f_{NH3} in the GRS increases slightly from south to north and that there is a ring of minimal ammonia abundance around the edge, visible in Figures 15 and 18. If we correct for f_{NH3}–p_{cloud} correlation (by multiplying by p_{ref}/p_{cloud}, Section 4.2) then in Figure 17 we can still see a ring of minimal ammonia abundance around the edge, but higher abundances in the core. In Figure 19 the $\alpha(p)$-corrected (but not p_{ref}/p_{cloud}-corrected) ammonia map derived with the FIT method and shown previously in Figure 5f has been inverted and reprojected on to a cylindrical map to compare with a map of X-band (8–10 Gz) brightness temperature recorded by the Very Large Array in 2016, and shown as Fig. 1 of Moeckel et al. (2023). The VLA map shows the brightness temperature differences of the thermal emission, where absorption by ammonia pushes the emitting level up to lower pressures where it is cooler. Thus in the VLA map (and in the inverted MUSE map) ammonia-rich areas are dark. The pressure region sampled at these VLA frequencies is estimated by Moeckel et al. (2023) to be 1–2 bar, which is very similar to our estimate for the MUSE sounding level and it can be seen that there is very good correlation between the two maps, even though considerable time has elapsed between the VLA map

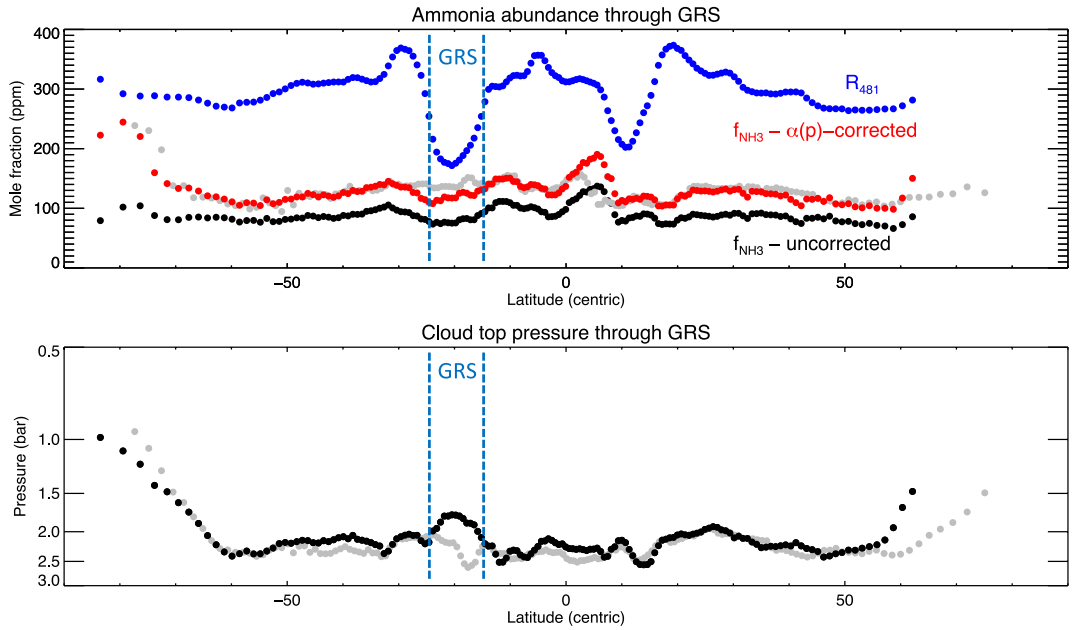

Figure 18. Variation of ammonia abundance (f_{NH3}) (top panel) and cloud-top pressure (p_{cloud}) (bottom panel) with latitude along a vertical line in the VLT/MUSE cube (shown in Figure 4) passing through the center of the Great Red Spot (GRS) at 22°S, determined using the FIT model. For reference, the top panel also shows the central-meridian blue reflectivity (481 nm), arbitrarily scaled, and both panels show the corresponding variations along the vertical line through the disc center (in gray) of $f_{NH3}[\alpha(p)\text{-corrected}]$ and p_{cloud}, shown previously in Figure 6. The top panel includes both uncorrected, and $\alpha(p)$-corrected values. The approximate northern and southern boundaries of the GRS are indicated by the blue dashed lines.

recorded in 2016 and the MUSE map observed in 2020. In both maps, we can see the enhanced ammonia at the northern edge of the EZ as a dark belt, and depletion in the NEB as a brighter zone. In addition, in both the VLA and VLT/MUSE maps the GRS is visible as a slightly brighter region (indicating lower ammonia abundance) bounded by an even brighter annulus (indicating even lower ammonia). In addition, a darker region (indicating enhanced ammonia) is visible to the north of the GRS in both maps. Hence, the ammonia abundances derived from MUSE observations of the visible reflection spectrum from 600–680 nm show remarkable consistency with determinations of X-band thermal emission by VLA at similar pressure levels. N.B., versions of Figures 18 and 19

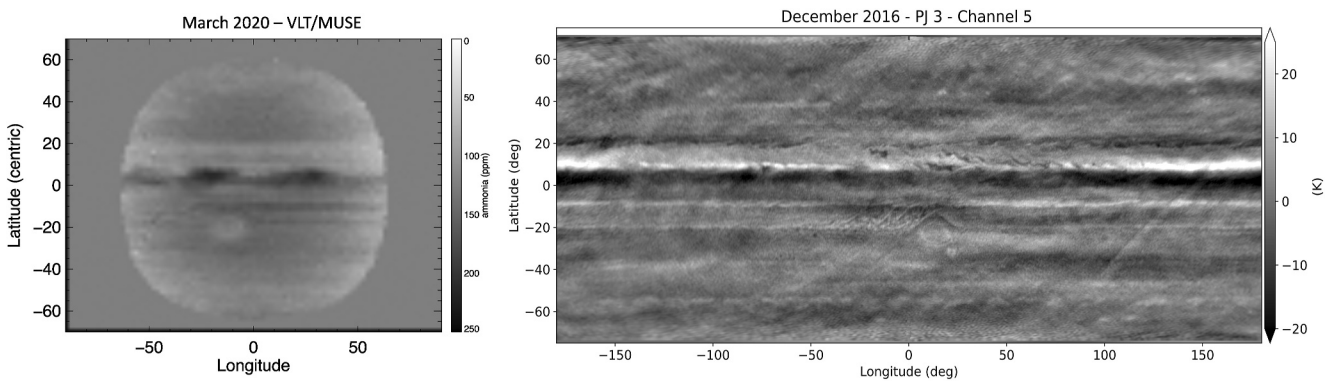

Figure 19. Comparison of VLT/MUSE band-depth approximation ammonia determinations with the Very Large Array (VLA). Left hand panel shows ammonia map derived with the FIT method from March 2020 observations, previously shown in Figure 5F, but here with the gray-scale reversed and projected onto a cylindrical grid of latitudes and central-meridian longitudes. Here, areas that are rich in ammonia are dark, while ammonia-poor regions are bright. The NEDFs are visible as dark regions at 5N, while the GRS appears bright, with a slightly brighter annulus around its edge. Right hand panel reproduces, with kind permission of the authors, the underlying data presented in Figure 1 of Moeckel et al. (2023), showing an X-band map (8–10 GHz) of Jupiter recorded by the VLA in December 2016. Dark regions indicate more ammonia absorption and the pressure region sounded in the X-band is estimated by Moeckel et al. (2023) to be 1–2 bar. The correlation between the VLT/MUSE and VLA maps is good, especially around the GRS, where a brighter annulus around the edge is also seen. In addition, a darker region (indicating enhanced ammonia) is visible to the north of the GRS in both VLT/MUSE and VLA determinations.

including the additional p_{ref}/p_{cloud} scaling are shown in Figures S7 and S8 in Supporting Information S1, respectively.

An analysis of Cassini/CIRS thermal emission observations of Jupiter from 7 to 17 μm (Irwin et al., 2004), probing the upper troposphere at ~0.5 bar, found decreased ammonia humidity in the GRS, which is consistent with what we find here, although the abundance of phosphine (PH_3) appeared to be enhanced at the northern edge of the GRS. It is possible that this enhanced PH_3 region coincides with the increased ammonia abundance just north of the GRS seen by both VLT/MUSE and the VLA. However, a reanalysis of these data (Fletcher et al., 2010) found PH_3 to be uniformly enhanced within the GRS, perhaps due to the elevated aerosols shielding the molecule against photolysis. More recent ground-based observations of Jupiter's thermal emission spectra (5–20 μm) with the TEXES instrument at NASA's Infrared Telescope Facility (IRTF) in Hawaii, also reveal a depletion of upper tropospheric ammonia within the GRS at 440 mb (Fletcher et al., 2016), and also a north-south asymmetry, which was previously noted by Fletcher et al. (2010), while later observations made in 2020 with the same instrument mounted at Gemini-North (Fletcher et al., 2016) also show a ring of low ammonia about the GRS, with interior values (which are generally lower than the average at the GRS latitude) increasing from south to north. In addition, Juno/MWR finds increased ammonia in the central to north GRS at $p <$ ~10 bar (Bolton et al., 2021). Hence, the ammonia variations we find here at 2–3 bar at visible wavelengths also appear to be consistent with variations found in the upper troposphere (~0.5 bar) by thermal emission and Juno/MWR observations.

4.4. Variation of Ammonia and Cloud Toward Poles of Jupiter

The band-depth approximation finds increased abundances of ammonia toward Jupiter's poles, but it is hard know if this is reliable since we can also see that p_{cloud} decreases rapidly toward the poles. The ammonia two-way column abundance map (Figure 5) shows the same limb-darkening toward the poles as along the equator and it is mostly when the ammonia abundance f_{NH3} is corrected for p_{cloud} that we see enhanced polar values (Figure 6). Lower p_{cloud} may be caused by a thickening of the main haze/cloud, but it might also be caused by a thickening of the upper haze layer centered at ~0.2 bar, caused perhaps by auroral processes, which will also suppress both W_{CH4} and W_{NH3}. Unfortunately, without a more in-depth radiative transfer analysis that considers the measured spectra at all wavelengths, not just 600–680 nm, it is not possible to tell which scenario is more likely. Such a study is again beyond the scope of this paper.

5. Application of Filter-Averaged Ammonia Determinations to Saturn Observations

Having demonstrated that band-depth approximation methods give remarkably reliable estimates of the cloud top pressure and the ammonia abundance below the ammonia condensation level in Jupiter's atmosphere, when compared with retrievals from a multiple scattering radiative transfer code, we wondered if the same technique could also be applied to MUSE observations of Saturn. To do this we analyzed a VLT/MUSE observation of Saturn made on 6 April 2017, shown earlier in Figure 1, measured close to northern summer solstice and so giving us the best view possible of Saturn's north polar region.

Ammonia condenses at deeper pressure levels in Saturn's cooler atmosphere than in Jupiter's, with an expected condensation level of ~1.8 bar. The scale height in Saturn's atmosphere is also approximately twice as great as Jupiter's and so Saturn's hazes are estimated to be much more vertically extended, with base pressures exceeding 1 bar (Pérez-Hoyos & Sánchez-Lavega, 2006). Hence, the absorption of ammonia in the 647-nm band might be expected to be very much less than for Jupiter, as the cloud tops will likely be at pressures where the abundance of ammonia is already very small and falling rapidly along the saturation vapor pressure curve. However, Figure 20 shows disc-averaged and equatorial spectra of Saturn from 600–680 nm, where it can be seen that although the equivalent width of the 647-nm ammonia band is smaller than for Jupiter, with a value here at the equator of 0.163 nm, it is by no means zero. In contrast, the equivalent width of the 619-nm methane band is 2.149 nm, which similar to that of Jupiter. In Figure 21 we show the results of applying the HILL method to these MUSE reflectivity spectra, where the data have been masked to exclude Saturn's rings. To convert radiance to reflectivity the solar spectrum of Meftah et al. (2023) was again used, with the solar distance set to that of Saturn at the time of observation of 9.6866 AU. For Saturn we assume the deep mole fraction of methane to be $f_{CH4} = 4.5 \times 10^{-3}$ (Flasar et al., 2005). Although the ammonia absorption band is weak, clear latitudinal variations of f_{NH3} are seen in Figure 21, with increased abundances at the equator (~200 ppm) and also near the north pole. Also shown in

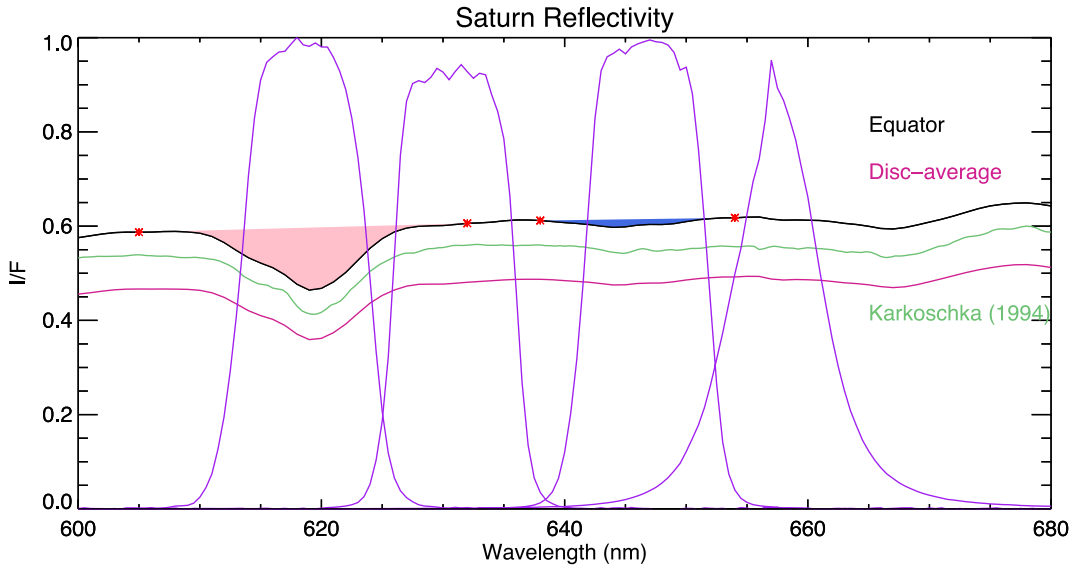

Figure 20. As Figure 3, but for Saturn, showing equatorial and disc-average VLT/MUSE reflectivity spectra of Saturn compared with the disc-averaged reflectivity spectrum of Karkoschka (1994) and filters used by Hill et al. (2024). The methane and ammonia absorption bands are shaded in pink and blue, and have equivalent widths of 2.149 and 0.163 nm, respectively.

Figure 21 is the latitudinal variation of p_{cloud}, which can be seen to have values of ~0.35 bar at the equator, increasing to ~0.5 at mid-latitudes, and increasing further to ~0.65 bar in Saturn's north polar vortex, coincident with Saturn's North Polar Hexagon (NPH). However, given that ammonia is expected to condense near 1.8 bar, how can our determination of ammonia mole fractions of ~200 ppm and cloud-top pressures of ~0.5 bar be correct?

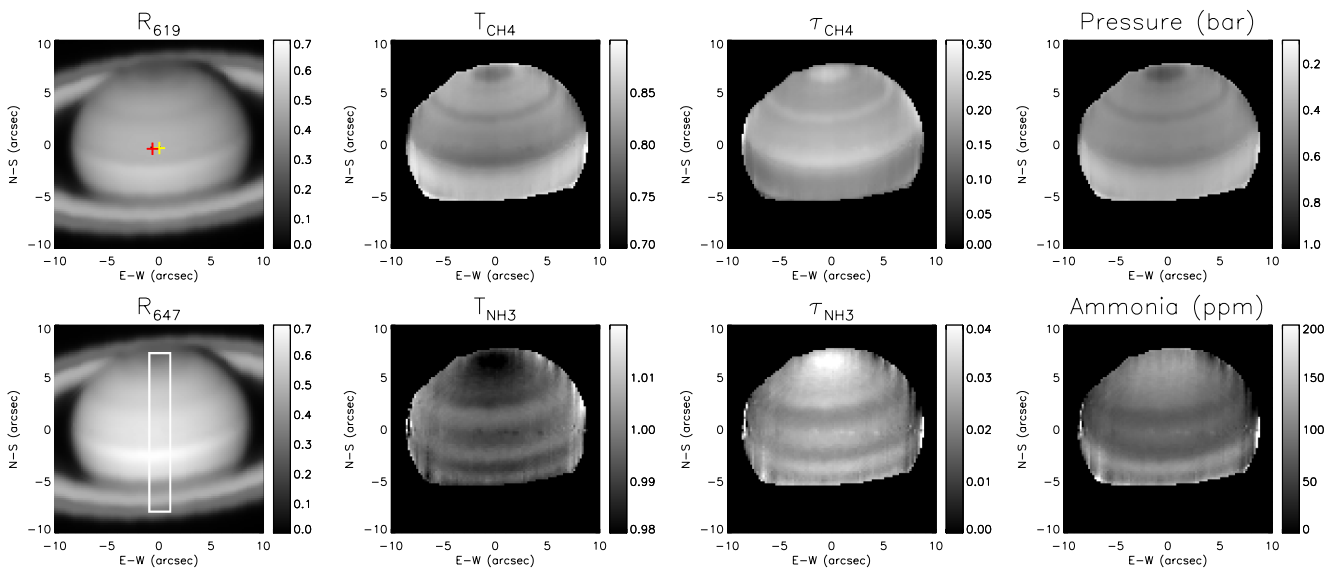

Figure 21. Example of simple band-depth approximation calculations (HILL method) applied to VLT/MUSE observations of Saturn made on 6 April 2017. The left hand column shows the observed reflectivity averaged over the 619- and 647-nm SCT filters. The second column shows the mean transmission of the methane and ammonia bands calculated from the filter-averaged reflectivities. The third column shows the calculated filter-averaged opacities, while the right-hand column shows the calculated maps of cloud top pressure (p_{cloud}) and ammonia abundance (f_{NH3}). The image at 619 nm (top left) also shows the sub-observer point (yellow cross) and the subsolar point (red cross), indicating this is a low phase angle observation. The image at 647 nm (bottom left) also outlines the region roughly along Saturn's central meridian analyzed in Figures 23 and 26.

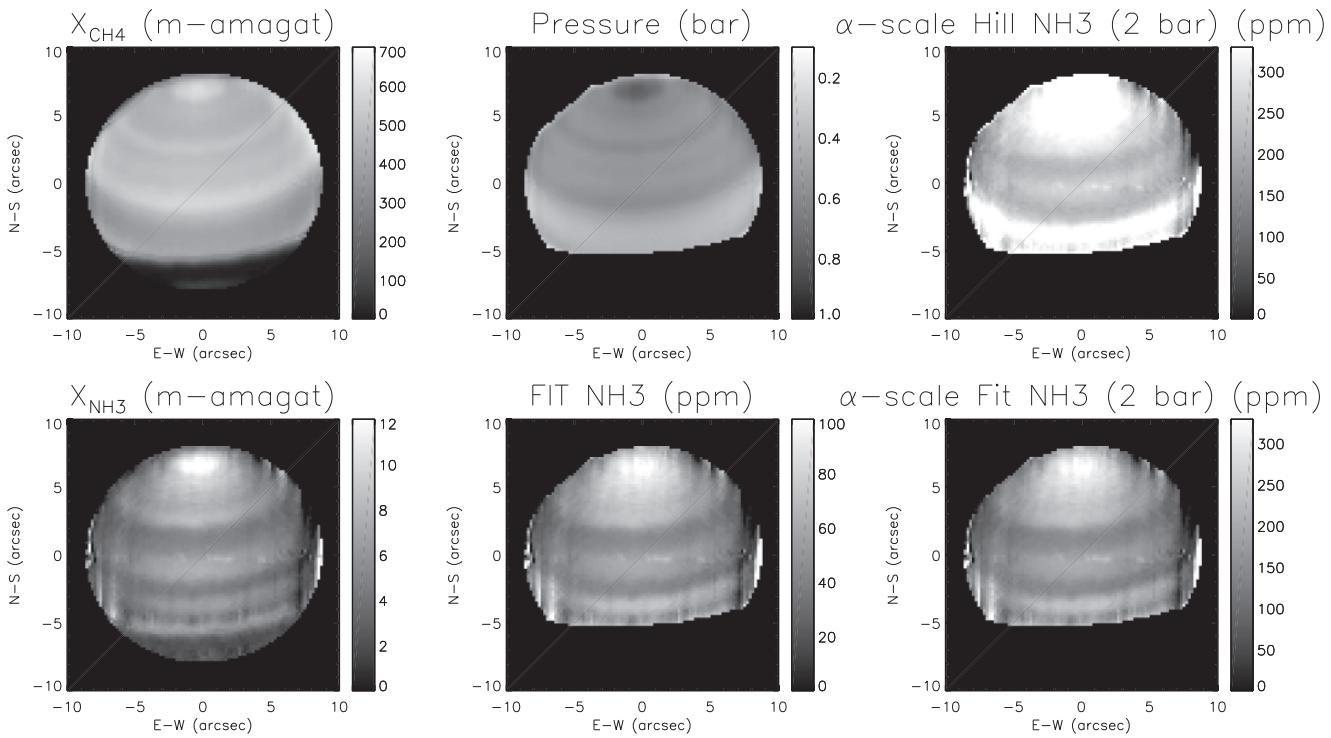

Figure 22. Similar to Figure 5, but showing the results of the analysis of the VLT/MUSE Saturn observations with the FIT reflectivity model. The left column shows the fitted vertical two-way column abundances of methane (X_{CH4}) and ammonia (X_{NH3}), while the middle columns show the derived values of cloud-top pressure (p_{cloud}) and ammonia abundance (f_{NH3}). The right column shows $\alpha(p_{cloud})$ -corrected maps (assuming a fixed pressure p_{cloud} of 2 bar) of the ammonia abundance computed with the HILL and FIT methods, respectively.

Since the 647-nm ammonia band is weaker in Saturn's spectrum (Figure 20), small differences in the continuum correction might conceivably lead to large errors in the derived f_{NH3} values using the wide filter profiles and simple HILL method. Hence, to determine the ammonia variation more accurately from these MUSE spectra we used the more sophisticated FIT method to determine the two-way column abundances of CH_4 and NH_3 directly from the measured reflectances using the continuous $k_{CH4}(\lambda)$ and $k_{NH3}(\lambda)$ absorption coefficients described earlier. Revised maps of f_{NH3} and p_{cloud} using this approach are shown in Figure 22, together with the corresponding maps of the methane and ammonia two-way column abundances X_{CH4} and X_{NH3}. The latitudinal variations determined by the FIT method can be seen more quantitatively in Figure 23, where the values of f_{NH3} and p_{cloud} have been sampled along the central meridian of the disc and plotted against latitude. The values of f_{NH3} determined from the FIT method are smaller (typically 60 ppm) than those derived from the simpler Hill method, but show a very similar variation with latitude, with minima at 10°N and 35°N, and maxima at 0°, 20° and 45°N, increasing smoothly polewards of 45°N and then decreasing slightly polewards of 70°N. Meanwhile, the cloud-top pressure p_{cloud} is found to be at a minimum value of 0.4 bar at the equator, increasing to a maximum of 0.75 bar at 15°N, reducing to ~0.6 bar at 25°N and then remaining roughly constant before slightly increasing again polewards of 70°N to ~0.7 bar near the north pole.

Before we read too much into these variations, though, we still need to reconcile the large apparent ammonia abundances with the low cloud-top pressures. Even though the new estimates of f_{NH3} of ~60 ppm are less than those derived earlier from the simpler HILL method of ~200 ppm, they are still very much greater than the expected mole fraction of ammonia at the 0.5-bar pressure level, where the ammonia mole fraction should be limited by the saturated vapor pressure curve to a value of only 0.04 ppm (using our reference Saturn atmospheric profile, which is that used by Fletcher et al., 2007). How can we possibly have such incompatible values of f_{NH3} and p_{cloud}? The answer to this is that, once again, the Reflecting Layer Model assumption underpinning the calculations of p_{cloud} is simply not applicable when modeling radiative transfer in Saturn's atmosphere. To demonstrate this, the center-to-limb variation of the equivalent widths of the 619-nm methane and 647-nm ammonia bands (W_{CH4}, W_{NH3}) are shown for a 2°–wide latitude band centered on the equator in Figure 24.

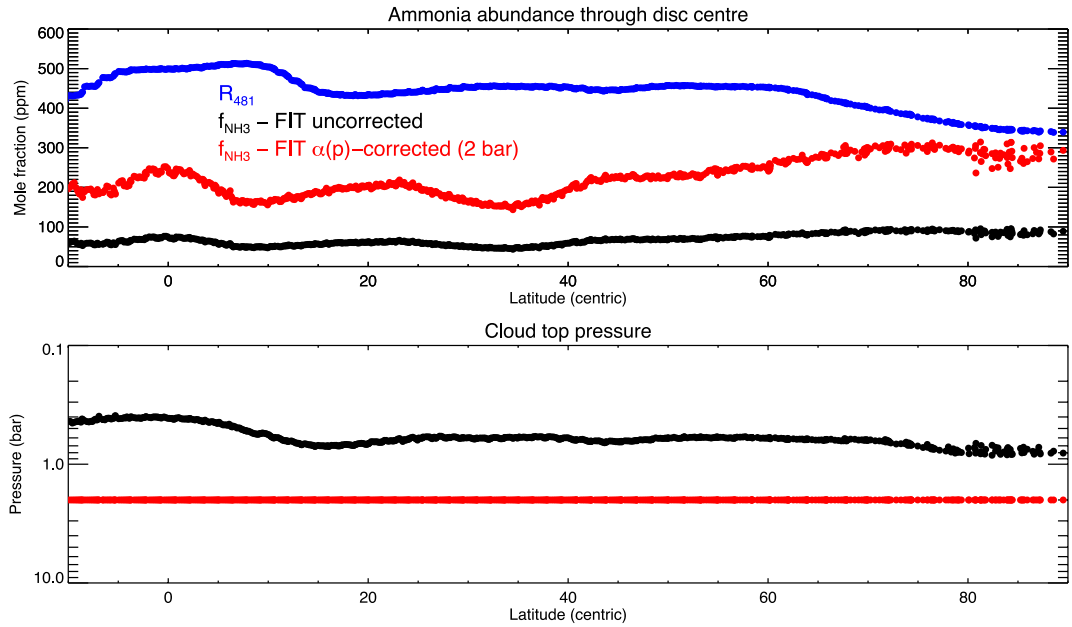

Figure 23. As Figure 6, but showing variation of ammonia abundance (f_{NH3}) (top panel) and cloud-top pressure (p_{cloud}) (bottom panel) along the center of Saturn's disc (region outlined in Figure 21 and roughly along Saturn's central meridian) determined from our VLT/MUSE observations using the FIT reflectivity model. The top panel shows both the original values of f_{NH3} (black) and also the $\alpha(p_{cloud})$-corrected values (red), assuming a fixed pressure p_{cloud} of 2 bar. For reference, the top panel shows the central-meridian blue reflectivity (481 nm), which has been arbitrarily scaled. The bottom panel shows the derived latitudinal variation of p_{cloud} (black) and the actual value used of 2 bar (red) to correct f_{NH3}.

Once again, as for Jupiter (Figure 9), both W_{CH4} and W_{NH3} decrease with the airmass factor, indicating that the hazes in Saturn's atmosphere are vertically extended, with W_{CH4}/W_{NH3} increasing much more rapidly with airmass than for Jupiter. Applying the same analysis as we used in Section 3.1, we took our reference Saturn atmospheric model and, for different assumptions of the pressure level probed in the methane band at nadir, p_0, we used the smoothed variation of the W_{CH4} with airmass, η, to determine the equivalent vertical path abundances (Equation 9), determined the corresponding pressure levels, $p(\eta)$, from $X_{CH4}(p)$ and then calculated the expected variation of W_{NH3} with airmass. Values of nadir-sounding pressure $p_0 = 1$, 3, and 5 bar were assumed and the modeled dependences of W_{NH3} and W_{CH4}/W_{NH3} are overplotted in Figure 24, where the rapid increase of W_{CH4}/W_{NH3} with airmass suggests that pressures as great as 5 bar are being probed at nadir.

While Braude (2019) made an initial analysis of these observations with NEMESIS, a full retrieval analysis of the Saturn MUSE observations is beyond the scope of this paper for the same reasons as we outline in our Jupiter comparisons. In the meantime, we made a preliminary analysis of the 600–680 nm region of the Saturn equatorial nadir spectrum using NEMESIS and a simple aerosol model based on that used for Jupiter, with two aerosol layers: one based at ~3 bar and the other at ~0.05 bar, and retrieved the opacity and width of the lower layer, the opacity of the upper layer (with fixed width $\Delta p/p = 0.2$), together with the imaginary refractive index spectra of the two components. The ammonia profile in our model has a deep abundance of 175 ppm and is limited to 100% relative humidity above the condensation level at ~1.8 bar. From our best-fit solution to the observed equatorial spectrum we once again then added a vertically thin, non-reflecting opaque layer at various pressure levels to isolate and examine the contribution to the total reflection of the overlying aerosols. The results of this analysis are shown in Figure 25, which is identical in form to the earlier analysis of the Jovian equatorial spectrum (Figure 11). Here we can see that the methane band is formed over a very wide range of pressures from 0.1–5 bar and that reflection from the overlying hazes adds to the center of the band, which partially "fills it in", giving it a smaller equivalent width than would be expected from the pressure level of the opaque layer in an aerosol-free atmosphere. This leads, once again, to values of p_{cloud} that are systematically too small, but to a much greater degree than for Jupiter. We again find that the aerosol particles need to be highly scattering to match the observed spectra and so at wavelengths away from the 619-nm methane band, light can scatter down to very deep levels before being reflected back to space. Hence, photons with wavelengths near the 647-nm ammonia band will experience

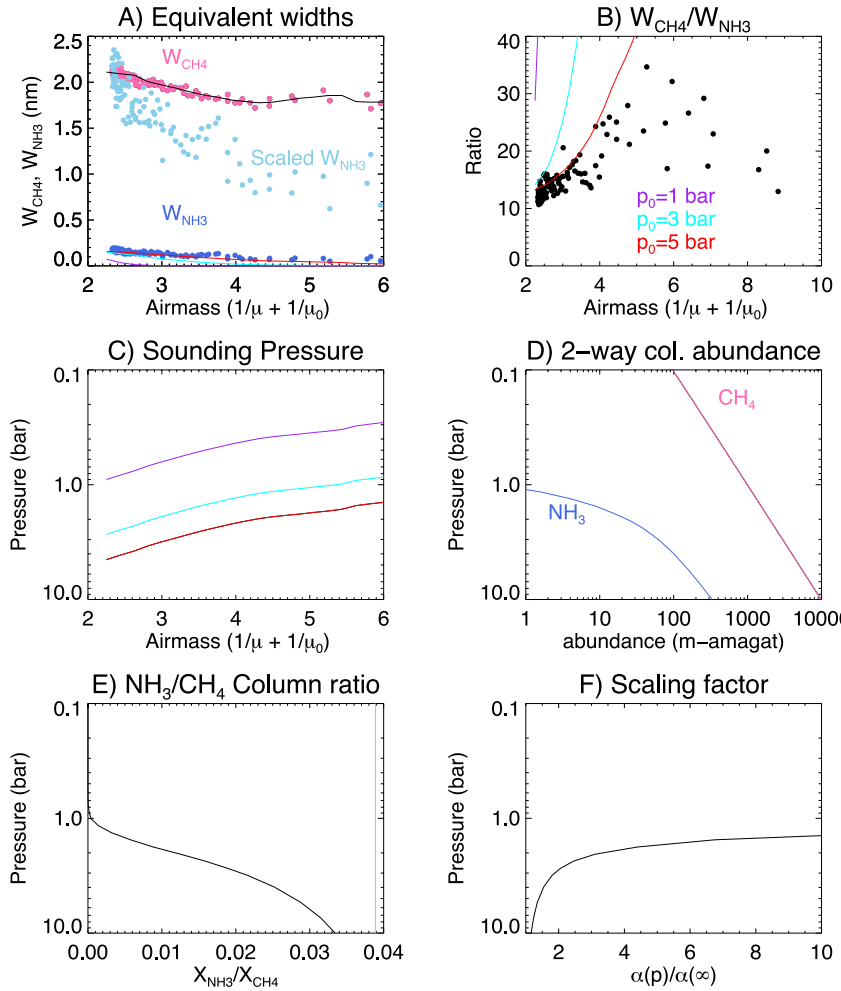

Figure 24. As Figure 12, but showing observations and results for Saturn's atmosphere. Top row shows the variation of the 619-nm CH_4 and 647-nm NH_3 absorption band strengths and band strength ratio (W_{CH4}/W_{NH3}) with airmass factor $\eta = 1/\mu + 1/\mu_0$ at Saturn's equator from VLT/MUSE. In both panels the colored lines show the expected variation of W_{NH3} and W_{CH4}/W_{NH3} with η, respectively, computed from the smoothed variation of W_{CH4} with η (shown in black), depending on the assumed nadir pressure level p_0 observed, which are here set to 1, 3, and 5 bar, respectively. These assumed nadir pressures and calculated variation with airmass are shown in Panel C and are computed from the pressure variation of the two-way methane column abundance from our reference Saturn atmosphere, shown in panel D. The ammonia two-way column abundance is also plotted in panel D, which decreases rapidly above ammonia's condensation level at ~1.8 bar. Panel E shows the variation of X_{NH3}/X_{CH4} as a function of pressure, compared with the asymptotic value at infinite pressure of $f_{NH3}/f_{CH4} = 1.75 \times 10^{-4}/4.5 \times 10^{-3} = 0.03889$. Panel F shows $\alpha = (f_{NH3}X_{CH4})/(f_{CH4}X_{NH3})$, which has a value of unity at depth, and increases as pressure decreases.

very little absorption until they penetrate to levels where the ammonia abundance starts to become significant. As a result, the absorption in the ammonia band in Figure 25 cannot be seen at all until the pressure of the opaque layer exceeds ~2 bar. Hence, in contravention to our usual expectations from the band-depth approximation of Combes and Encrenaz (1979), the levels probed by the methane and ammonia bands are very different, with the ammonia band formed at much deeper pressures than the methane band. This can also be seen in Figure 8, where we show that for a simple two-way transmission calculation in an aerosol-free Saturn model atmosphere, the observed equatorial methane equivalent width (2.149 nm) intersects the calculated curve at ~0.5 bar, whilst the ammonia equivalent width (0.163 nm) intersects the ammonia calculated curve at ~1.5 bar. Computing the Jacobians for aerosol opacity and ammonia abundance from our retrieval, we find the aerosol Jacobian peaks strongly in the 0.2–0.5 bar region, consistent with the values of p_{cloud} we determined, while the ammonia Jacobian peaks at 1.8 bar and extends slightly to deeper pressures.

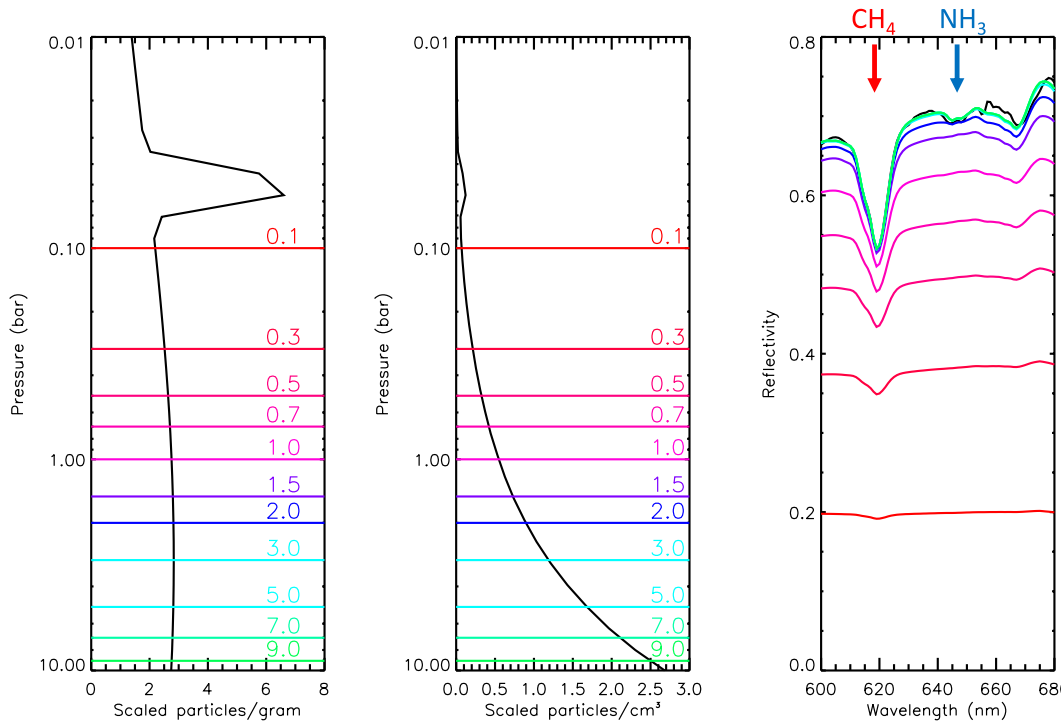

Figure 25. As Figure 11, but showing simulations with an opaque non-reflecting base added at a range of pressures to a model fitted to the nadir equatorial VLT/MUSE spectrum of Saturn. Left and middle panels show the retrieved two-component cloud model in units of particles/gram and particles/cm^3, respectively, with one cloud/haze centered at 3 bar in specific density and the other centered at 0.05 bar, together with the range of pressures for the bottom non-reflecting layer. Right-hand panel compares the measured nadir spectrum (black) with a range of simulations from our best fit model with a non-reflecting base added at the pressures shown in the other panels and shown with the same color. As we go deeper into the atmosphere, the methane band can be seen to deepen, but the ammonia band at 647 nm only becomes observable for pressures greater than the condensation pressure at ~1.8 bar.

While the derived two-way column abundance map, X_{NH3}, shown in Figure 22, is dominated by the abundance of ammonia near the condensation level, it will also be affected by the cloud opacity at this level. Unfortunately, as we have seen the methane column abundance map X_{CH4} is sensitive to the cloud opacity over a much wider range of pressures. Hence, X_{NH3}/X_{CH4} will not cleanly correct for cloud opacity. However, assuming the aerosol opacity is vertically correlated from 0.1–5 bar the variations seen in p_{cloud} probably have the same latitudinal dependence as the clouds at deeper levels and thus X_{NH3}/X_{CH4} is probably a better measure of the variations of deep ammonia mole fraction than X_{NH3} alone. The retrieved values of f_{NH3} ~60 ppm are clearly too small though, just as they were for Jupiter, but this can be understood from Figure 24, where we saw that the increase of W_{CH4}/W_{NH3} with η is more consistent with an effective cloud-top pressure p_0 of 3–5 bar. From our reference Saturn atmospheric model we can calculate the variation of the two-way column abundances of methane and ammonia with pressure (Figure 24d) and calculate the $\alpha(p)$ scaling factor (Equation 11 and Figure 24f). Choosing a fixed value for p_{cloud} of ~3 bar, we calculate $\alpha(p = 3) = 1.9$, which increases f_{NH3} from ~60 to ~110 ppm. In contrast, choosing $p_{cloud} = 2$ bar, leads to a scaling factor of $\alpha(p_{cloud}) = 3.3$, which further increases f_{NH3} to ~200 ppm. Assuming an effective cloud-top pressure of 2 bar, the pressure-corrected variation of f_{NH3} across Saturn's disc (using the FIT method) can be seen in Figure 22 and along Saturn's central meridian in Figure 23. If we assume that f_{NH3} is dominated by latitudinal variations in the abundance of ammonia at ~2–3 bar, the variations determined would seem to indicate upwelling near 0°N, 20°N and polewards of 45°N, and downwelling elsewhere. Alternatively, enhanced ammonia at the poles could indicate less condensation in the slightly warmer polar environment in summer as noted by Cassini/CIRS (Fletcher et al., 2018).

6. Interpretation of Spatial Variations of Ammonia and Cloud Revealed in Saturn's Atmosphere

The band-depth approximation determinations of f_{NH3} for Saturn, shown in Figures 22 and 23, are considerably more uncertain than for Jupiter since: (a) the ammonia and methane bands probe very different pressure levels; (b) we have had to assume that the cloud opacity variations indicated in X_{CH4} are correlated with the opacity near ∼2–3 bar; and (c) we have had to make an educated guess of p_{cloud} to determine the appropriate pressure-scaling factor $\alpha(p)$. While increased values of f_{NH3} could indicate enhanced ammonia mole fraction, they could also indicate a thinning of the deeper clouds, allowing photons to reach deeper into Saturn's atmosphere before being reflected and thus leading to more ammonia absorption. In addition, variations in f_{NH3} could also alias variations in temperature, with regions of elevated temperature increasing the saturated vapor pressure for ammonia and so increasing the condensation level and thus slightly increasing the column abundance. However, Cassini/CIRS observations of Saturn (Fletcher et al., 2007), revealed only small changes in temperature with latitude at pressures greater than 0.6 bar, so this latter degeneracy is perhaps unlikely to be significant.

Cassini/CIRS was sensitive to mid-infrared thermal emission from 0.8 to 0.08 bar, where the ammonia abundance is very low due to condensation, and hence ammonia determinations are difficult. However the latitudinal variation of phosphine (PH_3) is recoverable from these data and shows peak abundances at 5°S, 45°S and 70°S at ∼0.24 bar, and then decreasing toward the south pole (Fletcher et al., 2009). A study of later Cassini/CIRS observations (Hurley et al., 2012) found a strong peak in PH_3 at the equator, and a secondary peak at mid-latitudes, consistent with Fletcher et al. (2007). Hurley et al. (2012) also found that the abundance of ammonia at ∼0.6 bar showed broad peaks at 25°N, S. Although the peak in upper tropospheric PH_3 near the equator mirrors that seen in ammonia here, the other features do not coincide, but then the peak pressure of phosphine sensitivity (∼0.24 bar) is very different from that sounded by the 657-nm ammonia band (∼2–3 bar) in our MUSE data. The abundance of ammonia at deeper levels can, however, be mapped in 5-μm emission spectra. Fletcher et al. (2011) analyzed Cassini/VIMS 5-μm observations, and found strongly increased NH_3 abundance at the equator (also seen in Cassini/RADAR observations, Laraia et al., 2013) and secondary, smaller peaks at 20–30°N and ∼45°N, which agree well with our determinations. Similar conclusions were reached by Barstow et al. (2016) from a separate study of Cassini/VIMS observations. In addition, neither study found great variations in the cloud base pressure (at 2–3 bar) or opacity, although Fletcher et al. (2011) found the base pressure to be less at the equator (∼2 bar, as opposed to ∼2.6 bar elsewhere). This observed small variation in the deep cloud at these pressure levels adds confidence that the ammonia column abundance derived by this technique is most strongly determined by the ammonia mole fraction, rather than changes in "cloud-top" pressure. Indeed, if the cloud is really at lower pressures at the equator, then this would reduce the ammonia column abundance seen at 647 nm, which could explain why we find approximately equal abundances of ammonia at the equator and ∼20°N, while Cassini/VIMS 5-μm observations find the equatorial NH_3 abundance to be significantly larger. Most recently, Fletcher et al. (2023) report observations of Saturn made in November 2022 with the Mid-Infrared Instrument/Medium Resolution Spectrometer (MIRI/MRS) on board the James Webb Space Telescope. The observations spanned 4.9–27.9 μm, with the 5-μm region used to retrieve the ammonia abundance below the ammonia condensation level. The MIRI-retrieved variation of ammonia mole fraction with latitude is compared with our MUSE band-depth approximation values of f_{NH3} (α(2-bar)-corrected) in Figure 26, where we can see remarkably good correlation between the latitudes of peak ammonia abundance. The increased amplitude of the MIRI peak ammonia abundances compared with MUSE is interesting and may be caused by the lower spatial resolution of the MUSE observations, which perhaps average over such features. Alternatively, it may again be that increased abundance of high altitude haze in Saturn's atmospheres, especially near the equator, "fills in" the ammonia band, reducing its apparent abundance in the FITS approach. However, the choice of scaling our values of f_{NH3} with a $\alpha(p)$ correction value calculated at 2 bar appears justified as the general abundances agree very well.

Finally, although we have seen that the cloud-top pressures derived by the band-depth approximation method do not accurately define a hard cloud top, they do give an indication of the general degree of haze opacity and probably also vertical extent. Roman et al. (2013) present an analysis of high spatial resolution Cassini/ISS observations of Saturn made in 2004 soon after Saturn's southern summer solstice, which map the latitudinal distribution of southern hemisphere hazes in Saturn's upper troposphere and lower stratosphere from 1 to 0.01 bar. Roman et al. (2013) find that the tropospheric haze extends highest in the atmosphere at the equator, but does not extend so far up approaching the north pole, very similar in shape to our p_{cloud} dependence (Figure 23). The north polar region was also studied by Sanz-Requena et al. (2018), who analyzed HST and Cassini/ISS observations to

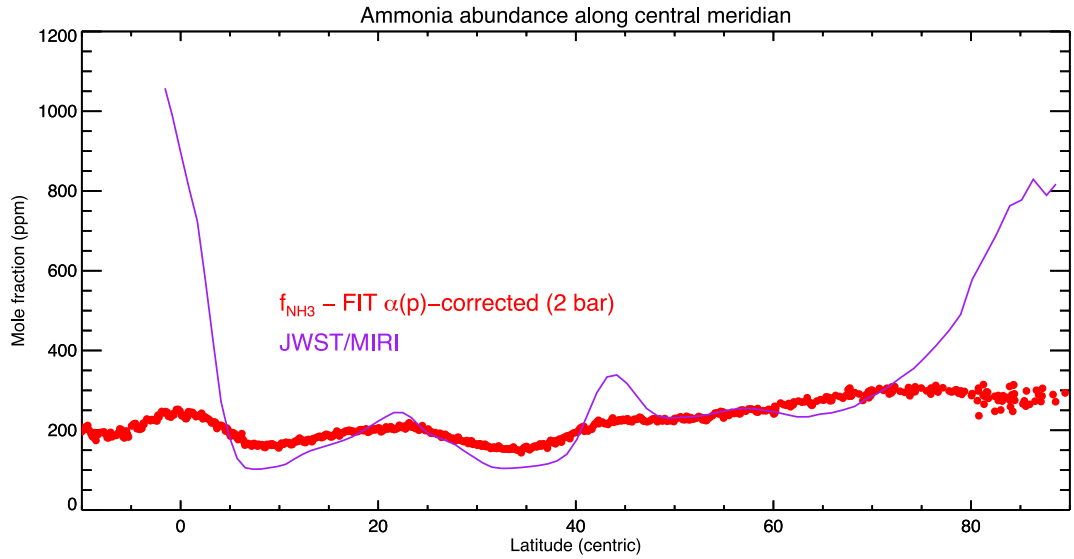

Figure 26. Variation of ammonia abundance (f_{NH3}) roughly along Saturn's central meridian (region shown in Figure 21), determined using the FIT model and $\alpha(p_{cloud})$-corrected to 2 bar (previously shown in Figure 23) compared with the deep ammonia mole fractions retrieved from JWST/MIRI by Fletcher et al. (2023).

find that the opacity of the tropospheric haze in the North Polar Hexagon (NPH) is greatly reduced, which would allow photons to reach deeper levels before being reflected. This is again consistent with our p_{cloud} estimates.

7. Discussion

We have seen that the band-depth approximation provides a remarkable and unexpectedly deep window into the atmospheres of both Jupiter and Saturn, and appears to reliably map the abundance of ammonia below the ammonia condensation level on both planets. The filter-averaged HILL method (Hill et al., 2024) thus allows backyard astronomers to generate maps of ammonia abundance and "cloud-top pressure" that agree very well with formal retrievals from spectral-imaging observations, and means that citizen scientists can generate high-cadence maps of these properties, which could be enormously useful in understanding the dynamics of these turbulent atmospheres. However, considerable potential degeneracy remains in the method, both in terms of spatial variations (as we saw for Jupiter's NEB features in Section 4.2) and also the overall mean abundances since the band-depth approximations (and indeed the formal NEMESIS retrievals) depend on the assumed vertical profile of ammonia mole fraction. For example, our ammonia abundances, where we have assumed the mole fraction to be constant with pressure below the condensation level, are lower than those determined by MWR and VLA by a factor of about 1.6 (Figure 13). If, in fact, the ammonia mole fraction increases with pressure below the condensation level, as suggested by the Galileo Probe results, then the $\alpha(p_{cloud})$ correction factor will be larger and vary more rapidly with pressure; this would help to make the MUSE determinations more consistent with MWR/VLA determinations, and also lead to ammonia abundance abundances over features such as the GRS and NEDFs that are more in line with previous expectations. However, to investigate this further would require analysis of a very much wider range of data covering as wide a wavelength range as possible, which is beyond the scope of this paper. Whether this band-depth technique probes down also to the ammonium hydrosulfide (NH_4SH) precipitation level is harder to judge, since we do not have very reliable estimates of the hydrogen sulphide (H_2S) abundances to predict this level. However, equilibrium cloud condensation models (ECCM) such as those of Atreya et al. (1999), also reported by Irwin (2009), quote expected (NH_4SH) precipitation levels of ~2 bar for Jupiter and ~5 bar for Saturn. Hence, it is quite possible that the ammonia distributions derived here map the ammonia abundance beneath both the ammonia and ammonium hydrosulfide clouds for Jupiter and between the two expected levels for Saturn.

We have also shown in this work that there is very strong evidence that the main cloud "decks" on Jupiter and Saturn are not at the ammonia condensation level, but somewhat deeper. This is consistent with the view that the main aerosols are haze layers composed of an accumulation of photochemical products combined with

condensates of perhaps NH_4SH (Irwin et al., 2001; Sromovsky et al., 1998), ammonia, or maybe even some mixture of ammonia and water ice in a "mushball" phase (Guillot, Stevenson, et al., 2020). However, although we find that the main level of reflection cannot be at the ammonia condensation level, we do find that we need a small abundance of aerosols at these levels, which we model as being a vertical extension from the main aerosol layer below (e.g., Figure 11). Some opacity in the 0.5–1 bar range is also needed to explain the appearance of Jupiter in the mid-infrared at 8.6 μm (Fletcher et al., 2009, 2016). The composition of the photochemical component is not certain, but its spectral properties are similar to materials generated in the laboratory, such as the chromophore of R. W. Carlson et al. (2016), "tholin" materials (Khare et al., 1984, 1993) and phosphorous allotropes (Noy et al., 1981). It is clear, however, that in general we do not see much evidence for fresh ammonia ice, which could be because more ammonia than expected is incorporated into NH_4SH particles or mushballs. In addition, UV insolation may perhaps photolyze ammonia faster than it can be uplifted to its condensation level, or perhaps generate photochemical products that combine with, or coat, ammonia ice particles, masking their spectral properties and perhaps affecting their sublimation temperatures. Hence, it may be that detectable ammonia ice clouds can only ever form in localized regions of very rapid upwelling that transport ammonia up to its condensation level faster than it can be photodissociated, and/or coated/combined with photochemical products.

The redness of the GRS could be because the air is trapped inside the vortex and so photolysis has longer to act. It is certainly apparent that the reflectivity spectra of the GRS and NEB are very different, with the GRS looking very similar to the EZ at wavelengths longer than ~700 nm (Figure S4 in Supporting Information S1), while the NEB is darker not just at blue wavelengths, indicating more chromophore, but at red wavelengths also. Hence, the GRS is a region of enhanced chromophore and cloud opacity, while the NEB would be better interpreted as a region of lower cloud opacity, which perhaps better reveals the chromophore component.

8. Conclusions

We have shown in this paper that observations of the 600–680 nm reflectivity spectra of Jupiter and Saturn offer an unexpectedly deep window into ammonia abundance variations in the atmospheres of Jupiter and Saturn, allowing the spatial variation of ammonia abundance to be probed below the ammonia condensation level at pressures of ~2–3 bar for both planets. This means that backyard astronomers are able to generate very useful high-cadence maps of ammonia abundance and "cloud-top pressure" to help understand the dynamics of these atmospheres. Furthermore, we have shown that the simple band-depth approximation method, developed by Hill et al. (2024) and further refined here, allows the ammonia distribution to be inferred rapidly from either spectral or filter-averaged observations with remarkably low computational cost and high reliability. With appropriate corrections, this allows citizen and professional scientists alike to investigate the circulation of these atmospheres on a pixel-by-pixel basis.

The detailed conclusions of this paper are:

1. We find that the band-depth approximation, comparing the equivalent widths of the 619-nm methane and 647-nm ammonia bands, provides a mostly reliable and cost-efficient method of determining the relative deep abundance variations in the atmospheres of both Jupiter and Saturn at pressures of 2–3 bar;
2. We find very strong evidence that the main level of reflection in both atmospheres is significantly deeper than the ammonia condensation level. For Jupiter, we find the dominant pressure level of reflection to be 2–3 bar, while it may be even deeper in Saturn's atmosphere. Although the vertically extended nature of the retrieved aerosol profiles, and the difference between the vertical profiles of methane and ammonia mole fraction make it difficult to unambiguously define a "cloud-top pressure", these observations add to the weight of evidence that the clouds we generally see in visible imaging are not predominantly ammonia ice, although local regions of vigorous updraft may raise ammonia to its condensation level in Jupiter's atmosphere before it can be photodissociated;
3. We find strong latitudinal constraints on the abundance of ammonia in Jupiter's atmosphere at a pressure level of 2–3 bar, which closely match the abundance variations seen by the VLA and Juno/MWR. In particular, we see a significant enhancement at ~2–4°N and a significant depletion from 7 to 20°N, covering the NEB and NTrZ. The amplitude of the belt/zone variations of ammonia abundance at other latitudes is smaller, but variations are seen all the way to the poles. We note, however, that these results are partly dependent on the assumed vertical profile of ammonia mole fraction;

4. We find evidence for a slight depletion of ammonia within the GRS at pressure levels of 2–3 bar. This finding might be consistent with the extreme redness of the GRS arising from the air being trapped in the vortex allowing more time for ammonia to be photodissociated and formed into "chromophore" particles. The lower abundance within the GRS, with more depletion toward the south, together with a bounding thin annulus of even lower ammonia abundance, are all also seen in VLA X-band determinations and a host of other mid-IR results;
5. We show that NEDFs (or 5-μm hotspots) have considerably depleted aerosol abundances, which increases the significance of the blue Rayleigh-scattering component, giving these features their distinctive color. In addition, we find enhanced ammonia abundances in the south and east of these features, but that the ammonia column abundance is low in the "plume" regions to the west of NEDFs, indicating either lower ammonia gas abundances, or perhaps additional ammonia ice clouds, which act to mask the ammonia gas absorption. While we also find high ammonia abundances over the center of the NEDFs, this assumes that the ammonia mole fraction profile does not vary with pressure below the condensation level, which is particularly unlikely for these NEDFs, where strong subsidence might be occurring to depress the NH_3 column. It is possible that ammonia is severely depleted below the condensation level, and the apparent enhancement is due to light being able to penetrate very deeply to where the ammonia mole fraction is less depleted. Assuming the ammonia mole fraction increases with pressure below the condensation level leads to results that are more consistent with previous determinations; We find that the band-depth approximation technique also works in Saturn's atmosphere, even though the pressure levels probed by the 619-nm methane band (0.1–2 bar) and the 647-nm ammonia band (~3 bar) are very different;
6. We find that the abundance of ammonia at ~3 bar varies strongly with latitude in Saturn's atmosphere, with latitudinal maxima seen at 0, 20 and 45°N, and steadily increasing abundance seen from 45°N to the north pole. This variation agrees well with recent deep ammonia mole fractions retrieved from 5-μm observations made by JWST/MIRI. However, the conclusions for Saturn are much more uncertain than for Jupiter due to the several confounding factors described in Section 5.

Finally, as we have already alluded to, retrieving estimates of the abundances of aerosols and condensable gases such as NH_3 in a giant planet atmosphere is fraught with difficulty as this is a very degenerate problem. Similar difficulties are found when analyzing the spectra of Uranus and Neptune, and Irwin, Teanby, Fletcher, et al. (2022) have shown in their "holistic" study that to begin to break the degeneracies we need to consider simultaneously the available observations from as wide a wavelength range as possible, and also consider the center-to-limb variations. Sadly, such a study is beyond the scope of the present paper. However, an analysis of Jovian MUSE observations over their complete wavelength range (475–933 nm) is in preparation and we hope in the near future to conduct a study leading to an "holistic" aerosol model also for both Jupiter and Saturn.

Appendix A: Absorption Band-Depth Method

The absorption band-depth method (e.g., Combes & Encrenaz, 1979) was developed initially within the context of a Reflecting Layer Model (RLM), where the cloud tops are treated as a discrete reflecting surface with a characteristic, wavelength-dependent reflectivity. The vertical column abundance, $X_{\rm gas}$ (molecule/m^2) of a well-mixed gas above a certain pressure level, p, is given by

$$X_{\rm gas} = f_{\rm gas} n H \tag{A1}$$

where $f_{\rm gas}$ is the mole fraction of the gas, $n = p/kT$ is the number density (molecule/m^3) at pressure p and temperature T (k is the Boltzmann constant), and H is the atmospheric scale height, which is the height over which the pressure drops by a factor of e (i.e., Napier's constant). This scale height can be calculated as:

$$H = \frac{RT}{\overline{m}g} \tag{A2}$$

where R is the gas constant, g is the local gravitational acceleration (ms^{-2}) and $\overline{m}$ is the mean molecular weight of the atmosphere (kg/mol). Substituting for n and H in Equation A1 we find

$$X_{\text{gas}} = f_{\text{gas}} \frac{p}{kT} \frac{RT}{\overline{m}g} = \frac{f_{\text{gas}} p N_A}{\overline{m}g} \tag{A3}$$

where we have used that the gas constant, R, is equal to kN_A, where N_A is Avogadro's number.

When observing the absorption of methane or ammonia above clouds, we need to multiply the vertical column abundance by a geometric factor to account for the sunlight passing through the gas to the cloud at some zenith angle, and then being reflected back to the observer at another zenith angle. When observing a single location, this factor, η, can be written as:

$$\eta = \frac{1}{\mu} + \frac{1}{\mu_0} \tag{A4}$$

where μ is the cosine of the viewing zenith angle and μ_0 is the cosine of the solar viewing zenith angle. Hence, observing in the nadir with the sun directly overhead, $\eta = 2$, and then η increases as we view at higher zenith angles. When analyzing disc-averaged observations, assuming a simple Reflecting Layer Model, the disc-averaged geometric factor can be shown to be $\eta = 4$, (e.g., Chamberlain & Hunten, 1987)

Including this geometric factor, the absorption of the gas along the reflecting path can then be calculated as

$$\tau_{\text{gas}} = \eta X_{\text{gas}} k_{\text{gas}} = \frac{\eta f_{\text{gas}} p N_A k_{\text{gas}}}{\overline{m}g} \tag{A5}$$

where k_{gas} is the absorption coefficient of the gas (m^2/molecule).

If we observe the absorption of both CH_4 and NH_3 for the same path, and assume that the number densities of these gases both fall with the same scale height then it can be seen that

$$\frac{\tau_{\text{NH3}}}{\tau_{\text{CH4}}} = \frac{f_{\text{NH3}} k_{\text{NH3}}}{f_{\text{CH4}} k_{\text{CH4}}} \tag{A6}$$

since all other quantities cancel. Hence, we deduce that:

$$f_{\text{NH3}} = f_{\text{CH4}} \frac{\tau_{\text{NH3}}}{\tau_{\text{CH4}}} \frac{k_{\text{CH4}}}{k_{\text{NH3}}} = f_{\text{CH4}} \frac{X_{\text{NH3}}}{X_{\text{CH4}}} \tag{A7}$$

In practice, the path abundance (molecule/m^2) is often measured in units of km-amagat, where an amagat is the number density of an ideal gas at 1 atm pressure (i.e., 101.325 kPa) and 0°C (i.e., 273.15 K), equal to 2.68678×10^{25} molecule/m^3, or 44.165 mol/m^3. In such cases, the absorption coefficients are expressed in units of (km-amagat)$^{-1}$.

Equation A7 for f_{NH3} was derived assuming a Reflecting Layer Model (RLM) with the number densities of the two gases assumed to decrease with the same scale height above the reflecting layer. However, if we can show that the two absorption bands are formed at the same pressure level then this ratio of absorption method works equally well for a vertically extended scattering cloud model, assuming the vertical profiles of the two gases differ only by a single multiplicative constant. However, the rearrangement of Equation A5 to give cloud top pressure:

$$p_{\text{cloud}} = \frac{\tau_{\text{gas}} \overline{m}g}{\eta f_{\text{gas}} N_A k_{\text{gas}}} \tag{A8}$$

is *only* valid under RLM conditions for gases with mole fractions that do not vary with height.

In this paper we show that the assumption of Equation A7 that both CH_4 and NH_3 have the same shaped vertical profile is not valid, since once the ammonia condensation level is reached the mole fraction of ammonia follows the saturated vapor pressure curve and hence the number density decreases with height faster than for methane.

If we are probing a region well above a condensation level of one of the two observed constituents then they will have well defined, but different, scale heights. Under these conditions we can modify Equation A3 to

$$X_{\text{gas}} = f_{\text{gas}} \frac{p}{kT} H_{\text{gas}} \tag{A9}$$

where H_{gas} is the effective scale height of the gas in question. Under these conditions, Equation A5 becomes

$$\tau_{\text{gas}} = \eta X_{\text{gas}} k_{\text{gas}} = \frac{\eta f_{\text{gas}} p H_{\text{gas}} k_{\text{gas}}}{kT} \tag{A10}$$

and Equation A7 becomes

$$f_{\text{NH3}} = f_{\text{CH4}} \frac{\tau_{\text{NH3}}}{\tau_{\text{CH4}}} \frac{k_{\text{CH4}}}{k_{\text{NH3}}} \frac{H_{\text{CH4}}}{H_{\text{NH3}}}. \tag{A11}$$

However, we find in this study that we are probing in and around the condensation level of ammonia. Under these circumstances we have found it is better to multiply our f_{NH3} values by a correction factor $\alpha(p_{\text{cloud}})$ (Equation 11) calculated from the nadir two-way column abundance profiles ($X_{\text{CH4}}(p)$ and $X_{\text{NH3}}(p)$) of our a priori temperature-pressure models, using p_{cloud} values calculated directly from X_{CH4} for Jupiter, or from other constraints and assumptions for Saturn.

Data Availability Statement

The smoothed and projected VLT/MUSE data sets studied in this paper are available at Irwin (2024b). These data were recorded under ESO programmes: 0104.C-0136 (Jupiter) and 298.C-5050 (Saturn). Data files associated with this analysis are available at Irwin (2024a). The spectral fitting and retrievals were performed using the NEMESIS radiative transfer and retrieval algorithm Irwin et al. (2008) and can be downloaded from Irwin et al. (2022b) (or https://github.com/nemesiscode/radtrancode), with supporting website information at Irwin et al. (2022a) (or https://github.com/nemesiscode/nemesiscode.github.io).

Acknowledgments
We are grateful to the United Kingdom Science and Technology Facilities Council (STFC) for funding the early phases of this research (ST/S000461/1). Fletcher was supported by a UK STFC Consolidated Grant: ST/W00089X/1. Charlotte Alexander is supported by a UK STFC studentship. We are grateful for having been able to use and process observations made with the MUSE instrument at the European Southern Observatory's Very Large Telescope. For the purpose of open access, the principal author has applied a Creative Commons Attribution (CC BY) license to the Author Accepted Manuscript version arising from this submission.

References

Achterberg, R. K., Conrath, B. J., & Gierasch, P. J. (2006). Cassini CIRS retrievals of ammonia in Jupiter's upper troposphere. *Icarus*, *182*(1), 169–180. https://doi.org/10.1016/j.icarus.2005.12.020

Alexander, C. (2024). *Remote sounding of the Jovian atmosphere (Unpublished doctoral dissertation)*. University of Oxford.

Atreya, S. K., Wong, M. H., Owen, T. C., Mahaffy, P. R., Niemann, H. B., de Pater, I., et al. (1999). A comparison of the atmospheres of Jupiter and Saturn: Deep atmospheric composition, cloud structure, vertical mixing, and origin. *Planetary and Space Science*, *47*(10–11), 1243–1262. https://doi.org/10.1016/S0032-0633(99)00047-1

Baines, K. H., Carlson, R. W., & Kamp, L. W. (2002). Fresh ammonia ice clouds in Jupiter. I. Spectroscopic identification, spatial distribution, and dynamical implications. *Icarus*, *159*(1), 74–94. https://doi.org/10.1006/icar.2002.6901

Baines, K. H., Sromovsky, L. A., Carlson, R. W., Momary, T. W., & Fry, P. M. (2019). The visual spectrum of Jupiter's Great Red Spot accurately modeled with aerosols produced by photolyzed ammonia reacting with acetylene. *Icarus*, *330*, 217–229. https://doi.org/10.1016/j.icarus.2019.04.008

Banfield, D., Gierasch, P. J., Bell, M., Ustinov, E., Ingersoll, A. P., Vasavada, A. R., et al. (1998). Jupiter's cloud structure from Galileo imaging data. *Icarus*, *135*(1), 230–250. https://doi.org/10.1006/icar.1998.5985

Barstow, J. K., Irwin, P. G. J., Fletcher, L. N., Giles, R. S., & Merlet, C. (2016). Probing Saturn's tropospheric cloud with Cassini/VIMS. *Icarus*, *271*, 400–417. https://doi.org/10.1016/j.icarus.2016.01.013

Bjoraker, G. L., Wong, M. H., de Pater, I., Hewagama, T., & Ádámkovics, M. (2022). The spatial variation of water clouds, NH_3, and H_2O on Jupiter using keck data at 5 microns. *Remote Sensing*, *14*(18), 4567. https://doi.org/10.3390/rs14184567

Bolton, S. J., Levin, S. M., Guillot, T., Li, C., Kaspi, Y., Orton, G., et al. (2021). Microwave observations reveal the deep extent and structure of Jupiter's atmospheric vortices. *Science*, *374*(6570), 968–972. https://doi.org/10.1126/science.abf1015

Braude, A. S. (2019). *Colour and cloud structure in the atmospheres of the giant planets (Doctoral Disseration)*. University of Oxford.

Braude, A. S., Irwin, P. G. J., Orton, G. S., & Fletcher, L. N. (2020). Colour and tropospheric cloud structure of Jupiter from MUSE/VLT: Retrieving a universal chromophore. *Icarus*, *338*, 113589. https://doi.org/10.1016/j.icarus.2019.113589

Carlson, R., Smythe, W., Baines, K., Barbinis, E., Becker, K., Burns, R., et al. (1996). Near-infrared spectroscopy and spectral mapping of Jupiter and the Galilean satellites: Results from Galileo's initial orbit. *Science*, *274*(5286), 385–388. https://doi.org/10.1126/science.274.5286.385

Carlson, R. W., Baines, K. H., Anderson, M. S., Filacchione, G., & Simon, A. A. (2016). Chromophores from photolyzed ammonia reacting with acetylene: Application to Jupiter's Great Red Spot. *Icarus*, *274*, 106–115. https://doi.org/10.1016/j.icarus.2016.03.008

Carlson, R. W., Weissman, P. R., Smythe, W. D., & Mahoney, J. C. (1992). Near-infrared mapping spectrometer experiment on Galileo. *SSRv*, *60*(1–4), 457–502. https://doi.org/10.1007/BF00216865

Chamberlain, J. W., & Hunten, D. M. (1987). *Theory of planetary atmospheres. An introduction to their physics and chemistry* (2nd ed. (Vol. 36). Academic Press.
Chance, K., & Kurucz, R. L. (2010). An improved high-resolution solar reference spectrum for earth's atmosphere measurements in the ultraviolet, visible, and near infrared. *Journal of Quantitative Spectroscopy & Radiative Transfer*, *111*(9), 1289–1295. https://doi.org/10.1016/j.jqsrt.2010.01.036
Choi, D. S., Showman, A. P., Vasavada, A. R., & Simon-Miller, A. A. (2013). Meteorology of Jupiter's equatorial hot spots and plumes from Cassini. *Icarus*, *223*(2), 832–843. https://doi.org/10.1016/j.icarus.2013.02.001
Coles, P. A., Yurchenko, S. N., & Tennyson, J. (2019). ExoMol molecular line lists - XXXV. A rotation-vibration line list for hot ammonia. *MNRAS*, *490*(4), 4638–4647. https://doi.org/10.1093/mnras/stz2778
Combes, M., & Encrenaz, T. (1979). A method for the determination of abundance ratios in the outer planets—Application to Jupiter. *Icarus*, *39*(1), 1–27. https://doi.org/10.1016/0019-1035(79)90096-4
Dahl, E. K., Chanover, N. J., Orton, G. S., Baines, K. H., Sinclair, J. A., Voelz, D. G., et al. (2021). Vertical structure and color of Jovian latitudinal cloud bands during the Juno era. *Planetary Science Journal*, *2*(1), 16. https://doi.org/10.3847/PSJ/abd400
de Pater, I., Sault, R. J., Butler, B., DeBoer, D., & Wong, M. H. (2016). Peering through Jupiter's clouds with radio spectral imaging. *Science*, *352*(6290), 1198–1201. https://doi.org/10.1126/science.aaf2210
de Pater, I., Sault, R. J., Wong, M. H., Fletcher, L. N., DeBoer, D., & Butler, B. (2019). Jupiter's ammonia distribution derived from VLA maps at 3-37 GHz. *Icarus*, *322*, 168–191. https://doi.org/10.1016/j.icarus.2018.11.024
Flasar, F. M., Achterberg, R. K., Conrath, B. J., Pearl, J. C., Bjoraker, G. L., Jennings, D. E., et al. (2005). Temperatures, winds, and composition in the Saturnian system. *Science*, *307*(5713), 1247–1251. https://doi.org/10.1126/science.1105806
Fletcher, L. N., Baines, K. H., Momary, T. W., Showman, A. P., Irwin, P. G. J., Orton, G. S., et al. (2011). Saturn's tropospheric composition and clouds from Cassini/VIMS 4.6-5.1 μm nightside spectroscopy. *Icarus*, *214*(2), 510–533. https://doi.org/10.1016/j.icarus.2011.06.006
Fletcher, L. N., Greathouse, T. K., Orton, G. S., Sinclair, J. A., Giles, R. S., Irwin, P. G. J., & Encrenaz, T. (2016). Mid-infrared mapping of Jupiter's temperatures, aerosol opacity and chemical distributions with IRTF/TEXES. *Icarus*, *278*, 128–161. https://doi.org/10.1016/j.icarus.2016.06.008
Fletcher, L. N., Irwin, P. G. J., Teanby, N. A., Orton, G. S., Parrish, P. D., Calcutt, S. B., et al. (2007). The meridional phosphine distribution in Saturn's upper troposphere from Cassini/CIRS observations. *Icarus*, *188*(1), 72–88. https://doi.org/10.1016/j.icarus.2006.10.029
Fletcher, L. N., King, O. R. T., Harkett, J., Hammel, H. B., Roman, M. T., Melin, H., et al. (2023). Saturn's atmosphere in northern summer revealed by JWST/MIRI. *Journal of Geophysical Research: Planets*, *128*(9), e2023JE007924. https://doi.org/10.1029/2023JE007924
Fletcher, L. N., Orton, G. S., Greathouse, T. K., Rogers, J. H., Zhang, Z., Oyafuso, F. A., et al. (2020). Jupiter's equatorial plumes and hot spots: Spectral mapping from Gemini/TEXES and Juno/MWR. *Journal of Geophysical Research: Planets*, *125*(8), e06399. https://doi.org/10.1029/2020JE006399
Fletcher, L. N., Orton, G. S., Mousis, O., Yanamandra-Fisher, P., Parrish, P. D., Irwin, P. G. J., et al. (2010). Thermal structure and composition of Jupiter's Great Red Spot from high-resolution thermal imaging. *Icarus*, *208*(1), 306–328. https://doi.org/10.1016/j.icarus.2010.01.005
Fletcher, L. N., Orton, G. S., Sinclair, J. A., Guerlet, S., Read, P. L., Antuñano, A., et al. (2018). A hexagon in Saturn's northern stratosphere surrounding the emerging summertime polar vortex. *Nature Communications*, *9*(1), 3564. https://doi.org/10.1038/s41467-018-06017-3
Fletcher, L. N., Orton, G. S., Teanby, N. A., Irwin, P. G. J., & Bjoraker, G. L. (2009). Methane and its isotopologues on Saturn from Cassini/CIRS observations. *Icarus*, *199*(2), 351–367. https://doi.org/10.1016/j.icarus.2008.09.019
Fletcher, L. N., Oyafuso, F. A., Allison, M., Ingersoll, A., Li, L., Kaspi, Y., et al. (2021). Jupiter's temperate belt/zone contrasts revealed at depth by Juno microwave observations. *Journal of Geophysical Research: Planets*, *126*(10), e06858. https://doi.org/10.1029/2021JE006858
Folkner, W. M., Woo, R., & Nandi, S. (1998). Ammonia abundance in Jupiter's atmosphere derived from the attenuation of the Galileo probe's radio signal. *Journal of Geophysical Research*, *103*(E10), 22847–22856. https://doi.org/10.1029/98JE01635
Gershman, R., Buxbaum, K. L., Ludwinski, J. M., & Paczkowski, B. G. (1994). Galileo mission planning for Low Gain Antenna based operations. In J. L. Rash (Ed.), *Space mission operations and ground data systems* (pp. 279–286).
Gierasch, P. J., Conrath, B. J., & Magalhães, J. A. (1986). Zonal mean properties of Jupiter's upper troposphere from voyager infrared observations. *Icarus*, *67*(3), 456–483. https://doi.org/10.1016/0019-1035(86)90125-9
Grassi, D., Adriani, A., Mura, A., Atreya, S. K., Fletcher, L. N., Lunine, J. I., et al. (2020). On the spatial distribution of minor species in Jupiter's troposphere as inferred from Juno JIRAM data. *Journal of Geophysical Research: Planets*, *125*(4), e06206. https://doi.org/10.1029/2019JE006206
Grassi, D., Mura, A., Sindoni, G., Adriani, A., Atreya, S. K., Filacchione, G., et al. (2021). On the clouds and ammonia in Jupiter's upper troposphere from Juno JIRAM reflectivity observations. *MNRAS*, *503*(4), 4892–4907. https://doi.org/10.1093/mnras/stab740
Guillot, T., Li, C., Bolton, S. J., Brown, S. T., Ingersoll, A. P., Janssen, M. A., et al. (2020). Storms and the depletion of ammonia in Jupiter: II. Explaining the Juno observations. *Journal of Geophysical Research: Planets*, *125*(8), e06404. https://doi.org/10.1029/2020JE006404
Guillot, T., Rosenqvist, M., Wong, M., Orton, G., Eichstädt, G., Brueshaber, S., et al. (2023). How high are Jupiter's clouds? Analysis of JunoCam images of the "Nautilus". In *EGU general assembly conference abstracts* (pp. EGU–17178). https://doi.org/10.5194/egusphere-egu23-17178
Guillot, T., Stevenson, D. J., Atreya, S. K., Bolton, S. J., & Becker, H. N. (2020). Storms and the depletion of ammonia in Jupiter: I. Microphysics of "Mushballs". *Journal of Geophysical Research: Planets*, *125*(8), e06403. https://doi.org/10.1029/2020JE006403
Hill, S. M., Irwin, P. G. J., Alexander, C., & Rogers, J. H. (2024). Spatial variations of Jovian tropospheric ammonia via ground-based imaging. *Earth and Space Science*, *11*(8), e2024EA003562. https://doi.org/10.1029/2024EA003562
Hurley, J., Fletcher, L. N., Irwin, P. G. J., Calcutt, S. B., Sinclair, J. A., & Merlet, C. (2012). Latitudinal variation of upper tropospheric NH_3 on Saturn derived from Cassini/CIRS far-infrared measurements. *Planetary and Space Science*, *73*(1), 347–363. https://doi.org/10.1016/j.pss.2012.08.003
Irwin, P. G. J. (2009). *Giant planets of our solar system* (2nd ed.). Springer. https://doi.org/10.1007/978-3-540-85158-5
Irwin, P. G. J. (2024a). patrickirwin/Jupiter_Saturn_MUSE: Figure data for Jupiter/Saturn MUSE paper (Version v3) [Dataset]. *Zenodo*. https://doi.org/10.5281/zenodo.12635611
Irwin, P. G. J. (2024b). Smoothed VLT/MUSE observations of Jupiter and Saturn (version 1) [Dataset]. *Zenodo*. https://doi.org/10.5281/zenodo.12634418
Irwin, P. G. J., Bowles, N., Braude, A. S., Garland, R., & Calcutt, S. (2018). Analysis of gaseous ammonia (NH_3) absorption in the visible spectrum of Jupiter. *Icarus*, *302*, 426–436. https://doi.org/10.1016/j.icarus.2017.11.031
Irwin, P. G. J., Bowles, N., Braude, A. S., Garland, R., Calcutt, S., Coles, P. A., et al. (2019). Analysis of gaseous ammonia (NH_3) absorption in the visible spectrum of Jupiter - Update. *Icarus*, *321*, 572–582. https://doi.org/10.1016/j.icarus.2018.12.008
Irwin, P. G. J., Dobinson, J., James, A., Teanby, N. A., Simon, A. A., Fletcher, L. N., et al. (2024). Modelling the seasonal cycle of Uranus's colour and magnitude, and comparison with Neptune. *MNRAS*, *527*(4), 11521–11538. https://doi.org/10.1093/mnras/stad3761

Irwin, P. G. J., Dobinson, J., James, A., Toledo, D., Teanby, N. A., Fletcher, L. N., et al. (2021). Latitudinal variation of methane mole fraction above clouds in Neptune's atmosphere from VLT/MUSE-NFM: Limb-darkening reanalysis. *Icarus*, *357*, 114277. https://doi.org/10.1016/j.icarus.2020.114277

Irwin, P. G. J., Parrish, P., Fouchet, T., Calcutt, S. B., Taylor, F. W., Simon-Miller, A. A., & Nixon, C. A. (2004). Retrievals of Jovian tropospheric phosphine from Cassini/CIRS. *Icarus*, *172*(1), 37–49. https://doi.org/10.1016/j.icarus.2003.09.027

Irwin, P. G. J., Teanby, N. A., de Kok, R., Fletcher, L. N., Howett, C. J. A., Tsang, C. C. C., et al. (2022a). nemesiscode/nemesiscode.github.io: Nemesis documentation website [Software]. *Zenodo*. https://doi.org/10.5281/zenodo.5816724

Irwin, P. G. J., Teanby, N. A., de Kok, R., Fletcher, L. N., Howett, C. J. A., Tsang, C. C. C., et al. (2022b). nemesiscode/radtrancode: Nemesis (v1.0.0) [Software]. *Zenodo*. https://doi.org/10.5281/zenodo.5816714

Irwin, P. G. J., Teanby, N. A., de Kok, R., Fletcher, L. N., Howett, C. J. A., Tsang, C. C. C., et al. (2008). The NEMESIS planetary atmosphere radiative transfer and retrieval tool. *Journal of Quantitative Spectroscopy & Radiative Transfer*, *109*(6), 1136–1150. https://doi.org/10.1016/j.jqsrt.2007.11.006

Irwin, P. G. J., Teanby, N. A., Fletcher, L. N., Toledo, D., Orton, G. S., Wong, M. H., et al. (2022). Hazy blue worlds: A holistic aerosol model for Uranus and Neptune, including dark spots. *Journal of Geophysical Research: Planets*, *127*(6), e07189. https://doi.org/10.1029/2022JE007189

Irwin, P. G. J., Weir, A. L., Smith, S. E., Taylor, F. W., Lambert, A. L., Calcutt, S. B., et al. (1998). Cloud structure and atmospheric composition of Jupiter retrieved from Galileo near-infrared mapping spectrometer real-time spectra. *Journal of Geophysical Research*, *103*(E10), 23001–23022. https://doi.org/10.1029/98JE00948

Irwin, P. G. J., Weir, A. L., Taylor, F. W., Calcutt, S. B., & Carlson, R. W. (2001). The origin of belt/zone contrasts in the atmosphere of Jupiter and their correlation with 5-μm opacity. *Icarus*, *149*(2), 397–415. https://doi.org/10.1006/icar.2000.6542

Janssen, M. A., Oswald, J. E., Brown, S. T., Gulkis, S., Levin, S. M., Bolton, S. J., et al. (2017). MWR: Microwave radiometer for the Juno mission to Jupiter. *SSRv*, *213*(1–4), 139–185. https://doi.org/10.1007/s11214-017-0349-5

Karkoschka, E. (1994). Spectrophotometry of the Jovian planets and titan at 300- to 1000-nm wavelength: The methane spectrum. *Icarus*, *111*(1), 174–192. https://doi.org/10.1006/icar.1994.1139

Karkoschka, E. (1998). Methane, ammonia, and temperature measurements of the Jovian planets and titan from CCD-spectrophotometry. *Icarus*, *133*(1), 134–146. https://doi.org/10.1006/icar.1998.5913

Karkoschka, E., & Tomasko, M. G. (2010). Methane absorption coefficients for the Jovian planets from laboratory, Huygens, and HST data. *Icarus*, *205*(2), 674–694. https://doi.org/10.1016/j.icarus.2009.07.044

Khare, B. N., Sagan, C., Arakawa, E. T., Suits, F., Callcott, T. A., & Williams, M. W. (1984). Optical constants of organic tholins produced in a simulated Titanian atmosphere: From soft x-ray to microwave frequencies. *Icarus*, *60*(1), 127–137. https://doi.org/10.1016/0019-1035(84)90142-8

Khare, B. N., Thompson, W. R., Cheng, L., Chyba, C., Sagan, C., Arakawa, E. T., et al. (1993). Production and optical constants of ice tholin from charged particle irradiation of (1:6) C_2H_6/H_2O at 77 K. *Icarus*, *103*(2), 290–300. https://doi.org/10.1006/icar.1993.1071

Laraia, A. L., Ingersoll, A. P., Janssen, M. A., Gulkis, S., Oyafuso, F., & Allison, M. (2013). Analysis of Saturn's thermal emission at 2.2-cm wavelength: Spatial distribution of ammonia vapor. *Icarus*, *226*(1), 641–654. https://doi.org/10.1016/j.icarus.2013.06.017

Li, C., Ingersoll, A., Janssen, M., Levin, S., Bolton, S., Adumitroaie, V., et al. (2017). The distribution of ammonia on Jupiter from a preliminary inversion of Juno microwave radiometer data. *Geophysical Research Letters*, *44*(11), 5317–5325. https://doi.org/10.1002/2017GL073159

Matcheva, K. I., Conrath, B. J., Gierasch, P. J., & Flasar, F. M. (2005). The cloud structure of the Jovian atmosphere as seen by the Cassini/CIRS experiment. *Icarus*, *179*(2), 432–448. https://doi.org/10.1016/j.icarus.2005.06.020

Meftah, M., Sarkissian, A., Keckhut, P., & Hauchecorne, A. (2023). The SOLAR-HRS new high-resolution solar spectra for disk-integrated, disk-center, and intermediate cases. *Remote Sensing*, *15*(14), 3560. https://doi.org/10.3390/rs15143560

Minnaert, M. (1941). The reciprocity principle in lunar photometry. *ApJ*, *93*, 403–410. https://doi.org/10.1086/144279

Moeckel, C., de Pater, I., & DeBoer, D. (2023). Ammonia abundance derived from Juno MWR and VLA observations of Jupiter. *Planetary Science Journal*, *4*(2), 25. https://doi.org/10.3847/PSJ/acaf6b

Niemann, H. B., Atreya, S. K., Carignan, G. R., Donahue, T. M., Haberman, J. A., Harpold, D. N., et al. (1998). The composition of the Jovian atmosphere as determined by the Galileo probe mass spectrometer. *Journal of Geophysical Research*, *103*(E10), 22831–22846. https://doi.org/10.1029/98JE01050

Noy, N., Podolak, M., & Bar-Nun, A. (1981). Photochemistry of phosphine and Jupiter's Great Red Spot. *Journal of Geophysical Research*, *86*(C12), 11985–11988. https://doi.org/10.1029/JC086iC12p11985

Orton, G., Ortiz, J. L., Baines, K., Bjoraker, G., Carsenty, U., Colas, F., et al. (1996). Earth-based observations of the Galileo probe entry site. *Science*, *272*(5263), 839–840. https://doi.org/10.1126/science.272.5263.839

Pérez-Hoyos, S., & Sánchez-Lavega, A. (2006). On the vertical wind shear of Saturn's Equatorial Jet at cloud level. *Icarus*, *180*(1), 161–175. https://doi.org/10.1016/j.icarus.2005.07.011

Plass, G. N., Kattawar, G. W., & Catchings, F. E. (1973). Matrix operator theory of radiative transfer. 1: Rayleigh scattering. *ApOpt*, *12*(2), 314–329. https://doi.org/10.1364/AO.12.000314

Ragent, B., Colburn, D. S., Rages, K. A., Knight, T. C. D., Avrin, P., Orton, G. S., et al. (1998). The clouds of Jupiter: Results of the Galileo Jupiter mission probe nephelometer experiment. *Journal of Geophysical Research*, *103*(E10), 22891–22910. https://doi.org/10.1029/98JE00353

Ragent, B., Privette, C. A., Avrin, P., Waring, J. G., Carlston, C. E., Knight, T. C. D., & Martin, J. P. (1992). Galileo probe nephelometer experiment. *SSRv*, *60*(1–4), 179–201. https://doi.org/10.1007/BF00216854

Rogers, J. H. (2019). Jupiter's north equatorial belt & jet I. Cyclic expansions & planetary waves. *The Journal of the British Astronomical Association*, *129*, 13–26.

Roman, M. T., Banfield, D., & Gierasch, P. J. (2013). Saturn's cloud structure inferred from Cassini ISS. *Icarus*, *225*(1), 93–110. https://doi.org/10.1016/j.icarus.2013.03.015

Roos-Serote, M., Drossart, P., Encrenaz, T., Lellouch, E., Carlson, R. W., Baines, K. H., et al. (1998). Analysis of Jupiter north equatorial belt hot spots in the 4-5-μm range from Galileo/near-infrared mapping spectrometer observations: Measurements of cloud opacity, water, and ammonia. *Journal of Geophysical Research*, *103*(E10), 23023–23042. https://doi.org/10.1029/98JE01049

Roos-Serote, M., & Irwin, P. G. J. (2006). Scattering properties and location of the Jovian 5-micron absorber from Galileo/NIMS limb-darkening observations. *Journal of Quantitative Spectroscopy & Radiative Transfer*, *101*(3), 448–461. https://doi.org/10.1016/j.jqsrt.2006.02.074

Sanz-Requena, J. F., Pérez-Hoyos, S., Sánchez-Lavega, A., Antuñano, A., & Irwin, P. G. J. (2018). Haze and cloud structure of Saturn's North Pole and hexagon wave from Cassini/ISS imaging. *Icarus*, *305*, 284–300. https://doi.org/10.1016/j.icarus.2017.12.043

Showman, A. P., & de Pater, I. (2005). Dynamical implications of Jupiter's tropospheric ammonia abundance. *Icarus*, *174*(1), 192–204. https://doi.org/10.1016/j.icarus.2004.10.004

Sromovsky, L. A., Baines, K. H., Fry, P. M., & Carlson, R. W. (2017). A possibly universal red chromophore for modeling color variations on Jupiter. *Icarus*, *291*, 232–244. https://doi.org/10.1016/j.icarus.2016.12.014

Sromovsky, L. A., Best, F. A., Collard, A. D., Fry, P. M., Revercomb, H. E., Freedman, R. S., et al. (1996). Solar and thermal radiation in Jupiter's atmosphere: Initial results of the Galileo probe net flux radiometer. *Science*, *272*(5263), 851–854. https://doi.org/10.1126/science.272.5263.851

Sromovsky, L. A., Collard, A. D., Fry, P. M., Orton, G. S., Lemmon, M. T., Tomasko, M. G., & Freedman, R. S. (1998). Galileo probe measurements of thermal and solar radiation fluxes in the Jovian atmosphere. *Journal of Geophysical Research*, *103*(E10), 22929–22977. https://doi.org/10.1029/98JE01048

Sromovsky, L. A., & Fry, P. M. (2002). Jupiter's cloud structure as constrained by Galileo probe and HST observations. *Icarus*, *157*(2), 373–400. https://doi.org/10.1006/icar.2002.6844

Sromovsky, L. A., & Fry, P. M. (2010a). The source of 3-μm absorption in Jupiter's clouds: Reanalysis of ISO observations using new NH_3 absorption models. *Icarus*, *210*(1), 211–229. https://doi.org/10.1016/j.icarus.2010.06.040

Sromovsky, L. A., & Fry, P. M. (2010b). The source of widespread 3-μm absorption in Jupiter's clouds: Constraints from 2000 Cassini VIMS observations. *Icarus*, *210*(1), 230–257. https://doi.org/10.1016/j.icarus.2010.06.039

Sromovsky, L. A., & Fry, P. M. (2018). Composition and structure of fresh ammonia clouds on Jupiter based on quantitative analysis of Galileo/NIMS and New Horizons/LEISA spectra. *Icarus*, *307*, 347–370. https://doi.org/10.1016/j.icarus.2017.10.037

Statman, J. I., & Deutsch, L. J. (1997). Galileo's telecommunications using the low-gain spacecraft Antenna. In C. Barbieri, J. Rahe, T. V. Johnson, & A. M. Sohus (Eds.), *The three Galileos the man, the spacecraft the telescope* (Vol. 220, pp. 107–113). https://doi.org/10.1007/978-94-015-8790-7_10

West, R. A., Strobel, D. F., & Tomasko, M. G. (1986). Clouds, aerosols, and photochemistry in the Jovian atmosphere. *Icarus*, *65*(2–3), 161–217. https://doi.org/10.1016/0019-1035(86)90135-1

Wong, M. H., Bjoraker, G. L., Smith, M. D., Flasar, F. M., & Nixon, C. A. (2004). Identification of the 10-μm ammonia ice feature on Jupiter. *Planetary and Space Science*, *52*(5–6), 385–395. https://doi.org/10.1016/j.pss.2003.06.005

Wong, M. H., Mahaffy, P. R., Atreya, S. K., Niemann, H. B., & Owen, T. C. (2004). Updated Galileo probe mass spectrometer measurements of carbon, oxygen, nitrogen, and sulfur on Jupiter. *Icarus*, *171*(1), 153–170. https://doi.org/10.1016/j.icarus.2004.04.010